Nanopatterning of tools for replication of non-planar polymer surfaces

Cech, Jiri; Taboryski, Rafael J.

Publication date:
2013

Document Version
Publisher's PDF, also known as Version of record

Nanopatterning of tools for replication of non-planar polymer surfaces

PhD Thesis

Jiri Cech

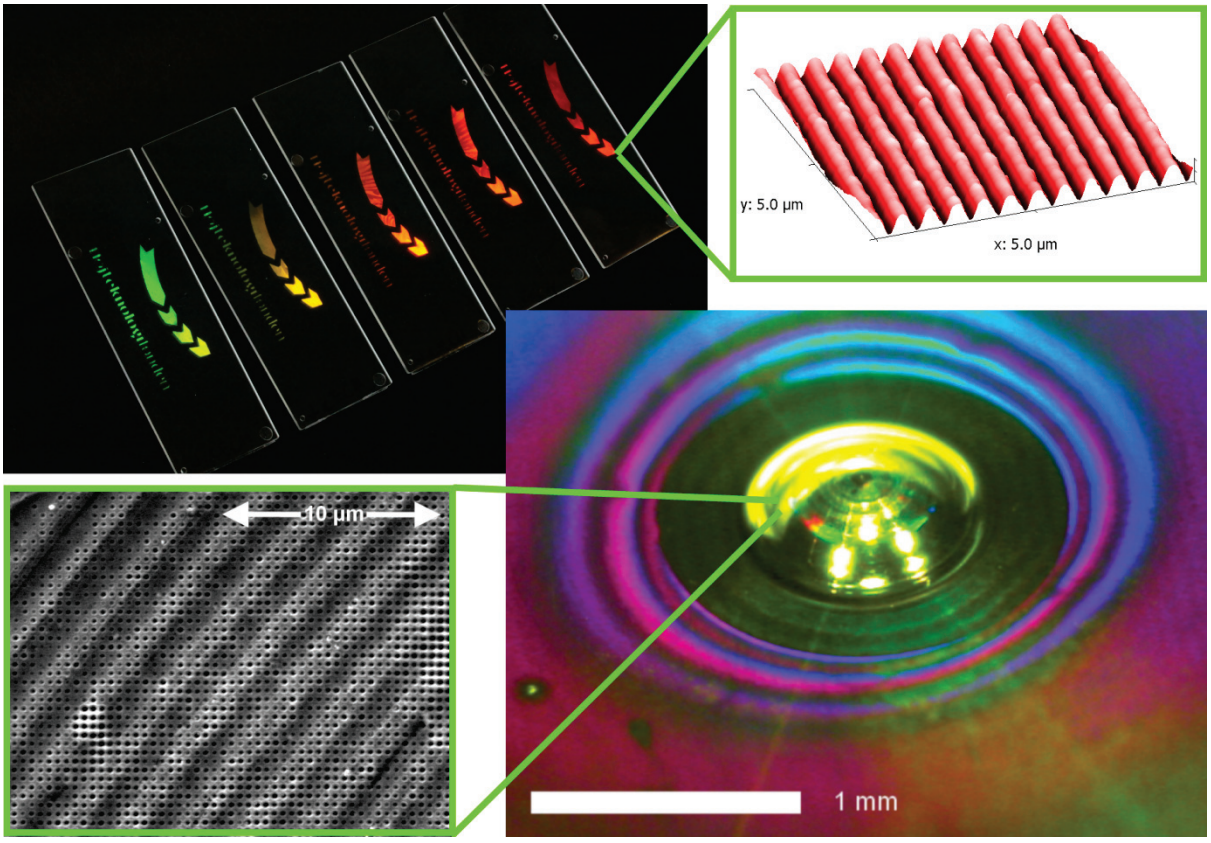

March 8, 2013

DTU Nanotech
Department of Micro- and Nanotechnology

I lovingly dedicate this thesis to my kids Kristina and Tom, and my wife Sylvia, who supported me each step of the way. There is no doubt in my mind that without her continued support and patience I could not have completed this process.

Abstract

The nanostructured surfaces, as seen in both nature and in the lab, offer a broad range of advanced functionalities, such as stunning structural colors, antireflective, self-cleaning, superhydrophobic, superhydrophilic or antifogging effects. Those effects are facilitated by the specific arrangement of micro- and nano- structures on the surface. Manmade nanostructured surfaces, formed by advanced microfabrication techniques, can often mimic or even exceed natural ones in some property. However, there is a substantial limitation, as most of the abovementioned techniques work only on a flat, planar surface. One of the most widely used fabrication techniques, polymer injection molding, is not only capable of replicating extremely small structures, but also to produce parts with complex, non-planar shapes, at affordable cost. If we want to use injection molding for making products with nanostructured surfaces, we need to fabricate molds facing the same problem. In this work, we address this problem. At first, we need to verify if the previously reported monolayer adhesion-reducing coating (FDTS) can be used under different conditions during actual injection molding. Such coatings are critical to facilitate de-molding of the nanopatterned parts. We analyzed the coated surfaces of aluminum, titanium, and nickel molds before and after 500 molding cycles, using X-ray photoelectron spectroscopy, AFM and contact angle measurements. We show that the contact angle and that the fluorine concentration on the surface remains increased. These results enable us to predict the coating lifetime and the linearity of the coating removal. Based on the data, we can state that FDTS can be used for coating of molds, and is particularly suited for coating of nanostructured molds. We can also rank tested metals in the order of expected lifetime in descending order: aluminum, titanium, and nickel. The second problem addressed is the forming of a nanostructured surface on a non-planar substrate. We used the hydrostatic nanoimprinting technique, with the HSQ films deposited by spin-coating and spray-coating methods, on flat and curved mold inserts. The HSQ films are durable and tough, which makes them good candidates for molds, but the room temperature nanoimprint such high viscosity films as the HSQ dictates the use of extreme pressures, up to 800 bar. We designed and tested a special device capable of operation at those pressures, and used it to transfer the precise nanopattern with a period of 426 nm onto HSQ films on spherical surfaces with radii of curvature as low as 500 μm. With the pattern transferred onto a curved substrate, we investigated the pattern distortion, resulting from contact between inherently flat nickel masters and double-curved spherical surfaces. The mean pattern period was measured as a function of radial distance and found to be in good agreement with the foil strain computed with a finite element (FE) method. Moreover, this FE method was able to predict the contact pressure as a function of the radial distance. The FE method was also able to predict the sudden pressure drop at the position corresponding to the experimentally observed limit behind which the pattern was no longer replicated. We

demonstrated a feasible method to produce non-planar nanopatterned surfaces for use as injection mold inserts. This opens new possibilities for making affordable polymer products with functional nanostructured surfaces.

Resume på dansk

Nanostrukturerede overflader, som kan ses både i naturen og i laboratoriet, indeholder en bred vifte af avancerede funktionaliteter, såsom fantastiske strukturelle farver, antireflektive -, selvrensende -, superhydrofobe -, superhydrofile - eller dug hæmmende effekter. Disse effekter opstår ved en særlig orientering af mikro- og nano-strukturer på overfladen. Menneskeskabte nanostrukturerede overflader, der fremstilles med avancerede halvleder mikrofabrikationsteknikker, kan ofte ligne eller endda i nogle tilfælde overgå de naturlige effekter. Men der er en væsentlig begrænsning, da de fleste af de ovennævnte teknikker kun kan anvendes på flade og plane overflader såsom silicium wafere. En af de mest udbredte industrielle fremstillingsteknikker, polymer sprøjtestøbning, er ikke blot i stand til at replikere ekstremt små strukturer, men også i stand til at fremstille plastemner med komplekse ikke-plane former til en rimelig pris. Hvis vi ønsker at bruge sprøjtestøbning til fremstilling af produkter med nanostrukturerede overflader, er vi også nødt til at fremstille formene og står over for den samme problemstilling med at overføre nanostrukturerne fra de plane halvledersubstrater. I denne afhandling adresseres denne problemstilling. I første omgang undersøges om den velkendte monolag tykke adhæsions-reducerende belægning (FDTS) kan anvendes under forskellige forhold, herunder selve sprøjtestøbningen. Disse belægninger er afgørende for at fremme afformningen af nanostrukturerede emner. Vi har undersøgt belagte overflader af aluminium-, titan- og nikkelforme før og efter 500 støbecykler ved brug af XPS, AFM og kontaktvinkel målinger. Vi viser, at kontaktvinklen øges, og at indholdet af fluor på overfladen forbliver højt efter brug. Ud fra resultaterne kan vi forudsige den forventede levetid og lineariteten af slid på belægningen. Fra disse data kan man konkludere at FDTS kan anvendes til belægning af forme, og er særlig velegnet til belægning af nanostrukturerede forme. Vi kan også rangordne testede metaller efter størrelsesordenen af den forventede levetid af FDTS belægningen på dem. I aftagende rækkefølge får vi: aluminium, titanium og nikkel. Det andet adresserede problem er overførslen af nanostrukturer til plane substrater. Vi brugte en hydrostatisk nanoimprint teknik, hvor en HSQ film blev deponeret ved hjælp af spin-coating og senere spray-coating på henholdsvis flade og krumme formdele. HSQ filmene viste sig at være slidstærke og hårde, hvilket gør dem til gode kandidater til strukturering af formgivende overflader, men den høje viskositet af HSQ under nanoimprint processen ved stuetemperatur krævede ekstremt høje tryk, op til 800 bar. Vi designede og testede en særlig anordning, der virkede til nanoimprint ved disse høje tryk, og brugte den til at overføre et præcist nanomønster med en periode på 426 nm til en HSQ film på sfæriske overflader med krumningsradier ned til 500 µm. Efter at mønsteret var blevet overført til en krum flade, undersøgte vi strækningen af mønsteret som følge af kontakten mellem de i sagens natur flade nikkel mastere og de dobbelt-krumme sfæriske formoverflader. Den gennemsnitlige mønster-periode blev målt som funktion

af den radiære afstand og blev fundet til at være i god overensstemmelse med folie strækket beregnet med en finite element (FE) metode. FE metoden var i stand til at forudsige kontakttrykket som funktion af den radiære afstand fra centrum, og dermed også i stand til at forudsige det abrupte fald i kontakttryk ved en afstand fra centrum svarende til den eksperimentelt observerede grænse, bag hvilken mønsteret ikke længere var replikeret. Vi har således demonstreret en mulig metode til fremstilling af ikke-plane nanostrukturerede overflader til anvendelsen som formgivende overflader i sprøjtestøbeforme. Dette åbner for overkommelige nye muligheder for at fremstille polymerprodukter med funktionelle nanostrukturerede overflader.

Contents

Preface

This thesis has been written in partial fulfillment of the requirements for obtaining the PhD degree at the Technical University of Denmark (DTU). This PhD project has been conducted at the Department of Micro- and Nanotechnology (DTU Nanotech) from September 2009 to December 2012.

The initial project, titled *"Processing and characterisation of precision polymer on glass structures for wafer based fabrication of optical elements"*, carried out with several industrial partners was changed due to the bankruptcy of Nokia Denmark and a major change in scope between the remaining partners, where they no longer needed polymer optical structures. Consequently, new objectives and a new title, *"Nanopatterning of tools for replication of non-planar polymer surfaces"*, were defined. They are presented in this thesis.

Functional micro- and nanostructured surfaces, as seen in nature in various organisms are often seen on non-planar substrates. This dictates some of methods used if we want to create them artificially. We selected injection molding as a method capable of mass production of polymer objects with complex geometries, perfluorosilane-based anti adhesion coating, and hydrogen silsesquioxane as the imprintable resist, as is discussed in the **Introduction**.

To facilitate the de-molding of the final plastic parts, the molds need to be coated with an adhesion reducing coating. In **chapter 2**, we test the stability of the selected coating on an aluminum mold surface, and in **chapter 3** on titanium and nickel mold surfaces.

Chapter 4 shows nanopatterning on a non-planar surface, namely on a PMMA spherical surface with radius of 1 mm, but such surface is not directly usable as a mold.

In order to fabricate tools needed for the mass replication of nanostructured non-planar polymer parts, we selected HSQ as a hard, tough and durable material. HSQ films can be used to reduce roughness on freeform surfaces, as shown in **chapter 5**, and, using the toolbox developed in **chapter 6**, a mold insert with a spherical surface with a radius of 500 µm was imprinted with 426 nm structures, as shown in **chapter 7**. This shows that it can be used as an example of a non-planar nanopatterned polymer replication tool.

Chapters 2, 5 and part of chapter 3 have been published or submitted for publication as can be seen in the list of publications on page 109.

Kgs. Lyngby, March 7, 2013

Jiri Cech

Glossary

AFM	Atomic force microscopy
BA	Benzyl alcohol
CFL	Capillary force lithography
DIIM	Di-iodomethane
FDTS	Perfluorodecyltrichlorosilane
FE	Finite element
FIB	Focused ion beam
HDMS	hexamethyldisilazane
HSQ	Hydrogen silsesquioxane
IM	Injection molding
IPA	Isopropyl alcohol
MIBK	Methyl isobutyl ketone
MVD	Molecular vapor deposition
NIL	Nanoimprint lithography
PDMS	Polydimethylsiloxane
PMMA	Polymethyl methacrylate
POSS	Polyhedral oligomeric silsesquioxane
SEM	Scanning electron microscopy
TOPAS COC	the trade name for Topas polymers‘ cyclic olefin copolymers
XPS	X-ray photoelectron spectroscopy
ZEONOR COP	the trade name for Zeonor cyclo olefin polymers

Chapter 1: Introduction

"I often say that when you can measure what you are speaking about, and express it in numbers, you know something about it; but when you cannot measure it, when you cannot express it in numbers, your knowledge is of a meagre and unsatisfactory kind."

William Thomson, Lord Kelvin of Largs (1824-1907)

Nano- and micro-structured surfaces, which give an additional surface functionality, are nothing new. One can clearly state that they have been around for millions of years, much longer than mankind as we know it. With a half billion years of evolution, the structures and functions of the surface are almost perfect for helping natural creatures to hide, survive, live and prosper. Nanopatterns and nanostructures in nature are not prepared in cleanrooms, using the most advanced e-beam or ion lithography systems, parallel beams of high-energy X-rays from a synchrotron radiation source, expensive masks, obscure toxic resists, ultra high purity chemicals and perfectly flat silicon substrates. Yet, even without all that they provide functionalities some of which are extremely difficult to fully understand, let alone mimic.

A prime example of effects provided by nanopattern on surface is color, as shown on Figure 1 from [1]. One can see typical nanostructures used to create and enhance color effect on plant flowers, insect shells, hair, wings and eyes.

Often this same nanostructured surface provides a lot more than just a nice look. Periodic gratings on flowers help them to stay clean by making water drops roll of the surface; this is known as a superhydrophobic or self-cleaning surface. Periodic multilayer superlattice help make Molluscs shells hard and tough. Microstructures on shark skin make them not only clean, but provides them with such a low drag that it inspired swimsuits used by 2008 Summer Olympics star Michael Phelps to beat other competitors. Antireflective properties of 2-D arrays of nanorods on insect eyes are well known. Perhaps less known is a structure closely resembling hollow optical fibre, found in a hair of marine worms. One can even find examples of very advanced optical structures, such as 3-D optical crystals, found in the beetles, or reverse opal structures, found in exotic butterflies. Some of these structures are so advanced that it is almost impossible to make them artificially in the lab.

We can look beyond color and consider the popular superhydrophobic/superhydrophilic effect. Each regular mosquito eye consists of a large closely-packed array of microhemispheres

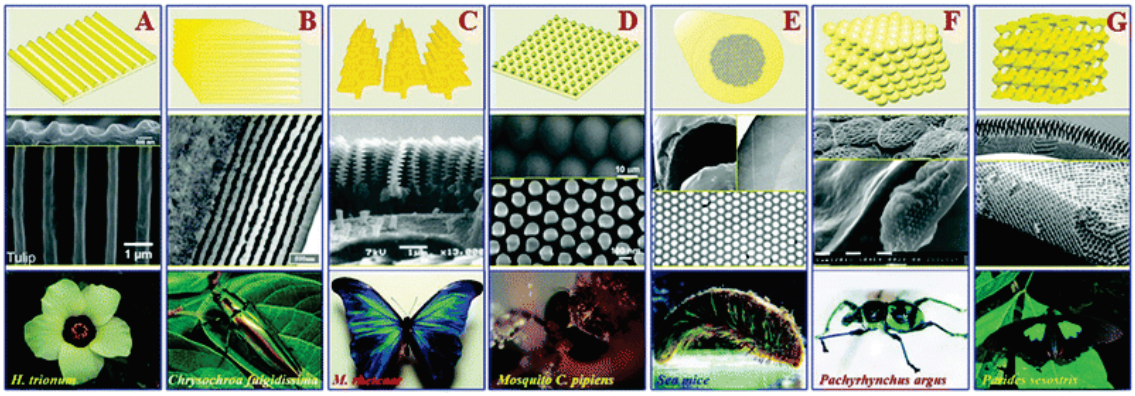

Figure 1*. Typical photonic nanostructures in natural creatures: (A) 1D grating can be found in some plant flowers, such as Hibiscus trionum and Tulipa species; (B) 1D periodicity in the form of multilayers widely existing in some insects, birds, fish, plant leaves, berries, algae, and so on; (C) some discrete 1D periodicity can be found in Morpho butterflies and certain iridescent plant leaves; (D) natural surfaces with 2D gratings are used for antireflection and self-cleaning by some nocturnal insects, such as moth and some butterflies; (E) natural 2D periodicity in the form of cylindrical voids that are embedded in a high-refractive-index solid medium, such as those found in the iridescent hairs of certain marine worms—Aphrodite; (F) close-packed spheres of solid materials generate the iridescence of gem opals and have recently been discovered in the beetle—Pachyrhynchus argus; (G) inverse opal analogous nanostructures generate the iridescence of several species of exotic butterflies, such as the Parides sesostris.* From [1].

(ommatidia), which are curved, few micrometer-wide lenses, placed on a curved substrate. This assembly alone is very difficult to mimic, yet it provides an extremely wide field of view. But the eye surface functionality does not stop there, as can be shown in Figure 2, there is an additional array of tiny, non-close-packed nanonipples. They are approximately 100 nm in diameter, and 50 nm apart, perfectly spaced to make the highly-curved surface of individual microhemispheres antifogging and dry even in the most difficult conditions, where everything around is covered by water drops, large and small.

Since the famous 1959 talk at Caltech, given by Richard P. Feynman [2], researchers in the field of micro and nanotechnology have been able to get really close and often below the minimum sizes of natural nanostructures, or to create completely new structures, unseen in nature, such as single walled carbon nanotubes or quantum dots. Micro and nanotechnology is now part of our daily lives and can be found in various

applications around us, and it is clearly an advantage to have surfaces with advanced functionalities on our everyday products.

Unfortunately, the vast majority of those man-made nanopatterns and nano-objects have been created on planar substrates. Everything in this field is build around silicon wafers and microelectronics fabrication processes of 1970s. The most common equipment to expose and form nanopatterns, such as optical lithography projection systems, have an extremely low depth of focus. Nanoimprinters, spin-coaters, hot plates and even wafer carriers usually anticipate flat samples. The majority of microfabrication characterization equipment is ruled by the same planar substrate assumption; optical microscopes are limited by the same laws as projection systems, the *z*-range of an AFM piezo scanner is few µm, contact angle (drop shape) measurement expects flat sample on which the drop sits, and similarly for XPS, ellipsometer or prism coupler measurement techniques. Even the optical profiler device, where one would expect suitability for curved samples, fails to measure high or deep samples when they are highly curved. One of few methods, where curved sample is not that big problem problem is SEM.

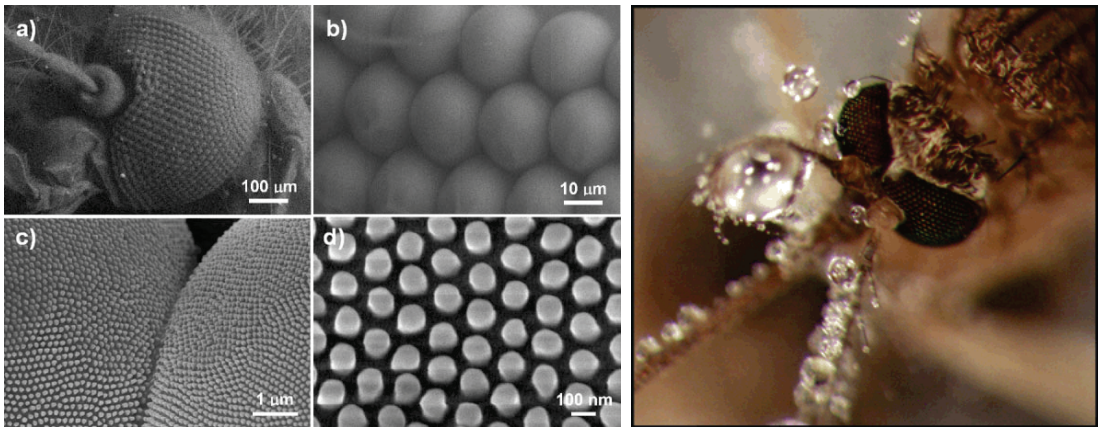

***Figure 2**. Antifogging properties in mosquito eyes. Left panel: a) An SEM image of a single mosquito eye. b) An hcp microhemispheres (ommatidia). c) Two neighboring ommatidia. d) Hexagonally non-close-packed nanonipples covering an ommatidial surface. Right: A photograph of antifogging mosquito eyes. Micro and nano structures shown on left panel causes that even though eyes are exposed to moisture, the surface remains dry and clear while the surrounding hairs nucleate water drops. From* [3].

Despite all this, it would be very beneficial to have method and tools to create synthetic nanopatterns of our choice, with well tuned properties of our choice, on freeform, non-planar surfaces. After all, the world around us is full of objects not flat like a silicon wafer. There are countless applications, from hi-tech industry to basic products. It is not so difficult to imagine a superhydrophobic and antifogging structures on say the optical lens on the head of a laparoscopic or an endoscopic tool so doctors could better see when the tool is inside patient's body, or a well designed array of antireflective nanorods on the lens of your cell phone camera, or on an IR

heat seeker tip of a guided missile, or say, hydrophobic and oleophobic food packaging, or simply polymer toys decorated with structural colors formed in a harmless and well tested plastic without a need for expensive and possibly toxic paints.

Now we established that nanopatterns may provide additional, very useful functionalities, and that having such functional nanopatterns on freeform, non-planar surfaces, is highly desirable. Let's have a look how they can be and have been created.

Functional nanopatterns on non-planar surfaces

Due to obvious limits of projection methods, imprinting [4], embossing or pattern transfer where a stamp, an imprint tool, intrinsically planar is brought in contact with a freeform, non-planar, substrate is often the method of choice. Outlined below are a few examples.

Nanopatterns on curved surfaces are usually realized with soft elastic stamps made from materials such as PDMS, as reported by Choi *et al*. [5], where cylindrical and spherical substrates with radius of 10 mm were used, as shown on Figure 3.

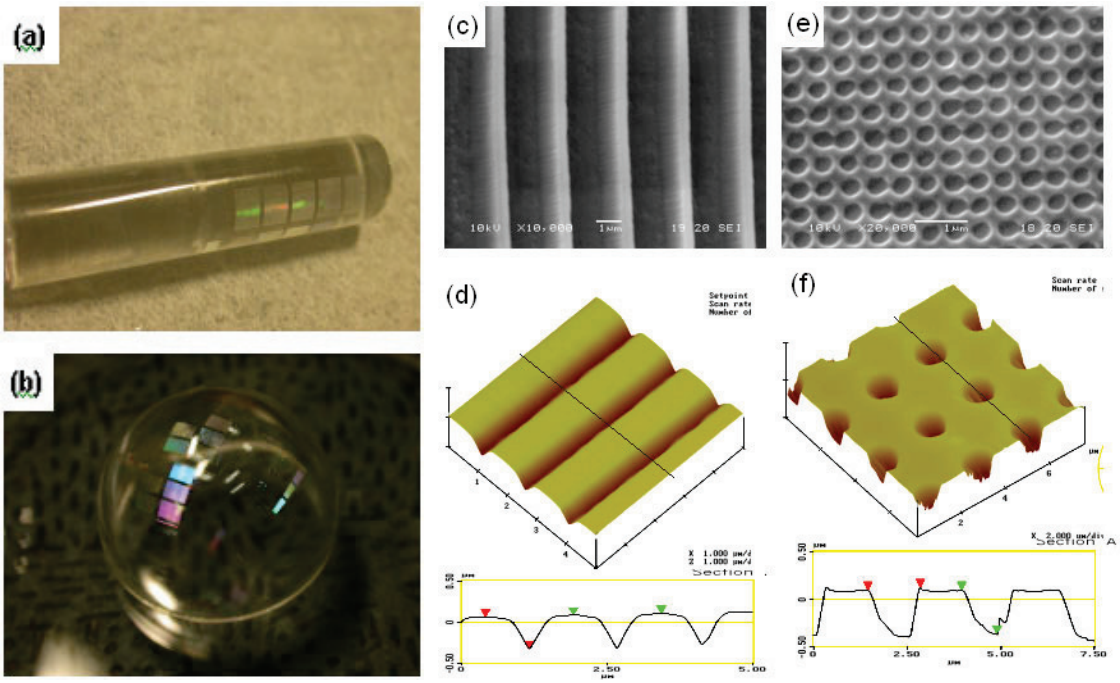

***Figure 3**. Nanopatterns on a curved (a) and a double-curved (b) surface, where the 10 mm PS sphere was used, (c) SEM of line pattern and (d) AFM of the same and (e) SEM of 400 nm dot array and (f) AFM of the same array.*

Polyvinyl alcohol and nickel stamp was used by Hong *et al*. [6], where the force was delivered by gas pressure (5 bar) and a cylindrical substrate with radius of 20 mm was used. Another work, by Chang et al. [7], where the gas pressure was used to imprint

600 nm features on 2 inch steel disk with curvature radius of 80 mm shows the need for moderate pressure (40 bar), even when a soft stamp (PDMS) and a soft resist (PMMA) is used.

Weng *et al*. reports [8] an interesting method, where a flexible, PDMS stamp is cast with a magnetic layer, then applied to the surface with 1 bar of gas pressure , and after reaching sufficient contact with the substrate, an electromagnet is activated which increases the force to 13 bar.

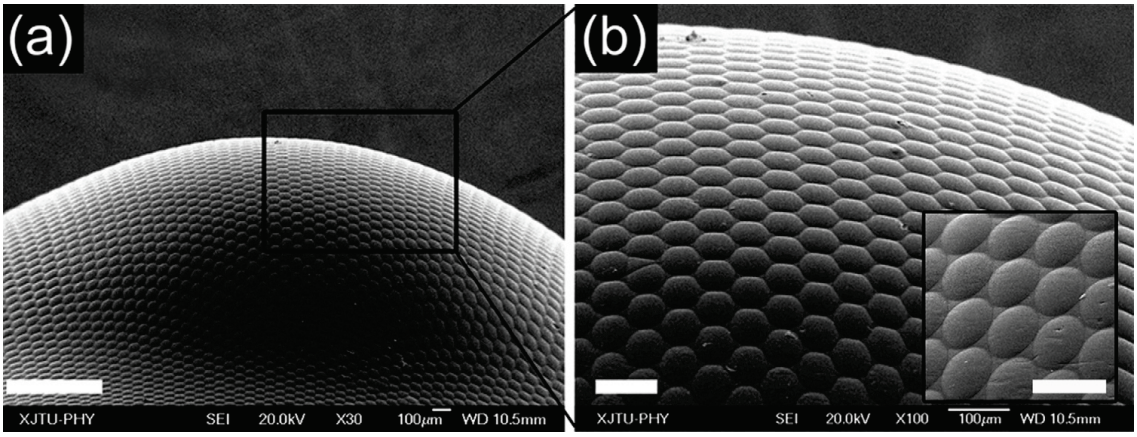

Figure 4*. (a) The morphology of the omnidirectional microlens array observed via an SEM. The scale bar is 1 mm. (b) SEM observation of the microlenses on the top of hemispherical shell. The scale bar is 100 lm. Inset: the microlenses on the outer ring of the dome (the scale bar is 100 lm).*

Fully functional, insect eye-like PMMA hexagonal gapless lenses on a curved spherical surface with radius of 3.5 mm have been recently (2012) reported by Liu *et al.* [9] as shown in figure 4. They prepared a planar intermediate PMMA film with lenses and then used heated spherical glass substrate, which remained inside the “eye” to shape PMMA sheet, and their assembly offers field of views greater than 170°.

Yet another quite successful set of experiments with PMMA and nanopatterned PDMS transferred onto highly non-planar ribs and a channels for use in microfludics was recently (2011, 2012) reported by Farshchian *et al.* [10-12]. After not so successful attempts with UV curable resists, an ultrathin nanopatterned PDMS nano-stamp was used, together with brass or PDMS ribs, or another macro-stamp, to form structures in PMMA above T_g as shown in Figure 5.

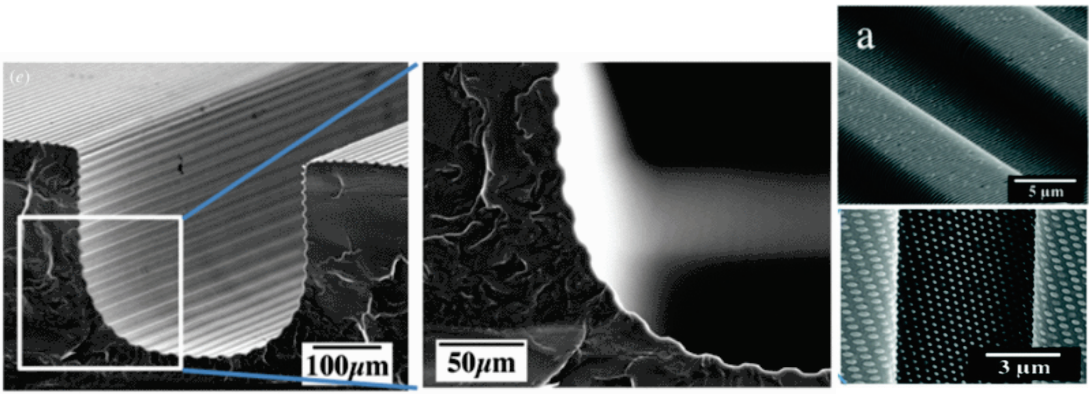

***Figure 5**. SEM micrographs of micropatterned sidewall of micfrofluidic channel and nanopatterns on channel sidewalls, modified from* [11,12].

In the last 2 cited works [11,12], by Farshchian *et al.* have the attempts to form micro/nano pattern on single curved surfaces been highly successful, even in the situation where a radius of curvature was fairly low. There are some problems with pattern distortions, double-curved surfaces and tearing thin PDMS nano-stamp, but overall it shows a very nice demonstration of current state of art. Note, however, that demonstrated results are formed in a PMMA polymer, thus cannot serve as an injection molding tool.

Injection molding

The most common and versatile of manufacturing process for plastic parts is undoubtedly injection molding (IM), shown in Figure 6. In principle, plastic granulates are fed via a barrel heated with a series of heating elements, that, together with friction, help in melting the polymer. Molten plastic is then injected by a reciprocating screw under high pressure into the mold cavity. Once the plastic part has cooled, the mold opens and the part is ejected to make room for another cycle. This process is semi-continuous, making the manufacturing of parts very affordable. It is well suited for a high volume, complex shape parts that have tight tolerances and, when optimized, can replicate mold structure down to the nanometer scale.

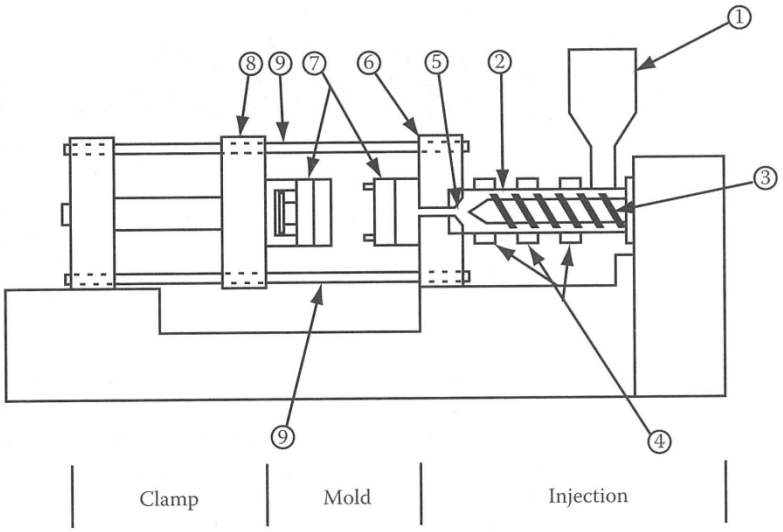

Figure 6. Schematic diagram of an injection molding equipment. 1. Hopper for plastic granulate. 2. Screw barrel. 3. Reciprocating screw. 4. Heating elements 5. Injection nozzle assembly 6. Stationary platen. 7. Standard two-plate mold assembly 8. Moving platen. 9. Tie-bars. Adapted from [13]

Molds are typically fabricated from tooling steel or aluminum. These materials have the strength to withstand high injection pressure, conduct and dissipate heat, and provide reasonable wear characteristics. Aluminum conducts and dissipates heat better than steel, making the cooling cycle shorter and more economic, but wears much quicker. Aluminum molds are much easier, faster and cheaper to machine, and material allows the use of fabrication methods that are otherwise incompatible with steel, such as single-point diamond turning[*]. As such, aluminum molds are mostly used for prototype tools or low volume parts.

Steel mold surfaces are usually covered with hard coatings, to limit wear and to prolong the lifetime of expensive tools. For this type of coating, thickness is much less important than hardness. Coatings not only protect the tool, they may affect the surface finish, thus the look and feel of the prepared part, and can affect polymer flow, mold filling, and de-molding. Classic coatings are usually a few hundred nm to a few µm thick. Most common "classic" coatings include electroplated hard chrome and electroless deposited nickel. More advanced coatings include Ni-Co alloys, deposited elecroless and therefore without the need to make a conforming anode that can be as complex and expensive as the mold itself. Another class of hard coatings are hi-tech coatings such as diamond-like-carbon, or PVD TiN, TiAlN, CrTiAlN, CrCN and alike, all of which are well suited for "classic" parts but with thicknesses of at least a few hundred

[*] Diamond is carbon, which reacts with iron in steel, leading to tool damage and dulling after short cut lengths.

nm such that they are not suitable for molds with nanopatterns as their purpose is different.

Perflorodecyltrichlorosilane

To prepare and successfully use nanopatterned IM tools, one has to take a different approach to coatings. Hardness and wear reduction are not on the top of priority list, but adhesion reduction combined with stability is. In the field of nanoimprint lithography, there are established processes to achieve good anti-adhesion properties on nanostructured stamps made of silicon, glass, quartz (SiO_2) or even PDMS. For this, stamps are often coated with self assembled monolayers. The resulting coating is then extremely thin, in fact, as the name monolayer suggests, only one molecule thick.

It is known that a perflorodecyltrichlorosilane, also known as FDTS, with formula $C_{10}H_4Cl_3F_{17}Si$ (for structure see fig. 7), can be used for this purpose. [14-18]. The chlorosilane head group reacts with hydroxyl (-OH) terminated surfaces of like SiO_2 and Al_2O_3 and forms a stable, covalent bond. The tail group, heavily fluorinated alkyl, brings in the desired functionality, dramatically reducing the surface energy of a newly formed surface.

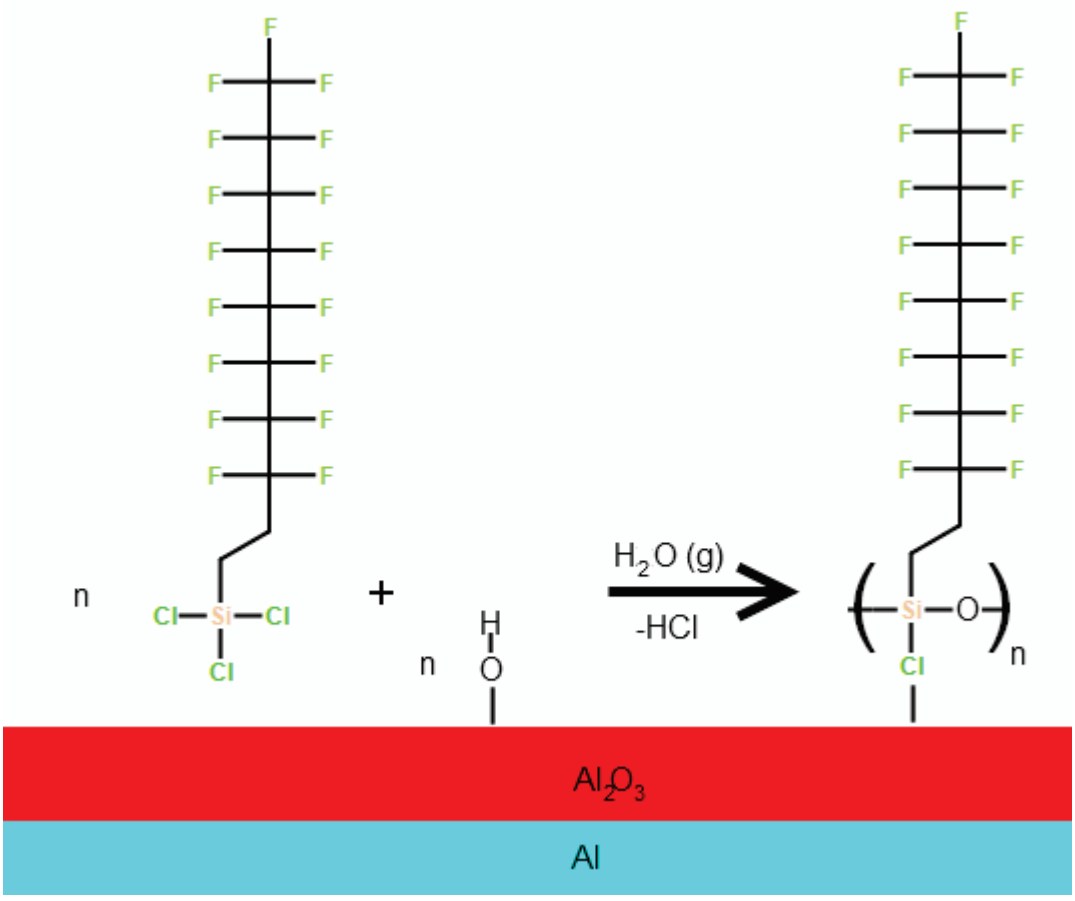

***Figure 7**. Schematic figure of the FDTS self-assembled monolayer formation on the surface of an aluminum injection molding tool.*

The reason why FDTS coatings are relevant for a micro- and nanostructured injection mold coating is two-pronged. First, small but critically important features (see figure 8.), may be obliterated, if the conventional, few µm thick coating is use. To demonstrate, see recently published [19] a plastic injection molded device, which employs very shallow (100 nm) microfluidic channels to stretch single individual molecules of DNA so they can be studied with optical microscopy. This device would be impossible to create if the used mold coating completely overlays tiny 100 nm high ribs on the mold. It would be equally useless if it amplifies the height, making the ribs 300 nm high, as the resulting 300 nm deep channels would be inefficient for DNA stretching.

The second reason is de-molding or the adhesion reduction. Some functional nanopatterns, such as nanonipples from mosquito eyes, have very large surface/volume ratios. So, if the mold surface energy is not reduced, hot polymer may replicate the mold structure (if a varioterm process is used) but it may be impossible to release the final part, as shown in figure 9.

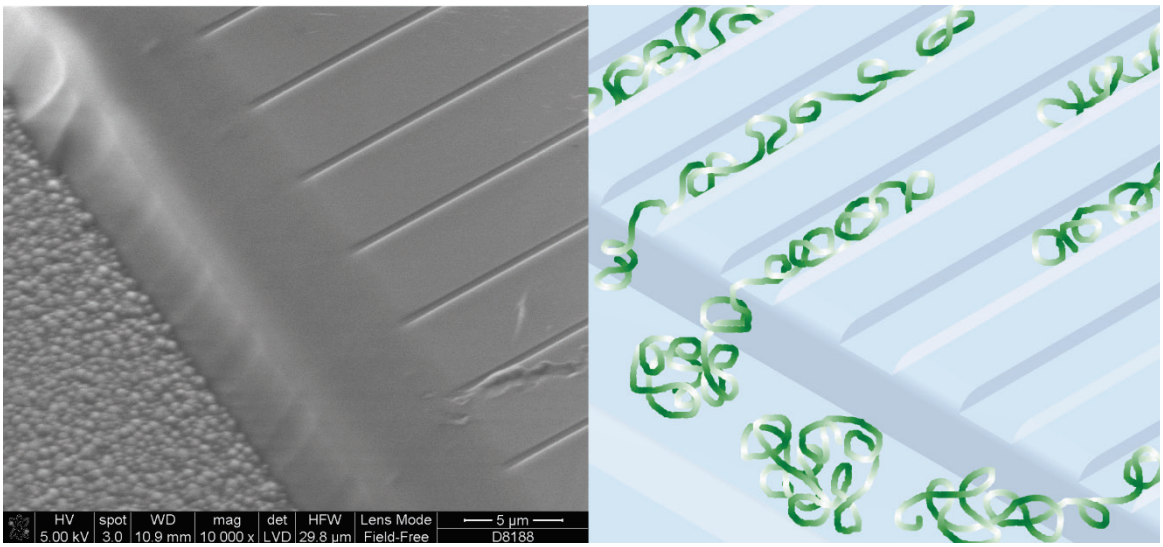

Figure 8*. Extremely shallow (100 nm) microfluidic nano-slits on an injection molded polymer device for elongation of DNA molecules* [19].

Those two arguments are a sufficient reason to study the stability of FDTS layers on the mold surface during real injection molding, as is presented in chapters 2 and 3 of this thesis and was published [20,21]. Our published results show that an FDTS monolayer is a suitable IM coating, and suggests that tools with nanostructured surfaces used to fabricate nanopatterned parts will work well, which was confirmed by a recent (Jan 2013) publication by Matschuk *et al.* [22].

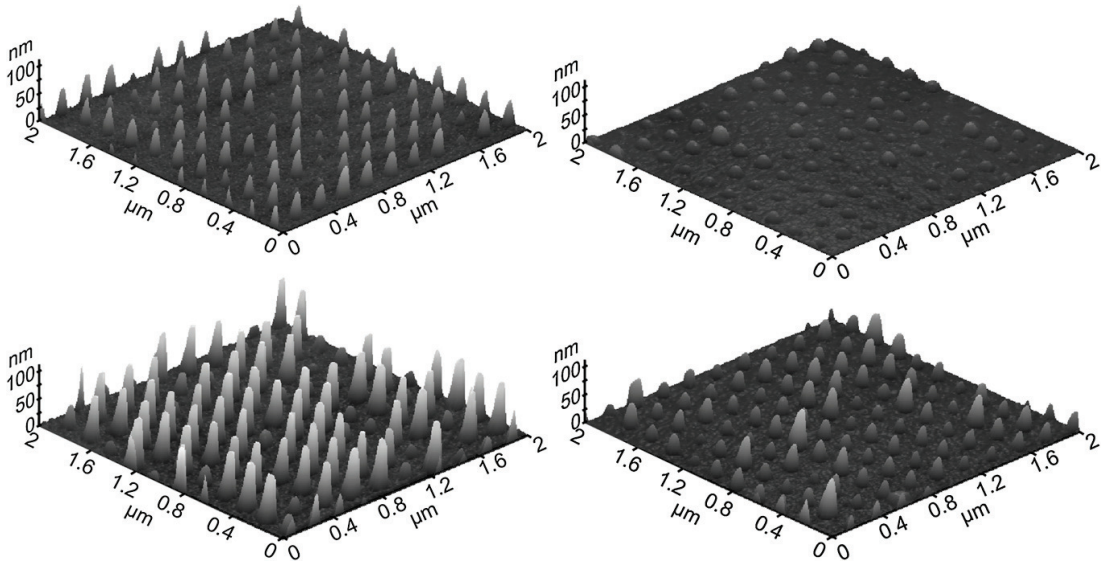

***Figure 9**. AFM micrograph showing the topography of polymer nanostructures, injection molded with (left) and without (right) FDTS coating on NiV mold. Mold temperature 60°C (top) and 90°C(bottom). Modified from* [22].

Silsesquioxanes and HSQ

If we search for nanoimprintable resists, sufficiently hard, tough and robust for the use as injection molds, silsesquioxanes turn up as a good candidate.

Silsesquixanes, a class of compounds with the empirical formula [$RSiO_{3/2}$] are just like nanopatterns. Their name comes from the 3/2 or one and one half of oxygen bound to silicon. They have been first synthesized in late 18th century by Ladenburg [23], and, in early 19th century, by Khotinski and Seregenkov [24]. In 1915 the hydrolysis and condensation of trifunctional silanes was studied by Kipping [25], but he concluded that polycondensation of "siliconic acids" leads to extremely complex mixtures of no synthetic value. This delayed further progress until the works of Brown and Vogt in the 1960s [26,27].

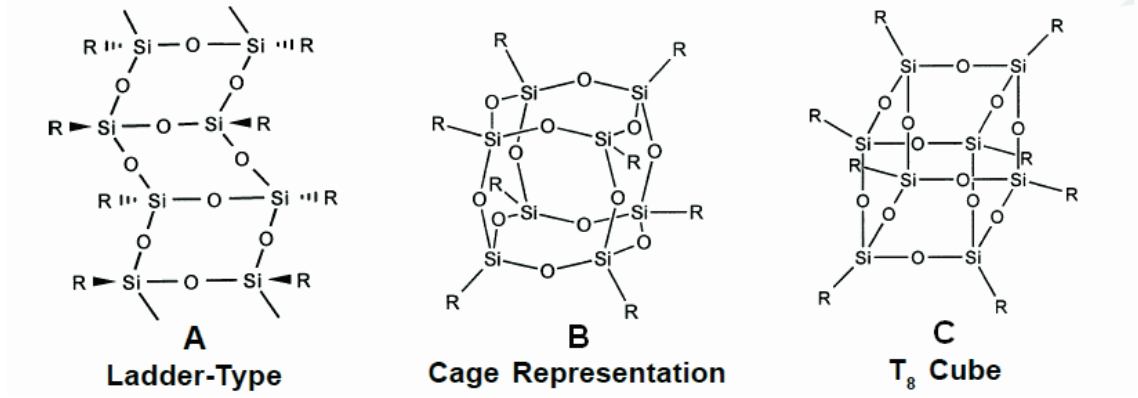

***Figure 10**. Structural representations of silsesquioxanes.*

There are several representations, as shown in figure 10, the most common one is the ladder-type structure (A) or cage-like (B), which is often drawn with an incorrect O-Si-O bond angle, shown as (C).

Substituents can be as simple as hydrogen, and then the hydrogen silsesquioxane (HSQ) is formed or a full variety of organic substitutents. When R is a polimerizable group, a whole new class of monomers, POSS (polyhedral oligomeric silsesquioxanes) becomes available. Again, just-like HSQ, they are extremely useful, and there is plenty of literature to benefit from. If we limit our focus on applications related to nanoscale patterning, there is a good review by Ro [28]. To briefly mention some stunning achievements, HSQ, when used as an e-beam resist, is capable of reaching sub-20 nm resolution [29], and, with optimized conditions, sub-10 nm [30]. To impress further, at 2012, a combination of He ion beam and nanoimprint was used to deliver 4 nm patterns [31].

In this work, HSQ is used merely as a room temperature nanomprint resist, which, when cured, forms a glass-like structure that is sufficiently hard to be usable as a mold or a mold insert for IM, thereby enabling affordable fabrication of non planar nanopatterned surfaces.

Objective

Concluding the information from Introduction we can now state the main objectives of this work, which, first, is to assess the stability of a monolayer adhesion reducing coating on actual mold surfaces, during the actual injection molding. And second, to fabricate non-planar surfaces with nanostructured patterns that are suitable for injection molding tools.

Chapter 2: Stability of FDTS monolayer coating on aluminum injection molding tools

Jiri Cech [1] and Rafael Taboryski [1*]

1. Department of Micro- and Nanotechnology, Technical University of Denmark, DTU Nanotech, Building 345E, DK-2800 Kongens Lyngby, Denmark

Abstract

We have characterized perfluorodecyltrichlorosilane (FDTS) molecular coating of aluminum molds for polymer replication via injection molding (IM). X-ray photoelectron spectroscopy (XPS) data, sessile drop contact angles with multiple fluids, surface energies and roughness data have been collected. Samples have been characterized immediately after coating, after more than 500 IM cycles to test durability, and after 7 months to test temporal stability. The coating was deposited in an affordable process, involving near room temperature gas phase reactions. XPS shows detectable fluorine presence on both freshly coated samples as well as on post-IM samples with estimated 30 at. % on freshly coated and 28 at. % on post-IM samples with more than 500 IM cycles with polystyrene (PS) and ABS polymer.

Introduction

The injection molding industry often employs prototype molds and mold inserts from melt spun (rapid solidification processing [32,33]) aluminum, especially for applications in optics [34,35], photonics [36] and microfludics. Prototypes are also used for verification of mold filling. The use of aluminum tools has reduced lead time (days instead of weeks) and manufacturing cost (30% of conventional mold). Moreover, for aluminum, a surface roughness (RMS) below 5 nm can be obtained with diamond machining [34,35,37]. Conventional mold coatings add cost and complexity, and coatings with thicknesses of a few microns can obliterate small features. The

* Corresponding author. Tel +45 21444236, rafael.taboryski@nanotech.dtu.dk

nanoimprint lithography community extensively uses functional monolayer coatings on silicon/SiO_2 lithographic stamps [14-18]. This treatment dramatically reduces stiction, and improves yield and quality of replicated nanostructures. Here we report on a fluorinated trichloro-silane based coating deposited on aluminum or its alloys by molecular vapor deposition. We have tested the stability of this coating in challenging conditions of injection molding, an environment with high shear stress from the molten polymer, pressures up to 200MPa, temperatures up to 250°C, and rapid thermal cycling.

Methods

The aluminum mold was machined from a solidified 6061 alloy. Samples have been cleaned in DI water, acetone, isopropylalcohol and blow dried in dry nitrogen.

The FTDS monolayer coating was deposited using a multi-cycle recipe [38,39] in a commercial MVD 100 system from Applied Microstructures. The chemicals were heated to about 50°C while the sample was kept at approx. 35°C. Process was started by O_2 plasma with 200 sccm flow at 250 W power for 300 s. This cleans and primes the surface [40,41], and ensures that aluminum is coated with aluminum oxide. The main cycle consist of four releases of FDTS at 0.5 Torr, one release of water vapor at 18 Torr and 900 s of reaction time. The cycle ends with five purge steps. The main cycle was repeated four times, resulting in a total processing time of approximately 80 minutes.

The samples were characterized by XPS and sessile drop shape analysis. XPS spectra have been acquired by a Thermo Fisher Scientific K Alpha, with the spot size set to the instrument maximum of 400 µm and a takeoff angle of 90°. Survey energy scan range was 0-1350 eV, with pass energy of 200 eV, 10 scans, and a collection time of approx. 660 seconds. XPS spectra have been collected on at least 3 spots on each sample, with spots at least 10 mm apart from each other to account for possible surface heterogeneity. Quantitative analysis of elemental composition from survey spectra and core levels deconvolution was done in the software package ThermoAdvantage version 4.75. The estimated relative error for the elemental quantification is below 1.8%.

A Krüss DSA 100S Drop Shape Analyzer was used to analyze the shapes of sessile drops of liquid on the sample surfaces. We used 3 liquids, namely water, benzylalcohol and diiodomethane to provide a sufficient number of pairs for the calculation of surface energy. Angles have been extracted 12 times from each drop during the first 6 seconds after deposition, with 4-10 good drops on each surface for each fluid.

The surface morphology was tested by a Dektak 8 stylus profiler from Veeco Instruments.

Moreover, the sample surfaces were also evaluated using DME DualScope C-21 tapping mode AFM with the resolution of 256 × 256 points. We used BS-TAP300AL probes with the probe force constant of 40 N/m. The topology data were collected from three regions (10.5µm × 10.5µm) on each of the investigated samples, selected regions being cca 75 µm apart. The scanned topology data have been processed with the provided DualScope/Rasterscope SPM software (version 1.6.2.5) using the following procedure: A central area of approximately 10 × 10 µm was selected, and a second order plane correction was applied prior to calculating the roughness parameters.

Injection molding to test wear stability was done using an Engel Victory 200/55 machine, with more than 500 IM cycles. First we tested 300 cycles using clear polystyrene, grade "Crystal 1810" (Total Petrochemicals) material, mold temperature 20°C and melt temperature 250°C, and then more than 200 cycles with proprietary yellow ABS material, mold temperature 90°C and melt temperature 320-340°C. Few initial shots have been used to set-up volume, speed, and briefly to optimize the filling and packing of the tested part for each material.

We also checked the temporal stability of the coating on the mold by leaving it exposed for more than 7 months at ambient conditions with exposure to direct sunlight, humidity and air pollution.

Results and discussion

We compared the surfaces of a pristine, uncoated control sample, with a sample freshly coated by FDTS, and with a sample used for more than 500 injection molding cycles. The stylus profiler data show no significant change in surface morphology and roughness, which is in accordance with the monolayer character of the perfluorodecyltrichlorosilane coating on the hydroxyl terminated aluminum oxide surface.

	FDTS coated			Post IM			Uncoated control		
region	A	B	C	A	B	C	A	B	C
S_A[nm]	4.48	3.98	1.82	1.92	2.59	1.09	2.03	2.72	4.15
S_{RMS}[nm]	5.80	4.80	2.25	2.38	3.82	1.80	2.59	3.57	5.48
S_{SK}	0.650	-0.028	0.460	-0.068	1.970	0.120	-0.660	-0.530	1.010

Table 1. *AFM surface roughness parameters. Root mean square height of the surface(S_{RMS}) and the arithmetical mean height of the surface (S_A) are low and does not significantly depend on a sample treatment. Skewness of height distribution (S_{SK}) values are fairly close to 0, therefore the surface roughness is relatively even, not dominated by tall spikes or deep voids.*

Surface roughness parameters obtained by AFM do not reveal any substantial change of surface morphology, with the mean S_{RMS} of 4.3, 2.7 and 3.9 nm for freshly FDTS coated, post IM and uncoated control samples respectively. Roughness parameters are shown in Table 1. The skewness of the height distribution values is close to 0, indicating a fairly even distribution.

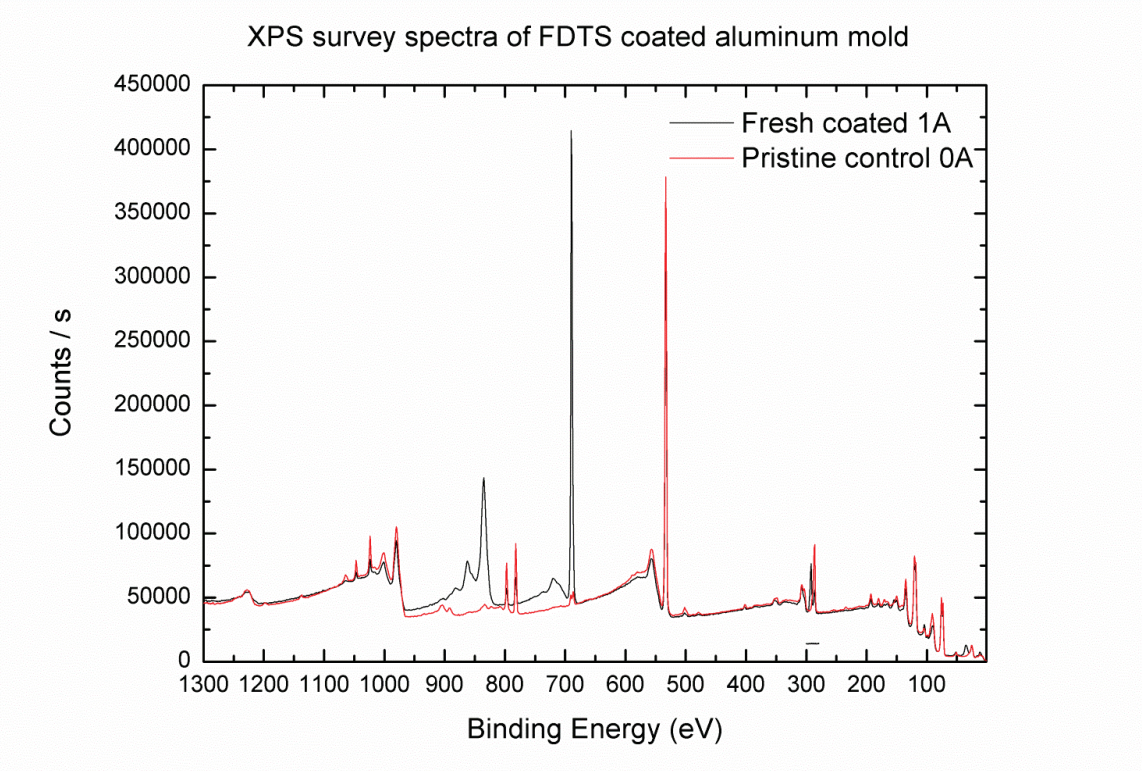

Figure 1. *XPS data, Survey spectra of coated (green line) and uncoated (red line) surface showing distinct F 1s peak at 689 eV.*

An elemental analysis from the XPS survey spectra (Figure 1.) shows strong presence of fluorine on freshly coated samples in comparison to uncoated control samples. This indicates that XPS is a well suited method to evaluate the coating state. Elemental quantification shows fluorine concentration of 30% at on the freshly coated surface and only slightly lower concentration on the post-IM mold surface, with 28% at. as shown in Table 2.

Name	Peak BE	FWHM eV	At. %
O1s	531.0	3.3	44.6
Al2p	72.3	5.1	34.2
C1s	284.4	3.2	19.4
F1s	685.1	3.8	1.8

Name	Peak BE	FWHM eV	At. %
O1s	533.1	3.2	31.6
Al2p	75.5	5.1	26.8
C1s	292.1	2.7	11.8
F1s	689.7	3.0	29.8

Name	Peak BE	FWHM eV	At. %
O1s	534.0	3.2	29.3
Al2p	75.9	4.8	19.1
C1s	287.2	3.0	24.0
F1s	690.8	2.6	27.6

Table 2. *Element quantification from survey spectra as a function of sample treatment, showing uncoated control (top), freshly coated mold surface (middle) and post IM mold (bottom), with fluorine concentration of 1.8, 29.8 and 27.6% atomic resp.*

This demonstrates that, FDTS coating prevails well in the harsh conditions of IM. Deconvolution of the C 1s core level spectra shown in Figure 2 and Table 3 reveals prominent high binding energy (BE) peak components at 294.47 eV and 292.13 eV, with FWHM of 1.04 and 1.48 eV respectively. Those high BE components can be attributed to the functional $–CF_2–$ and $–CF_3$ groups of the FDTS molecule. The ratio of peak areas is 6.89, very close to 7 as expected from the structure of the FDTS molecule shown in the insert of Fig. 2. Other, less prominent components at 290.3 and 287.6 eV arise from oxidized carbon species such as carboxyl group [42,43].

Name	Peak BE	FWHM eV	Area(P)CPS.eV	Area (N)	At. %	Q
C1s Scan A	292.1	1.5	12706.1	181	56.54	1
C1s Scan B	287.6	3.4	2196.92	31.23	9.75	1
C1s Scan C	285.9	1.9	4932.81	70.05	21.88	1
C1s Scan D	294.5	1.0	1844.31	26.3	8.22	1
C1s Scan E	290.3	1.2	810.59	11.54	3.60	1

Table 3. *Deconvoluted peak components of C1s spectra. Component A corresponds to -CF_2-, component D to -CF_3 and remaining components are described in the text.*

The peak at 834 seen on the coated sample arises from the Auger electron KL1 emission. This result is in fair agreement with XPS data presented in reference literature [42,44].

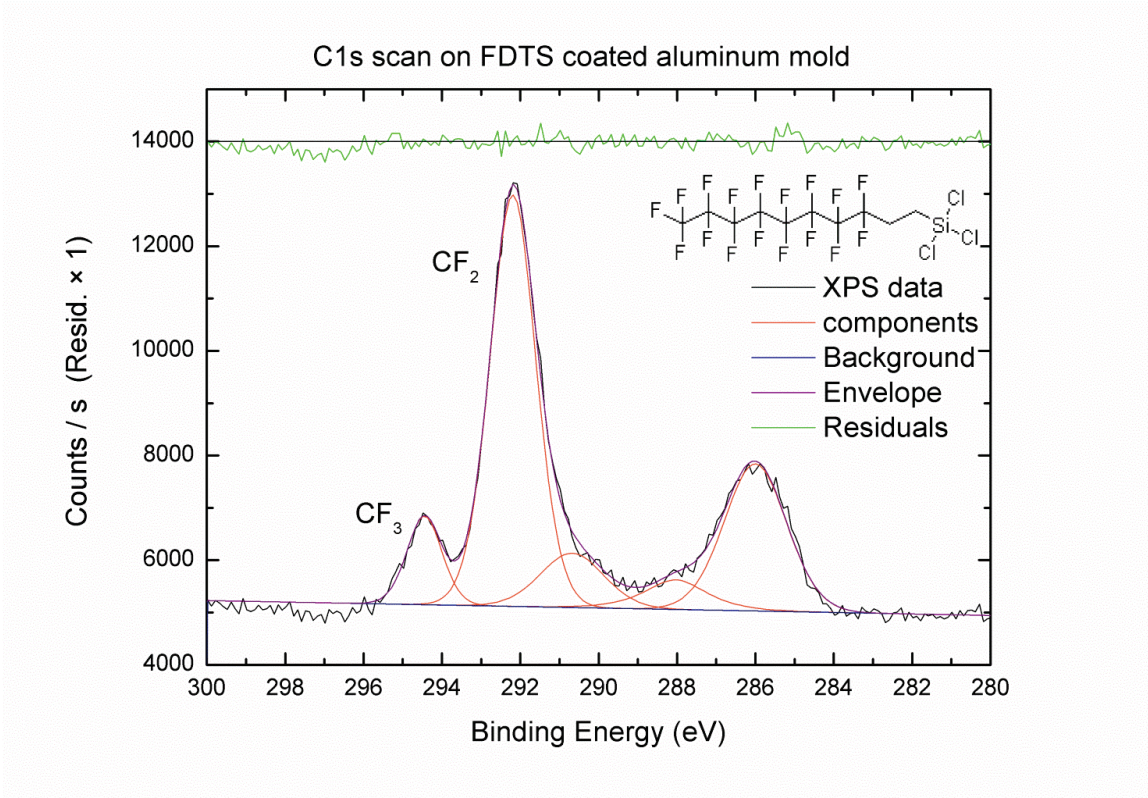

Figure 2. *Deconvoluted C1s spectrum, where ratio of D to A peak component areas (CF_2 to CF_3) is 6.89. This can serve as a specific fingerprint of FDTS coating presence. Insert: Structure of a FDTS molecule. Parameters of deconvoluted components are shown as Table 3.*

Sessile drop contact angles (CA) were again measured on multiple locations of the sample to account for possible heterogeneities. Each fluid drop was reproduced

between 4-10 times and measured 12 times during the first 6 seconds. Collected raw CA data are plotted in supplemental figures S1 to S3 (See Appendix A). Obvious outliers (often indicated by an odd drop shape on the surface and marked by star symbol) were excluded from the data before the variance was calculated from the remaining CA values for each liquid. This summary result is shown in Figure 3. The extracted error weighted contact angle data have been used to calculate the surface energies according to the extended Fowkes and Wu methods [45] using fluid pairs. SE results are shown in Figure 4.

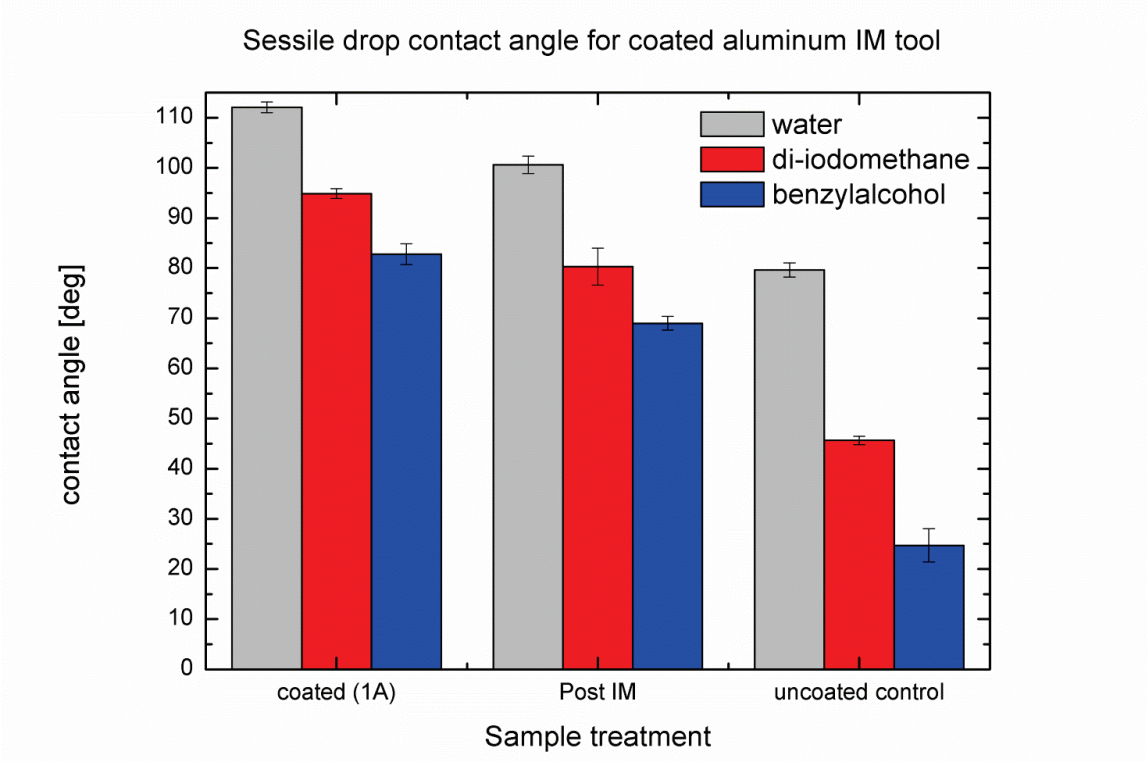

***Figure 3**. Contact angle measurement results for 3 different liquids as a funcion of sample treatment.*

The coating life expectancy seems to be between 2000 and 3000 molding cycles using a simple linear extrapolation from the calculated surface energy data. The same extrapolation from the XPS data gives a life expectancy of the monolayer coating of approximately 7700 cycles. There are arguments which may suggest that our life expectancy is too conservative, first, the wear of the FDTS layer seems to be slightly non-linear, with an initial wear followed by a relatively slow loss. The indication for this is the fact that we carried out a brief water-only sessile drop investigation of the surface after the first few IM cycles used to set-up the injection molding parameters and the results were comparable with the results obtained after more than 500 shots. Second, since we have a monolayer coating, removal of even one full monolayer of

coating in each molding cycle would result in total coating removal after the first full cycle, which was not observed.

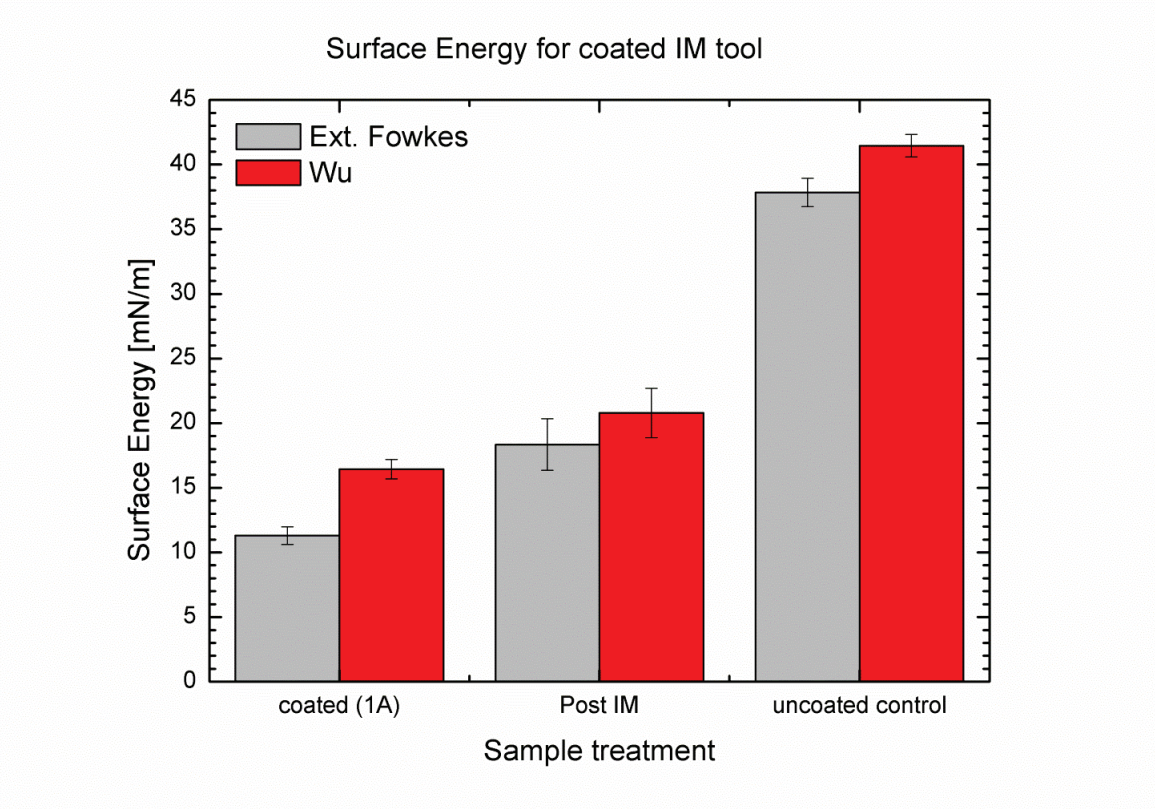

***Figure 4**. Surface Energy calculation result using pairs of liquids, according to Wu and Fowkes methods, shows dramatic decrease of SE after coating and survival of this surface modification for over 500 IM cycles.*

Moreover, if a need arise, the tool surfaces can easily be cleaned and primed by oxygen plasma and recoated with a new FDTS layer. Regarding the temporal stability, there was no observable degradation of the coating after 7 months exposure to ambient conditions.

Conclusion

The XPS spectral survey data confirms the presence of fluorine in both coated and post IM samples after 500 cycles. Covalently bonded FDTS coating molecules apparently prevail multiple injection molding cycles.

Sessile drop contact angle results show that the FDTS coating reduces surface energy by a factor 2.5 to 3.3, and this modification largely prevails over harsh IM cycling with enormous pressure and repeated temperature loading. The expected the coating lifetime was found to be 7700 cycles. Temporal stability is excellent as well.

In conclusion we have presented a mold coating deposited by molecular vapor deposition using off the shelf chemicals, and suitable for mold and tool manufacturing workshops. This coating is extremely thin, sub-nanometer monolayer, controllable, covalently bonded, reasonably durable, affordable, scalable to production, and detectable on the surface. It is especially suitable for rapid mold prototyping and mold geometry testing.

Acknowledgment

This work was funded and supported by DTU Nanotech, the Danish National Advanced Technology Foundation (HTF), project number 051-2008-3 and the Copenhagen Graduate School for Nanoscience and Nanotechnology (C:O:N:T). The authors would like to thank Dr. H. Pranov from InMold Biosystems for help with IM test and Dr. K. Nielson from DTU Danchip for help and fruitful discussion regarding XPS characterization.

Supplementary data

Supplementary data (namely the supplementary figures **S1**, **S2** and **S3**) associated with this article can be found as an Apendix A of this thesis

Chapter 3: FDTS stability on nickel and titanium injection molding tools

In this chapter I present results of FDTS monolayer coating stability during an injection molding. As we know from the previous chapter, FDTS coating on aluminum molds seems to prevail well even in a very harsh IM conditions, such as a rapid thermal cycling over hundreds of cycles, high pressure, high shear stress due to polymer melt flow and repeated de-molding. The main goal of this chapter is to verify if one can expect similar behavior with metals other than aluminum. To accomplish this, I selected commercial high-gloss nickel shim as one metal and sputtered pure titanium as another tested system. Both systems are highly relevant, just as aluminum is used for optics and microoptics molds, nickel is often used for preparation of microstructured molds for injection molded microfluidic devices and superhydrophobic surfaces, and titanium coatings are used in microfabrication.

Moreover, my secondary task in this chapter is to test the hypothesis that coating removal is in fact non-linear, which was suggested as a possibility in the discussion section of the previous chapter and questioned by the reviewer. To accomplish this, I decided to test the contact angle with all three selected fluids first after 200 cycles with cold mold and then again after another 300 cycles with heated mold. If the coating removal is strictly linear, one can expect a more dramatic loss between 200 and 500 cycles, than the loss in first 200 cycles. If the hypothesis of non-linear removal is correct to some extent, one can expect that the loss of coating will be less dramatic. As it turns out, loss is low, and the standard deviations of loss data are higher than observed changes, therefore does not allow for a conclusive answer.

I opted to test IM in-house, using resources of DTU Danchip, to achieve better control, and to test with 2 polymer grades and both heated and cold mold. I also decided to improve the presentation of contact angle and surface energy data and to devise another method to use XPS data for prediction of coating lifetime.

Some results presented in this chapter have been presented as a conference proceedings paper.

Methods

Methods used in this chapter are to a large extent identical to those presented in the previous chapter, with some notable differences which will be discussed below.

The tested **nickel** IM tool insert (shim) was approximately 370 µm thick and had a diameter of 85 mm. It was cut from a commercial highly polished Ni sheet, protected by polymer cover foil until used. Disc surface was carefully cleaned in a cleanroom with acetone, isopropyl alcohol and blow dried with dry nitrogen. This process was repeated three times to ensure that no residue of cover foil or possible adhesive is left on surface.

The tested **titanium** IM tool insert surface was created using identical nickel sheet substrate and subsequent sputter coating of its surface with a titanium metal. I used a Wordentec QCL 800 metal deposition system. After previous unsuccessful tests, I observed that the sputter target may contain more than only a thin layer of titanium dioxide, especially when stored outside the vacuum chamber for prolonged periods of time. This contamination resulted in the formation of a yellowish coating, comprised mostly of oxygen and titanium, ie. titanium dioxide, according to XPS data. Since adhesion of such coating is questionable as well as its composition, I choose to run in a batch mode with a full set of 6 wafers, and to put my nickel substrate on the last position, to ensure uniform target composition of pure titanium metal and a good adhesion. The process was carried out at 300W power and pressure of 0.01 mbar, which was reported to result in a deposition rate of 1.4-1.7 Å/s. Process duration, was selected to be 600 seconds, with an expected thickness of approximately 100 nm. This should be fully sufficient, as the XPS penetration depth is at least an order of magnitude less.

Injection molding was tested using the Engel Victory 80/45 Tech and a flat disc tool. This tool allows for the insertion of thin shim, which is our tested surface and produces polymer discs with diameter of 50 mm and thickness of 2 mm.

Each of the two coated metal substrates was in total exposed to more than 500 cycles. First, I used 200 cycles with a clear COC TOPAS (grade 8007S-04) and cold (20-30°C) tool. The polymer was plastified at 200 °C and injected at 250 °C. The state of the surface after this treatment is referred to as **IM 200**. Additionally, the same surface was exposed to another 300 cycles, again with a clear COC TOPAS (grade 5013L-10) and an elevated tool (mold) temperature, which was kept at 100 °C. The plastification temperature was set to 250 °C and the injection temperature to 280 °C. This puts the total cycle count at 500, therefore the state of the surface is referred to as **IM 500.** As before, few initial shots have been used to set-up volume, speed and briefly optimize mold filling and packaging for each tested polymer grade.

The perfluordecyltrichlorosilane (FDTS) coating procedure using an MVD system was identical to the one described in the previous chapter. Contact angle measurement and XPS characterization are essentially identical to the ones described in the previous chapter, with a maximum spot size of 400 µm. I did not systematically collected C1s

core level spectra, as the link between core level shape and the presence of fluorine was already established.

I omitted surface characterization with mechanical profilometer, as it was shown not to bring any additional information; instead I collected more data using the DualScope C-21 AFM microscope. Settings were identical as to the previous case, but I used 4 regions (10.5 µm × 10.5 µm) on each sample and treatment. Regions are cca 50 µm apart, in the corners of a square, using the maximum offset of the piezo elements.

Results and discussion

I compared titanium and nickel surfaces with and without an FDTS monolayer coating, and same FDTS coated surfaces after 200 IM cycles and after 500 IM cycles.

First, I tested surface morphology and roughness, as recorded by AFM. One can easily see that changes to topography (if any) are not significant, as shown in Table 1. This is not quite surprising, since FDTS monolayer coating thickness is expected to be just 1 molecule, if we consider the C-C bond length in Alkanes to be 154 pm, a decyl, 10-member chain is supposed to be only approximately 1.5 nm long. Since the initial roughness is bigger than this, we can hardly expect to see the change, which is indeed not the case. One can see that initial roughness of sputtered titanium is higher than that of nickel, probably as a result of the deposition process. In any case, roughnesses are fairly low, below 10 nm, which is in good agreement with the perfect mirror-like appearance of tested surfaces.

metal	**Nickel**						**Titanium**					
treatment	control		FDTS		IM500		control		FDTS		IM500	
S_A [nm]	2.61	±1.13	4.29	±2.81	3.34	±1.14	6.11	±2.11	8.44	±0.94	6.99	±1.35
S_{RMS} [nm]	3.95	±1.92	4.84	±1.27	4.51	±1.08	8.94	±2.35	10.51	±3.31	8.71	±0.96
S_{SK}	0.44	±0.71	-0.11	±1.3	0.59	±0.47	-0.24	±0.29	1.54	±0.14	0.25	±2.11

***Table 1**. Surface roughness parameter for Ni and Ti IM tool, measured by AFM. SD is calculated from all measured regions with the same treatment (N=4). Root mean square height of the surface (S_{RMS}) and the arithmetical mean height of the surface (S_A) are again fairly low and do not significantly depends on a sample treatment. This is a predictable result given the expected single monolayer thickness of an FDTS coating. Skewness of height distribution (S_{SK}) values are again fairly close to 0, therefore the surface roughness is relatively even, not dominated by tall spikes or deep voids.*

Second, I measured contact angles on tested surfaces. Processed results for all three fluids and all sample treatments are shown in Figure 1. Compared to the previous chapter, I have also collected data at 200 IM cycles, to provide insight on coating removal linearity. Results are in a fair agreement with expectations, one can see that

contact angles of pristine control samples are always much lower than after coating same sample with an FDTS. After first 200 injection molding cycles, the angle is slightly reduced and then, after a total of 500 cycles (300 with hot tool) it is reduced further, in agreement with expectations.

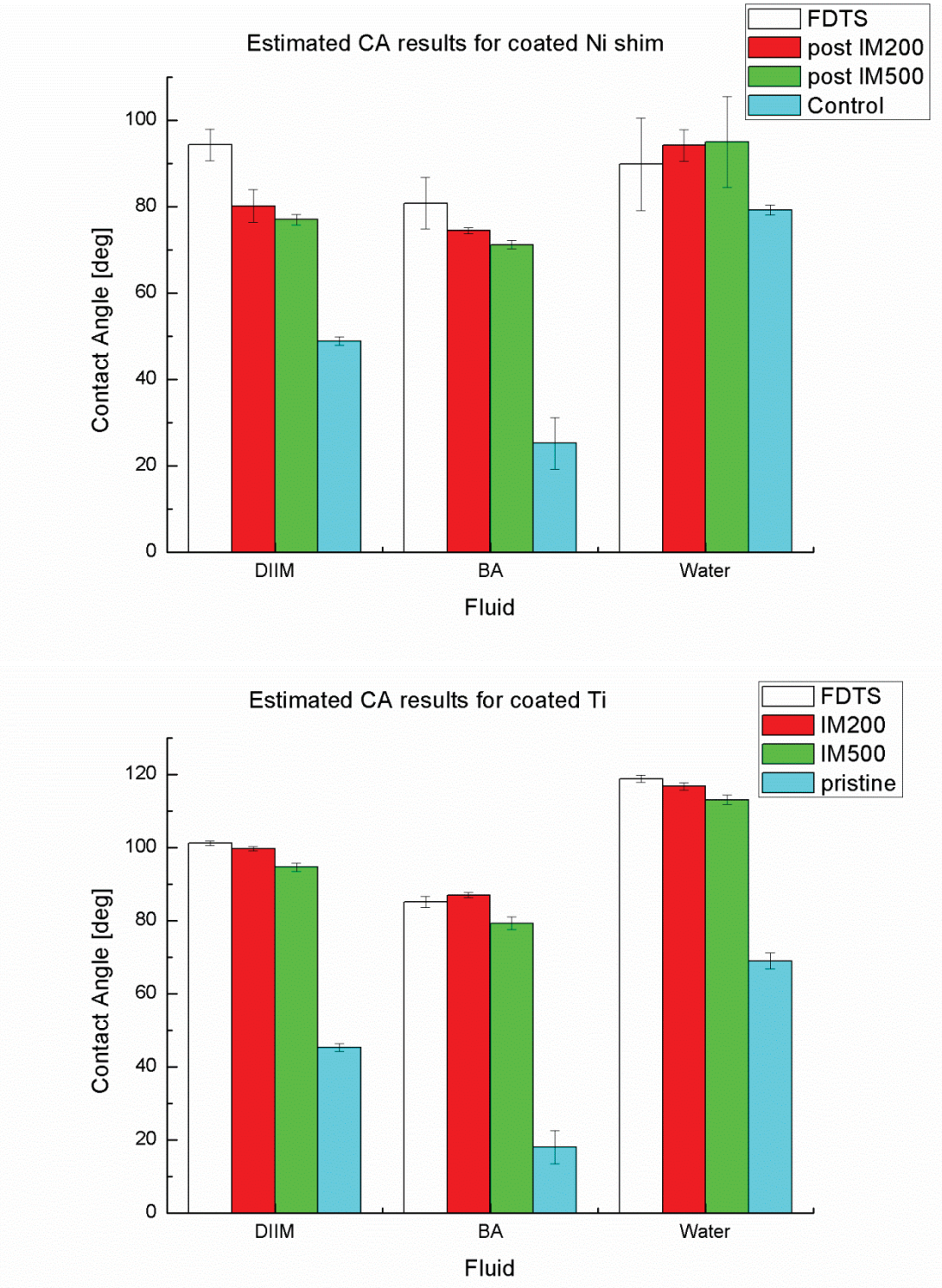

***Figure 1**. Processed contact angle measurement results for nickel and titanium surface (resp. their corresponding native oxides) and three different liquids (diiodomethane, benzyl alcohol and water) as a funcion of sample treatment.*

This general picture holds true for all cases with the exception of water and nickel tool and benzyl alcohol and titanium tool, where we see small, insignificant growth of contact angle, well within the error bars.

CA on freshly sputtered titanium surfaces (minutes from high vacuum chamber) has been too low to be measureable, well below 15°. However, it was an interesting observation, as the surface got contaminated by the ambient cleanroom atmosphere and hydrocarbons, in a few hours CA increased to the measureable values and remained stable for days and weeks. This effect is not the growth of native oxide, since the timescale for that is much shorter, by a few orders of magnitude. Same effect, Ti surface contamination in an ambient atmosphere on seconds to tens of minutes timescale was observed previously in literature [46-48].

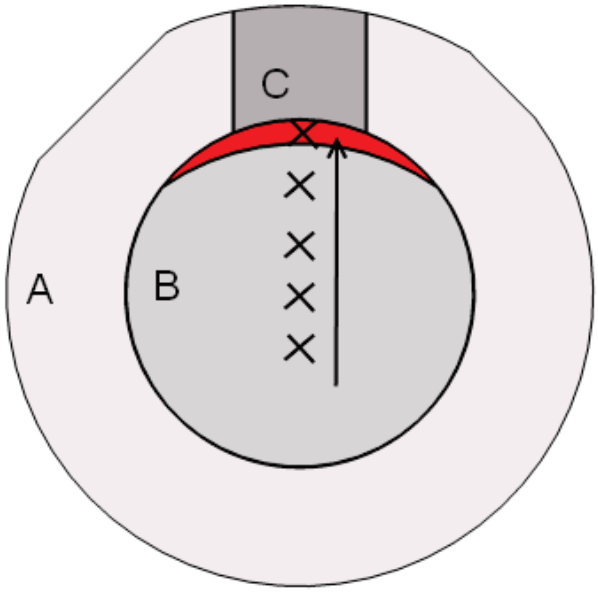

***Figure 2**. A sketch of the tested mold inserts. Diameter is cca 85 mm. Area A is not exposed to polymer flow, area B is inside a 50mm wide molding cavity, directly exposed to polymer, area C is a counterpart of tiny recess, a vent (air escape), in molding tool. Air in the cavity is escaping via this vent as cavity is being filled with polymer. Arrow and crosses indicate typical position of drops for contact angle measurwement. Red area is affected by excessive heating, so-called diesel effect, as I discuss the text.*

One can learn more details from the original raw data, shown as supplementary figures S4 to S9 in Appendix A of this thesis. There are notable groups of points with very low contact angle after the first 200 molding cycles. On figure 2 is a sketch of a tested shim, with a diameter of about 85 mm.

Drops for CA estimation are placed across the shim, and I noticed that the uppermost drops have a substantially lower CA. This mystery was much more visible while rinsing the molding tool insert with DI water or IPA, since apparently crescent like region on

the top (marked red on figure) was hydrophilic and was wetting well as opposed to the main part of the tool, which was still strongly hydrophobic, as expected for FDTS coated surface. If one also considers the position of a vent, and cavity filling, which can be seen on few initial incomplete shots, the whole mystery disappears. Air is rapidly compressed and heats up, especially if the air escape vent is insufficient and/or fouled by burnt polymer. This defect is well known in plastic industry, and is usually referred to as a diesel effect, burn marks, air burns. Temperatures in that small region can be high enough to burn away pieces of tool steel mold, and therefore it is not extremely surprising that the FDTS coating is fully removed and burned clean in that small region, which was confirmed by XPS quantification. This explains the local lower contact angle anomaly. In further investigation, I disregarded this small, non-representative region.

If one looks on Figure 1 again to assess if the coating loss (contact angle decrease) in a second molding set (cycles 200 to 500) is far more dramatic than in the first one (freshly coated to 200 cycles), an intuitive answer would be that it almost certainly is not. However, after I calculated surface energies using all contact angle data, the answer is that it is rather inconclusive since the loss, the differences themselves, are comparable and the standard deviations are larger than those differences.

To summarize result of CA measurement and surface energy calculations I show Figure 3, where is plotted a comparison of two metal materials (Ni, Ti) investigated in this chapter together with Aluminum from previous chapter. Result presented in this figure show that FDTS coating prevails not only on Al but also on Ni and Ti substrates for at least 500 IM cycles.

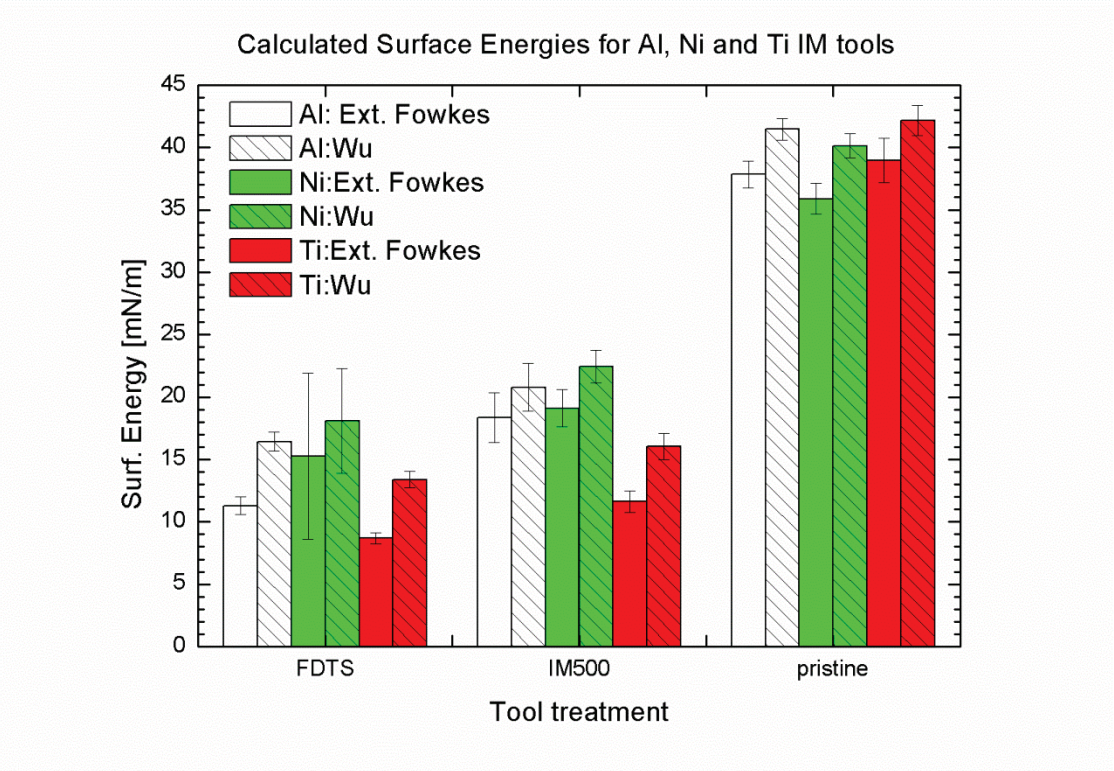

Figure 3. *Calculated Surface energies for aluminum (white), nickel (green) and titanium (red) using extended Fowkes (blank) and Wu (slanted lines) methods demonstrate that FDTS coating prevails for at least 500 IM cycles.*

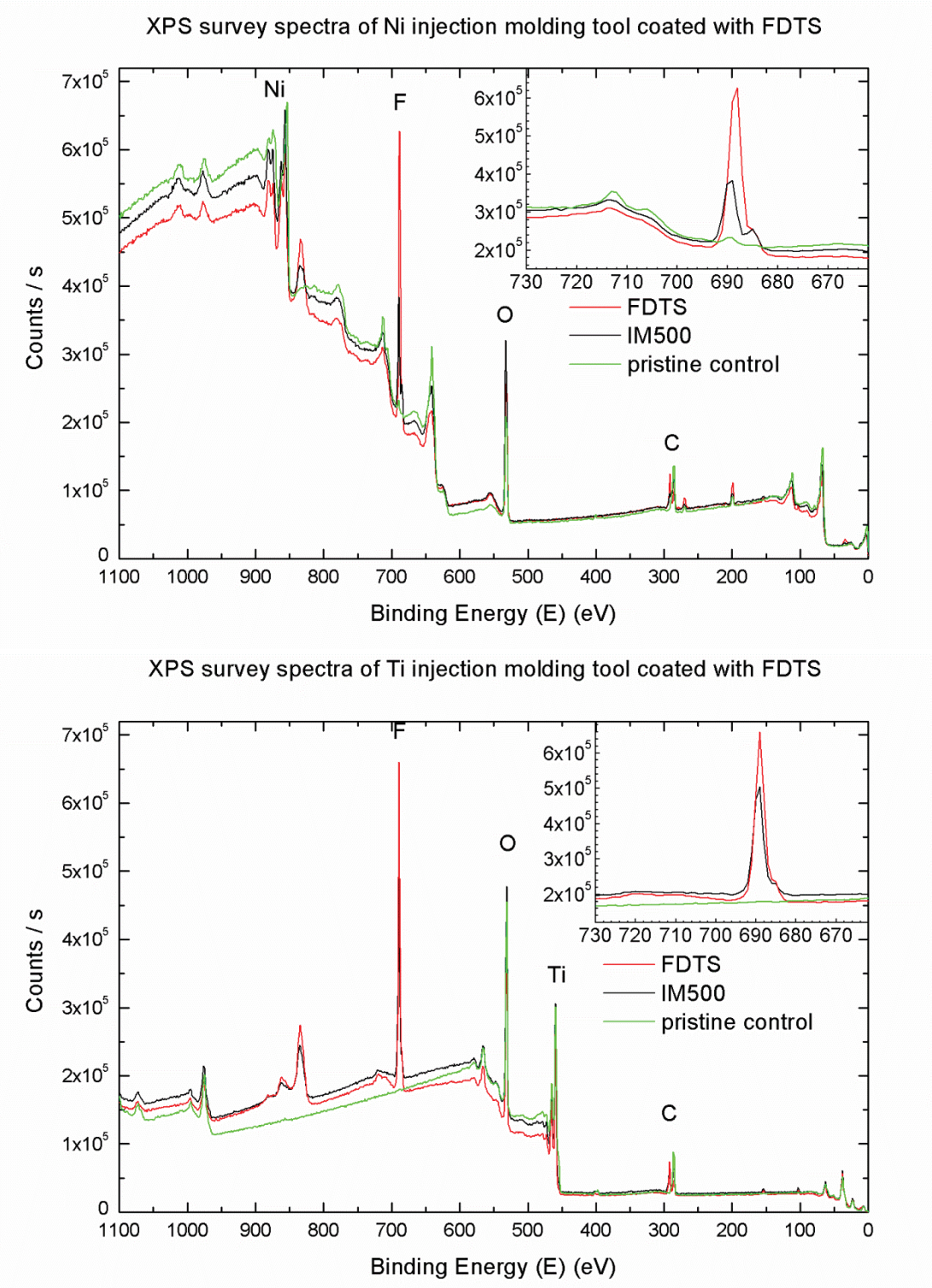

Figure 4*. X ray photoelectron spectroscopy survey spectra of tested surfaces, showing freshly coated (red), used, post 500 injection molding cycles (black) and uncoated control (green). One can see that even in the post IM state there is a well detectable contcentration of fluorine on both nickel (top) and titanium (bottom). This clearly indicates that at least some part of the FDTS coating prevails.*

I collected XPS survey spectra for both metals samples investigated in this chapter before FDTS coating, on freshly coated samples and after 500 injection molding cycles. Unfortunately, it was not possible to measure XPS after only first 200 molding cycles. XPS is in principle a non-destructive method, but the sample stage in a Thermo Fisher Scientific K Alpha is limited to a sample size of approximately 60 × 60 mm, and the tested mold inserts are circular with diameter cca 85 mm.

The survey spectra, presented as Figure 4, show that there is a detectable fluorine concentration on freshly coated and used samples. One can attempt to quantify how much fluorine, hence FDTS, is present. This quantification for nickel, titanium and aluminum sample is shown in Table 2.

Treatment	**Metal**		
	nickel	aluminum	titanium
FDTS coated	35.5%	29.8%	38.7%
post IM 500	20.5%	27.6%	27.5%
pristine	1.1%	0.9%	0.0%

***Table 2**. Detected concentration of fluorine (in at.%) from survey spectra as quantified by the ThermoAdvantage software package. Estimated error is below 2%.*

If one analyzes loss of fluorine, corresponding to the loss of FDTS coating, over the first 500 cycles, one can see that the loss on a nickel substrate (44%) is much larger than the loss on titanium (29%) and aluminum (7.6%) substrates. One can use this loss to predict coating lifetime using linear extrapolation, assuming linear removal of monolayer coating. However, this prediction depends critically on a quality of XPS quantification, purity of surface and a quality of collected spectra. There might be a better, slightly more robust method, taking in account not absolute fluorine concentration but the ratio of detected fluorine and underlying primary metal, i.e. nickel, titanium or aluminum. One can use those ratios for a linear extrapolation to estimate coating lifetime. This method should be less sensitive to surface contamination by for instance carbon, from polymers and injection molding lubricants. Comparison of this ratio/based method with other extrapolations is shown in Table 3.

Metal	**Expected FDTS lifetime**			
	Surf. En.		XPS	
	Ext. Fowkes	Wu	F conc	F/Metal
Al	1900	2800	7700	4650
Ni	2700	2550	1120	947
Ti	5130	5430	1735	1285

***Table 3**. Estimated coating lifetime using a linear extrapolation of changes in surface energy as calculated by two methods and based on XPS detected change of the fluorine concentration vs change in the ratio of fluorine to metal.*

Conclusion

I was able to observe an increased contact angle and to detect fluorine after 500 injection molding cycles (300 of them with a hot mold), which is evidence that at least a part of an FDTS monolayer coating prevails. This is true for both nickel and titanium. I can therefore guarantee minimal coating lifetime to be at least 500 cycles, which might be indeed sufficient for prototype mold or specialized devices. Moreover, since it is fairly simple to strip FDTS coating and re-coat same tool, it might be viable result by itself.

AFM data confirms, in agreement with expectation, that monolayer coating does not substantially alter topology of an underlying metal substrate.

Intuitive evaluation of observed contact angles supports the hypothesis about non-linear removal of coating. But, after evaluation and calculation of surface energies can one conclude the collected data cannot confirm or refute the hypothesis regarding non-linear removal of coating.

Analysis of the contact angle and surface energies, as well as loss of fluorine and a change in the ratio of fluorine to the metal may be used to predict coating lifetime. Linear extrapolation results from SE and XPS are in fair agreement within each method but not in good agreement when comparing those methods against each other. I would therefore suggest using the lowest of the coating lifetime estimates for each respective metal to be on the safe side. With this approach, we can rank substrate metals according to the expected coating lifetime to aluminum, titanium and nickel.

Supplementary data

Supplementary data, namely supplementary figures **S4**, **S5** and **S6** for nickel and **S7**, **S8** and **S9** for titanium, associated with this chapter can be found as the Appendix A of this thesis.

Chapter 4: Nanopatterning of highly curved spherical PMMA surfaces

Nanostructured, functional patterns created directly on double-curved surfaces allow for a variety of new applications *per se*. However, when combined with high volume replication methods such as casting or injection molding, such surfaces become sufficiently affordable for everyday use and may be used to enhance properties of common products.

This chapter covers initial tests with imprinting on non-planar surfaces. Substrates are flat and double curved spherical surfaces with a very high curvature (radius of just 1 mm), about 10 times more curved than the highest previously reported value in literature [5]. The selected material (PMMA) is not directly usable to form injection molding tools for further polymer replication, as the patterned surface is polymer, not a mold surface. It can, however, be electroplated or used for replica casting. The presented method relies on imprinting with a soft, flexible PDMS stamp, which conforms to the highly curved substrate. We demonstrate the feasibility of such patterning and show the importance of the fact that an intrinsically planar tool must conform to a double curved surface, which leads to a non-trivial and relatively high (up to 14%) distortion of a replicated nanopattern. This distortion was investigated, measured and compared for a thick and thin PDMS stamp.

Most of the experimental work was done during the Master thesis project of DTU Nanotech student Alexander Bruun Christiansen [49], where author of this thesis was co-supervisor. The main goals were: development of a technique for imprinting on double-curved concave and convex surfaces, test patterning on very highly curved surfaces, verification and classification of possible distortions, and testing the possibility to nanopattern the surface of polymer lenses without damaging their micro and macro structure.

Methods

The PDMS imprinting stamp was created in the usual way [50], using a 100 mm silicon wafer with nanostructured pattern as a master. This master surface was coated with a monolayer of Perfluorodecyltrichorosilane (FDTS), using the commercial MVD system and process described in detail in previous chapters, to ensure reduced adhesion effect. The Sylgard 184 base and a curing agent have been thoroughly mixed in the

usual 1:10 weight ratio in a disposable container. The mixture was poured onto the master wafer and degassed. This was accomplished by placing the wafer with PDMS layer into a plastic desiccator used *in lieu* of a vacuum chamber and exposing it to a vacuum for at least 30 minutes, to remove macro- and microscopic air bubbles from the casted PDMS layer. The PDMS layer on the master wafer was then cured at elevated (70°C) temperature for 6 hours. The master was placed in a slightly tilted position in order to achieve gradient in PDMS stamp thickness. After curing, the master wafer was removed and the flexible stamp was cut into smaller pieces of different thickness and characterized.

A PMMA solution was prepared by dissolving 15 wt% of PMMA beads in high purity anisole and prolonged (24+ hours) stirring. The molecular weight of used PMMA was 350k and the declared T_g was 105°C. Polystyrene (PS) used for bulk substrates prepared by an injection molding was identical to material used in Chapter 2, clear grade "crystal 1810" from Total Petrochemicals.

Non planar, high curvature and low surface roughness substrates for testing imprinting are not easy to obtain. The aluminum substrates used in this chapter were high precision, low roughness (R_{RMS} < 10 nm) spherical cavities and protrusion, specially designed for the fabrication of a polymer microlens array and single microlenses. All aluminum tools have been specially fabricated by Kaleido A/S. Actual profile of tools is shown in Figure 1. A photo of a tool with single microlens protrusion is shown in Figure 2 left.

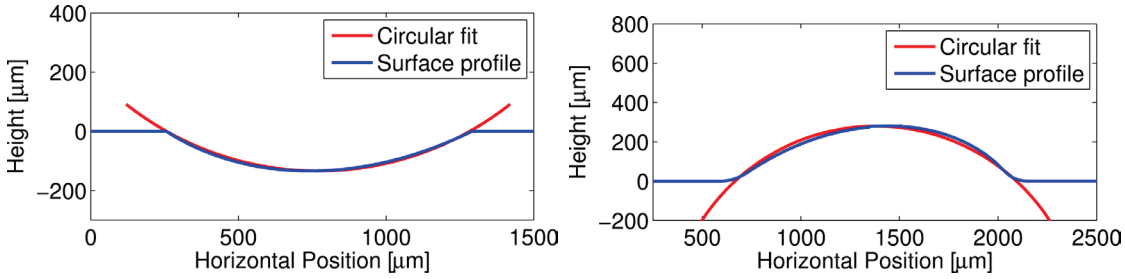

***Figure 1**. Surface profiles of used aluminum tools, as measured by stylus profiler. Cavity (left) radius was designed to be 1 mm, and the fitted circle radius (red) is 1050 µm. Maximum depth is 130 µm, the base diameter is 1000 µm. Protrusion (right) radius is 1050 as well, the maximum height is 280 µm and the base diameter is 1400 µm.*

Imprinting in hydrostatic pressure conditions, a perceived necessity for non-planar substrates, is a somewhat unusual requirement for most of the commercially available NIL systems. Typically, both stamp and substrate are flat and thin, imprint stack height is often well below 1 mm. This would not accommodate tested substrates, let alone their concave/convex surfaces. The Obducat NIL 2.5 Nano Imprinter (manufactured by Obducat, Sweden) is one of systems capable of a hydrostatic pressure operation. An

inert gas pressure is applied on a backside of a thin aluminium membrane, which is on topside of a soft PDMS stamp with nanopattern facing down to non-planar surface. See Figure 2. This allows the foil to conform to both the PDMS and underlying sample surface and deliver an even, uniform pressure on non-planar substrates. Typically, a pressure of 10 bars was used and dwell time was set to 2 minutes, imprint temperature was varied and cool down temperature, at which the pressure was released was set to 80°C.

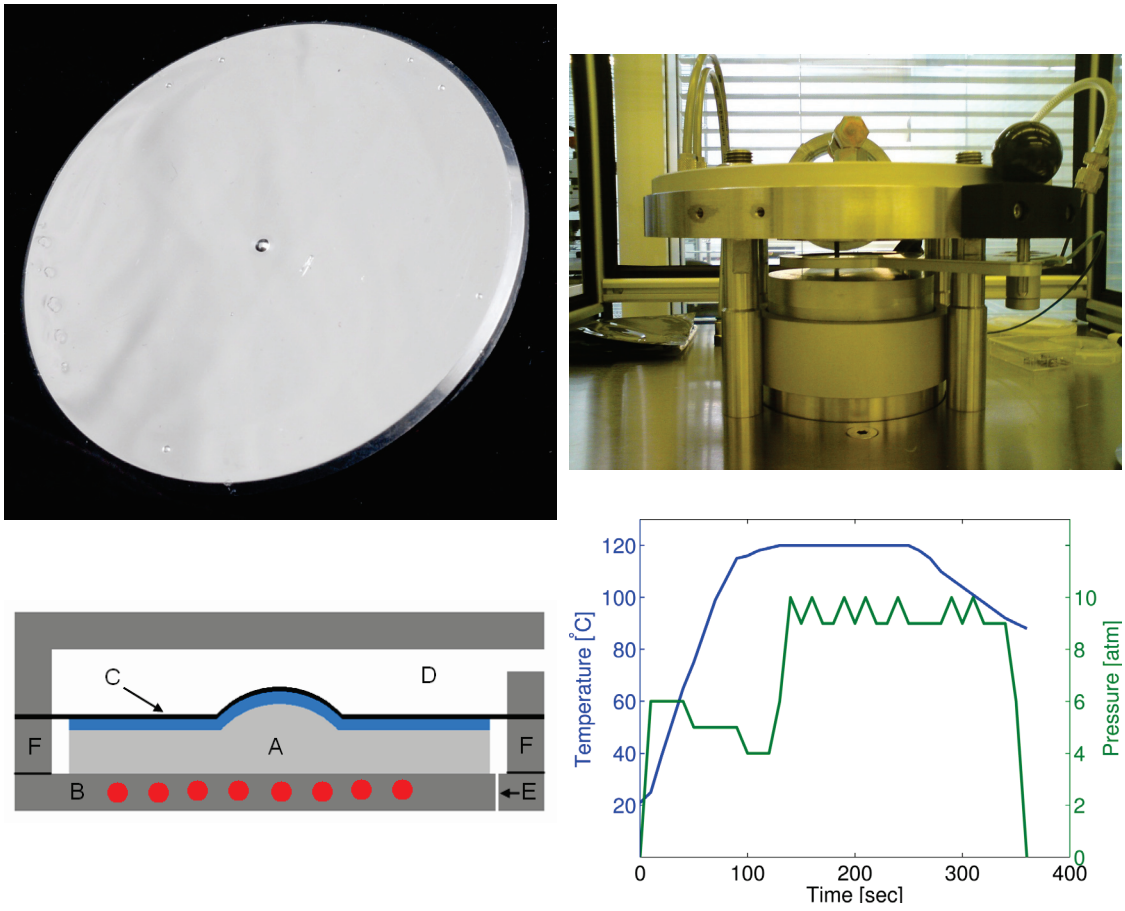

***Figure 2**. An aluminum tool and the Obducat NIL 2.5 nanoimpritner. Photos of the actual tool (left) and device (right) used in the cleanroom. A schematical figure (bottom left) to demonstrate the principles of operation. A planar or nonplanar substrate A with a PMMA resist layer and a flexible PDMS stamp is placed onto an electrically heated moveable piston B, which is then moved up, separated by a thin, disposable aluminum foil C, to close cavity D. This closed volume is then filled by a compresed inert gas at selected pressure. To accommodate for higher stack height, spacer F was used. E is a vacuum relief line used to avoid any pressure buildup below the separation foil. Bottom right panel shows pressure (green) and temperature (blue) during typical process. Pressure spikes are due to leak in the system.*

A Dektak 8 surface profilometer was used to collect height profiles of the substrates both before and after imprinting. The profilometer scans a mechanical stylus over the

analyzed surface, and measures the deflection. The scan is done in a single direction, and gives a line-profile of the surface topography. The diameter of the used diamond stylus is 5 µm, and the claimed vertical resolution at the finest range is only 1Å or 0.1 nm.

Two AFM systems were used for characterization of imprinted surfaces. First, in the DTU Danchip cleanroom, is the Nanoman AFM Dimension 3100, and second, the traceably calibrated system at Dansk Fundamental Metrologi (DFM). Both AFM systems were operated in tapping (intermittent) mode. It is important to consider that the vertical range of the piezo actuators for tip vertical movement is limited to 5 µm, due to their high resolution. This value might be easily exceeded, especially on highly curved surfaces. Recommended Z range for Nanoman system at Danchip is 2 µm which, in return, limits the X/Y range to 5 × 5 µm on the most curved samples. Another important consideration is that AFM processing software often fits data to a plane, either during post-processing or live, which may lead to the loss of information on most curved samples.

SEM use for analysis of tested surfaces was limited, as there were two issues. First, it remains nontrivial to image insulating samples like PMMA with sufficient resolution, and second, PMMA itself is sensitive to e-beam and its structure changes upon exposure.

Finally, during troubleshooting of the presented process, a high resolution X-ray computer tomography system Metrotom 1500 from Zeiss, located at Danish Technological Institute in Høje Taastrup was used.

Results and discussion

Results of initial imprinting experiments, where PMMA solution was spin coated either on a glass wafer or on an aluminum tool are presented in Figure 3. Those results are not on curved surfaces, they are collected on the flat part of aluminum tool, in the area between lenses and on a flat glass wafer. Initially, for a sample with post-spin curing at 110°C for 2 minutes, imprinting was successful also at temperatures 80 and 90 °C, well below the reported Tg of used 350k PMMA. This would be highly encouraging, as it suggests possibility to structure lens surface without damaging macro and micro geometry. However, follow up experiments, with curing at 180°C for 5 minutes, to warrant full removal of solvent, show that if there is no residual solvent (anisole), there is also virtually no imprint at temperature near Tg, such as at 100°C. One can see that it is possible to fully remove the solvent and still achieve imprint, but temperatures must be increased to 120 or 150°C. Another problem with curing at 180°C is formation of small bubbles in PMMA film, as this temperature is actually above the boiling point of anisole (154°C) at ambient pressure. To avoid this effect,

third curing temperature (150°C) was tested. This is below the anisole boiling point yet sufficiently high to remove all residual solvent from few micrometer thick PMMA film. Reliable imprinting with structure depth higher that 25% of stamp depth was demonstrated.

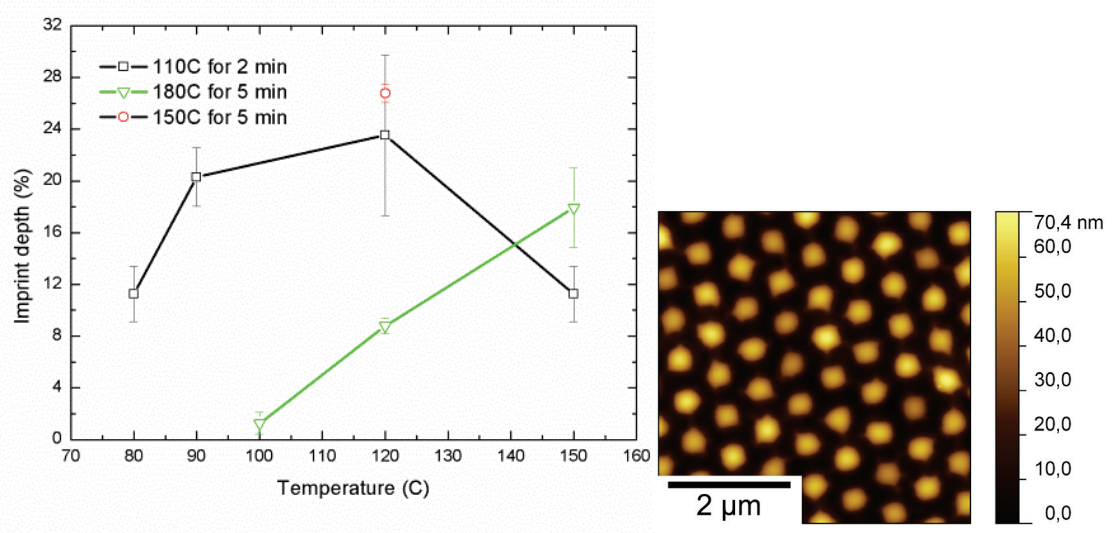

***Figure 3**. Depth of replication using a PDMS stamp and spin coated solution of a PMMA in anisole, shown here as a function of an imprinting temperature (left). Structure height/depth on a PDMS stamp is 239±10 nm. The first curve (black squares) shows results for samples cured for 2 minutes at 110°C after polymer spin coating. This suggests that there is a possibility of a replication even below T_g of the used PMMA (105°C) but it can be attributed to the insufficient time and/or temperature for total removal of anisole solvent, as confirmed by second curve (green triangles). Here the anisole was fully removed at 180°C for 5 minutes, and as expected there is practically no replication below T_g. Finally,the third point is PMMA cured at 150°C, below anisole boiling point, and one can achieve replication depth of 64 nm (27%). Left panel: AFM of the pattern replicated in PMMA at 120°C and cured at 110°C, showing nice, well defined pattern.*

After establishing imprinting conditions on planar substrates, we can move to non-planar surfaces, such as PMMA microlens arrays on glass wafers. Figure 4 shows process intended to prepare those imprinting substrates. Briefly, the intended process consists of spin coating the PMMA solution onto an aluminum tool with cavities, planarizing it, curing at the previously established temperature and transferring to a glass wafer prior to imprinting. Described steps apparently work, and curved PMMA substrates on glass have been prepared. However, after attempting to imprint nanostructures on the surfaces, something odd was observed. The polymer lenses did not behave like lenses anymore, and they appear to be somehow crushed and collapsed. Profile of such structure measured by Dektak is shown as the left panel of figure 5.

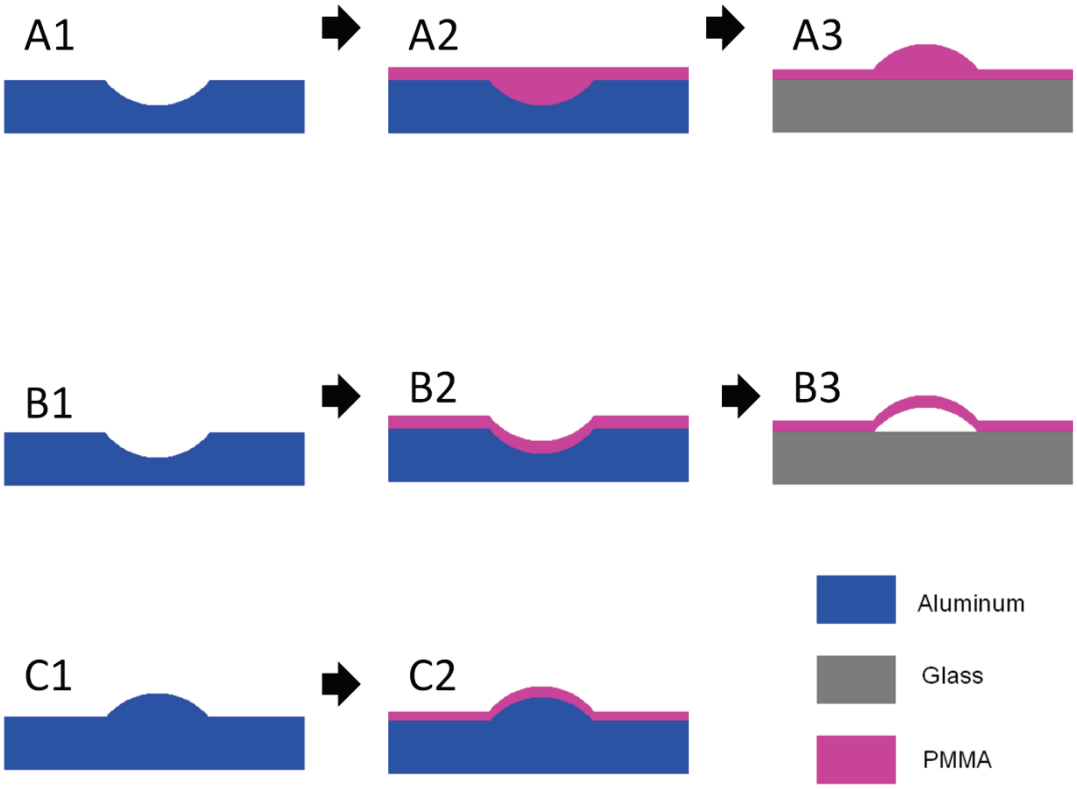

***Figure 4**. Non-planar polymer substrate preparation steps. Top line, panels A1 to A3 show intended process for the preparation of bulk PMMA microlens array on glass substrate. The FDTS coated aluminum tool is spin coated with a high viscosity PMMA mixture, and then the cavity replica from polymer is transferred onto a transparent glass substrate. Middle line, panels B1 o B3, shows actual outcome of the process. The PMMA coating is conformal rather than planarizing, despite being of a high viscosity. This results in a formation of polymer shells, rather than bulk microlenses. The mechanical strength of such shells is insufficient to withstand additional nanoimprinting. Bottom line, panels C1 to C2 show the process used for forming the PMMA layer on a rigid non-planar substrate using spin coating. This system was used to test embossing and to study pattern distortion.*

This profile of a collapsed lens structure upon imprinting suggests that there might be a void between glass substrate and PMMA body of lens. This is evidenced by SEM micrographs of an individual lens cut by a scalpel, as shown in middle and right panel of figure 5. However, this is still rather violent method, possibly altering the structure. In addition, there still might be alternative explanation such as a solvent rich core vs. well cured skin on the surface of PMMA. We used an x-ray computer tomography, as another, fully independent, non-destructive method to characterize microlens array in its intact state. The results, presented in Figure 5, are conclusive and clear, confirming the presence of a void inside each individual lens. This can be explained using a second line of panels in figure 4, B1-B3, where the PMMA forms a conformal coating instead

of a planar layer, thus forming the observed void instead of a bulk lens. Despite my various attempts to remedy this issue, such as blade coating instead of spin coating and high temperature vacuum annealing, I have not been able to eliminate it fully. Therefore, the process shown as bottom line in Figure 4, panels C1-C2 was used. Here, the PMMA film was spin coated onto a protrusion on aluminum tool, *and left on that tool*. The tool then forms a rigid support, and the PMMA film on top is an anticipated nanopatternable spherical surface, both highly and double curved.

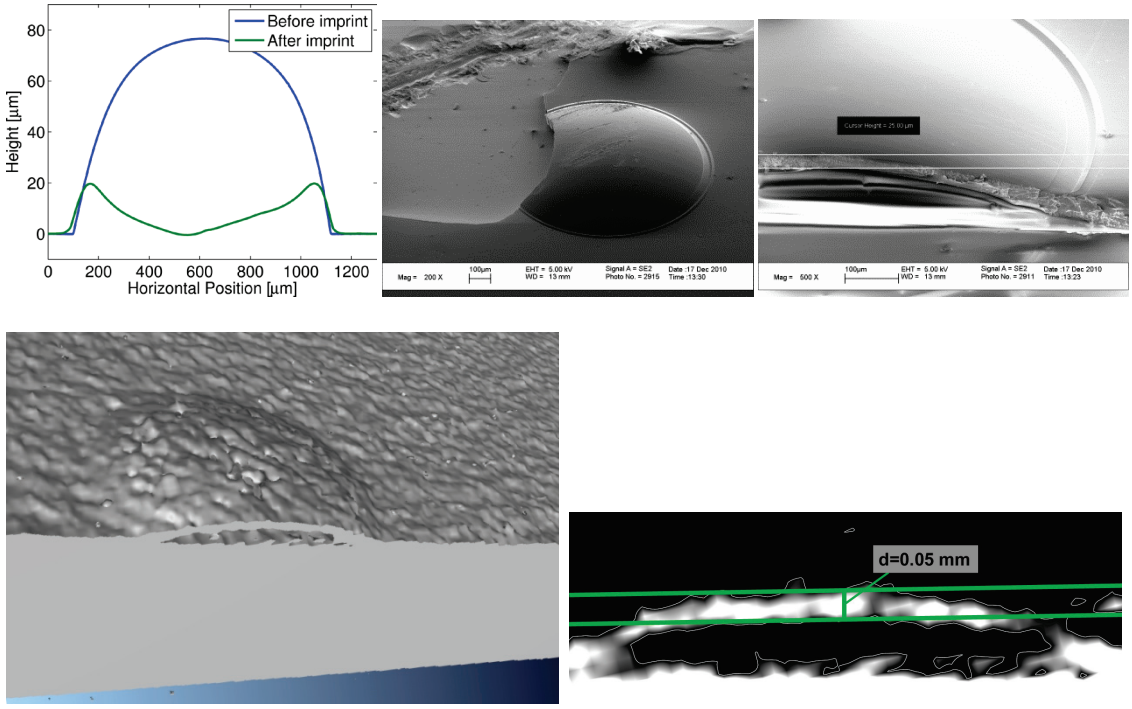

Figure 5*. Voids created inside PMMA shells. Top left: Profile before and after imprinting as measured by Dektak. Center and right: SEM micrographs of individual lenses cut by scalpel. Bottom: X-ray computer tomography measured on intact lens array, clearly proving existence of voids and thin shells.*

Imprinting on spherical PMMA films was carried out using previously established conditions, discussed in first paragraph of this section. PMMA was cured for 5 minutes at 150°C to avoid presence of any residual solvent, and then imprinted at 120°C and at 10 bar pressure for 2 minutes, with a cool down step to 80°C.

With the use of hydrostatic pressure and soft, flexible PDMS stamp, we can clearly see successful imprinting of nanostructures on a highly curved spherical surface, as shown in Fig 6. This is an important result as it exceeds the current record, established in literature approximately 10 times.

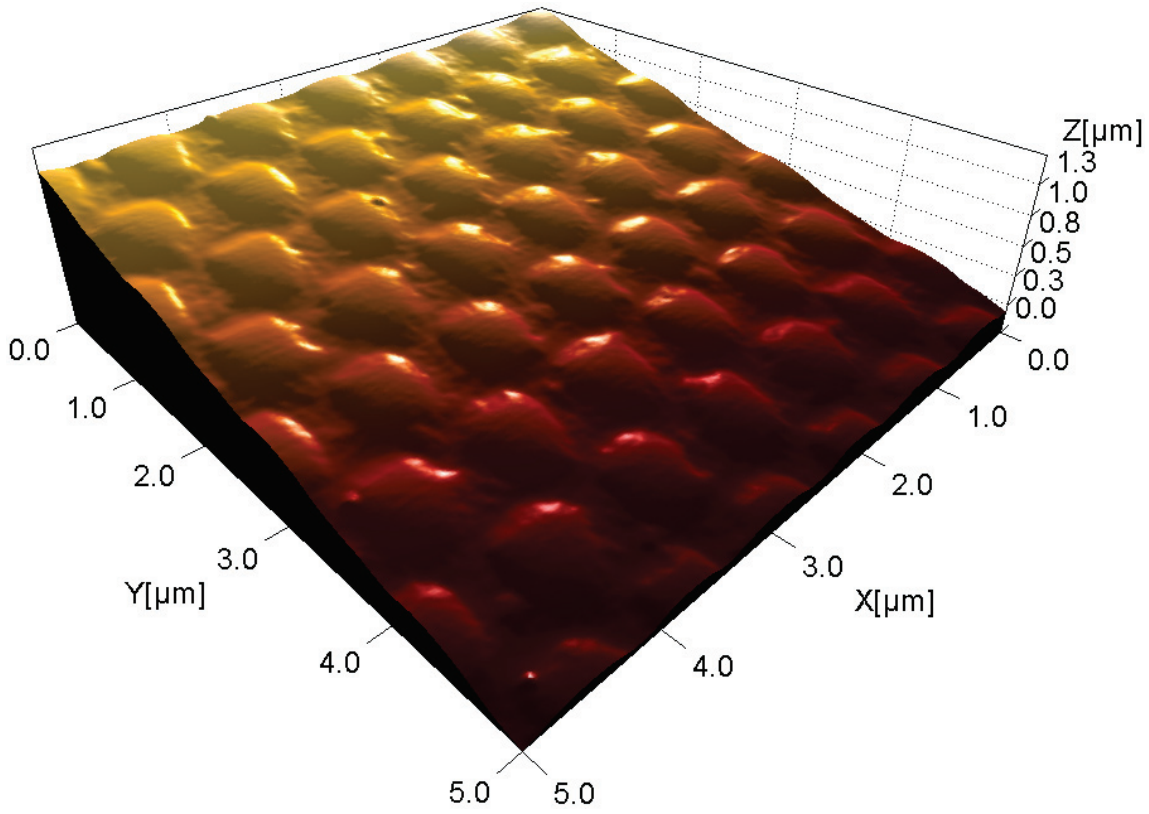

Figure 6. AFM micrograph showing a spherical PMMA surface with an imprinted nanopattern, recorded in the position B on figure 7.

Moreover, literature does not discuss any pattern distortion, which is rather unusual, provided that the intrinsically flat stamp has to conform to a spherical surface. With clear and well established imprint on the spherical surface we can proceed to detect and analyze pattern distortion. This is achieved by the comparison of the mean period (structure pitch) on the various positions of the imprinted spherical surface compared to the period on flat surface. Results of this comparison are shown in Figure 7. One can see a substantial difference when imprinting with a thin soft PDMS stamp (300 µm), comparable to the height of a protrusion, and when a thick (2000 µm) PDMS stamp is used. With a thin soft stamp, period stretch of 13 and 14% is observed at the apex of a protrusion. The area of the spherical cap is 16% larger than the area of the base circle. This corresponds to 7.7% larger mean period, if the strain is distributed homogeneously over the area.

This shows that the pattern distortion is non-neglible and has to be taken in account, and designed for, when a high precision is needed, such as for optical gratings and photonic crystals replicated onto a spherical surface.

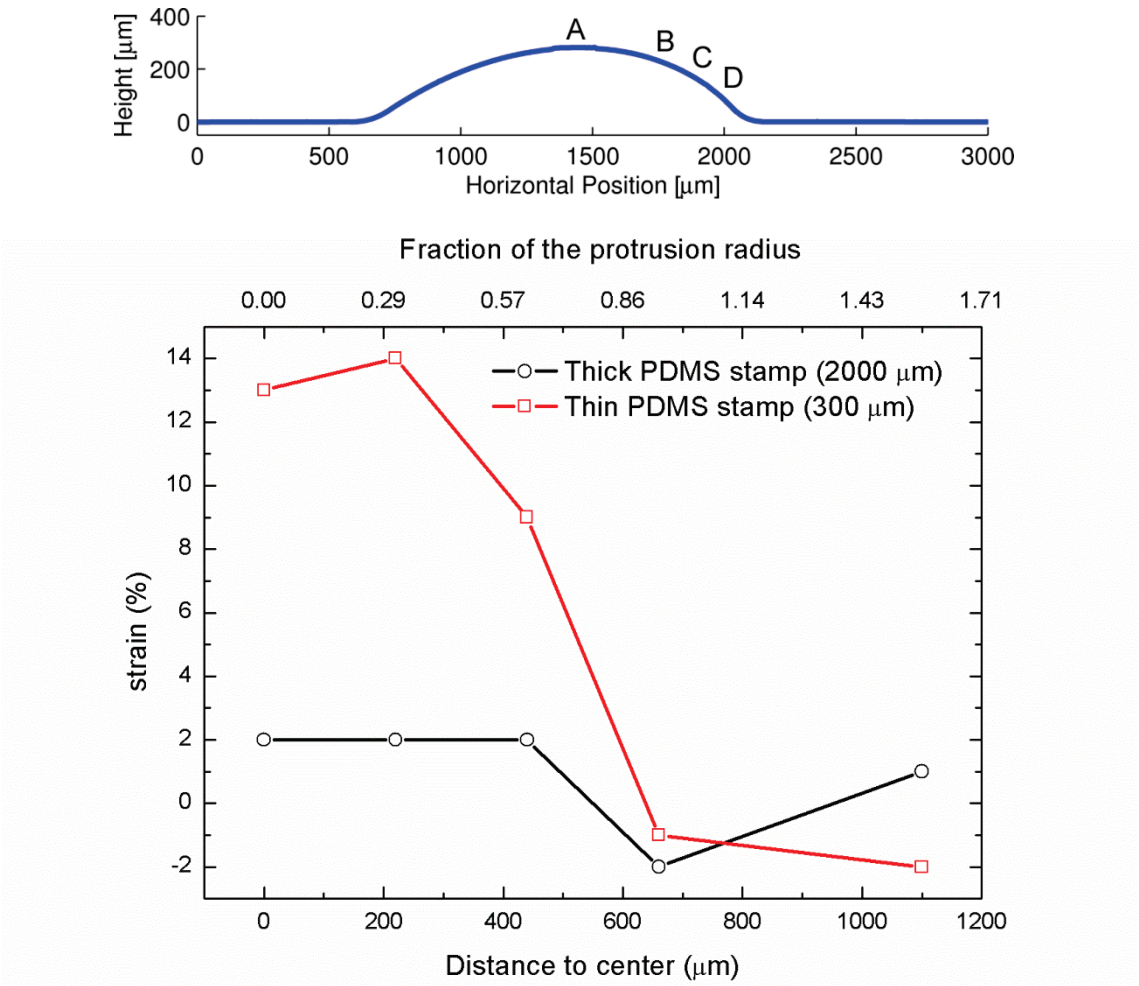

***Figure 7**. Distortion of the pattern on a spherical surface. A well replicated nanopattern was recorded in various positions on the spherical surface as indicated by the letters in the top panel. The pattern period is compared to the base period as observed on a flat surface. This strain is then shown on the bottom panel. One can see fair distortion (up to 14%) and also a dramatic difference between thick and thin PDMS stamp.*

Conclusion

To conclude the results collected in this chapter, one can see that; first, a process for imprinting with soft PDMS stamp into a few micrometer thick PMMA films was developed. This process uses NIL Obducat, which delivers hydrostatic pressure and thus is , in principle, capable of imprinting on non-planar samples. Second, a process to form highly curved non planar bulk PMMA microlenses on glass, usable as imprint substrates was tested, but collapsing of formed lenses during imprint was observed, analyzed, and explained. Third, as a solution, the PMMA solution was spin coated on a rigid aluminum substrate and imprintable highly curved spherical substrates have been obtained.

Structures as small as 420 nm were successfully imprinted on spherical substrate surfaces with the radius of curvature as low as 1 mm, using a hydrostatic pressure and a soft PDMS stamp. This result exceeds best value found in literature 10 times.

Due to geometrical difference between flat stamp and spherical substrate, a sizeable pattern distortion (up to 14%) was observed, in accord with expectations (mean of 7.7%). Moreover, a major difference in distortion between thick and thin soft stamp was measured.

Chapter 5: Surface roughness reduction using spray-coated hydrogen silsesquioxane reflow

Jiri Cech [a,b], Henrik Pranov [b], Guggi Kofod [b], Maria Matschuk [b], Swathi Murthy [b], Rafael Taboryski [*] [a]

[a] Department of Micro- and Nanotechnology , Technical University of Denmark, Building 345E, DK - 2800 Kgs. Lyngby, Denmark

[b] InMold Biosystems A/S, Gregersensvej 6H, DK - 2630 Taastrup, Denmark

Abstract

Surface roughness or texture is the most visible property of any object, including injection molded plastic parts. Roughness of the injection molding (IM) tool cavity directly affects not only appearance and perception of quality, but often also the function of all manufactured plastic parts. So called “optically smooth” plastic surfaces is one example, where low roughness of a tool cavity is desirable. Such tool surfaces can be very expensive to fabricate using conventional means, such as abrasive diamond polishing or diamond turning. We present a novel process to coat machined metal parts with hydrogen silsesquioxane (HSQ) to reduce their surface roughness. Results from the testing of surfaces made from two starting roughnesses are presented; one polished with grit 2500 sandpaper, another with grit 11.000 diamond polishing paste. We characterize the two surfaces with AFM, SEM and optical profilometry before and after coating. We show that the HSQ coating is able to reduce peak-to-valley roughness more than 20 times on the sandpaper polished sample, from 2.44(±0.99) µm to 104(±22) nm and more than 10 times for the paste polished sample from 1.85(±0.63) µm to 162(±28) nm while roughness averages are reduced 10 and 3 times respectively. We completed more than 10.000 injection molding cycles without detectable degradation of the HSQ coating. This result opens new possibilities for molding of affordable plastic parts with perfect surface finish.

[*] Corresponding author. Tel +45 21444236, rafael.taboryski@nanotech.dtu.dk

Introduction

Roughness of advanced polymer replication tools is costly and challenging to control, especially in case of complex geometries such as tools for freeform optical components, for microfluidic and medical diagnostics devices [19,51,52] or as substrates for nanopatterned surfaces. Such applications may often require special fabrication of molding tools. Low roughness surfaces fabricated by conventional means, such as abrasive diamond polishing or diamond turning, are often extremely costly. Hard coatings are often required to protect molds and to extend their lifetime. These coatings [53-55] are usually vacuum deposited [56,57] conformal coatings that simply copy an underlying topography, without affecting roughness. Electroplated coatings like hard chrome can even increase roughness. Wet deposited polymer coatings usually do not form sufficiently hard and durable films and the dip coating process may ruin fine features of a mold surface, such as microfluidic channels or micro- and nanopatterned regions.

Silsesquioxanes are small, cage-like, organosilicate molecules with the formula [$RSiO_{3/2}$], with three silicate bonds per silicon atom and one organic substituent R [58]. They tend to form cross-linked, organic-inorganic networks. Such networks may demonstrate features of both a hard, ceramic-like materials and features of a soft, organic material. Properties can be tuned and modified by processing to achieve for instance high final hardness together with solution processing or spin coating. There is a wide range of applications for this sophisticated material, such as optical coatings [59], dielectric insulators [60], barrier coatings, nanocomposites [61] , or lithography [62] to name a few.

Hydrogen silsesquioxane (HSQ), where the organic substituent R is simply a hydrogen atom, is an established lithographic resist [29,63] with good contrast and high sensitivity. HSQ resist in a solvent consist of individual cage-like molecules or a partially cross-linked, low molecular mass oligomer. Hence, it flows and can be spray-coated on planar and non-planar surfaces. It can be re-saturated with solvent to reduce surface roughness, as we show in this paper, or it can be (nano)patterned [64-66] . HSQ cross-links after curing and so forms a hard, fused silica-like structure. Patterned HSQ surfaces have previously been used as nanoimprint lithography masters [67]. Prerequisite to use HSQ for an injection molding mold is durability and robustness, which we tested. Hence, a mold comprising of such a cross-linked HSQ surface, is expected to be able to withstand a large number of injection molding cycles. Another viable use of spray-coated HSQ film is repair/refurbishing of injection molds as they are often extremely costly to replace.

HSQ mold surfaces can be coated with additional chemicals such as a monolayer of perfluorodecyltrichlorosilane (FDTS) which further reduces surface energy, sticking

and demolding force. While coating of SiO_2 [16,17,68,69] or cured HSQ [64] nanoimprint lithography tools with an antisticking/release layer is not new, it was suggested [70] and recently shown [71,72] that an FDTS monolayer coating can be successfully used to coat certain injection molding tools. This further reduction of the surface energy is important for a cost effective injection molding of complex and challenging articles such as nanopatterned superhydrophobic surfaces, where a successful part release remains a challenge.

Methods

We describe preparation of the metallic substrates, deposition, processing and curing of the HSQ film, sputtering of a reflective metallic film and characterization of the surfaces.

Substrates

Our testing substrates are the machined aluminum RSA 6061 alloy discs with a diameter of 33 mm and a thickness of approximately 3.7 mm, which may be used as an injection mold insert. The surface after machining was sanded with a series of sandpapers from Siawat fc, Switzerland for the grits P800, P1000, P1200 and from Rhynowet plus from Indasa, Portugal for the superfine grits P1500, P2000 and P2500. Sanding was performed in a wet state, using cca 10 minutes with each grit. Ceramic polishing paste MPA 11000/1 from Festool, Germany, corresponding to grit 11.000 was used on the appropriate sample for approximately 15 minutes. All surfaces have been carefully rinsed with acetone, isopropylalcohol and blow dried in dry nitrogen after surface preparation. Aluminum substrates have been cleaned immediately before spray-coating in the air plasma chamber for 15 minutes, using the chamber Diener Pico P100 from Diener Electronic, Germany to ensure perfect cleanliness and to reduce hydrocarbon contamination on the surface.

HSQ film processing

HSQ resist, FOX 16 from Dow Corning was applied using a spray-coating technique with an ultrasonic nozzle (Sonotek ExactaCoat with Impact spray nozzle). The resist passes through the nozzle and reaches the ultrasonically agitated nozzle tip, where it disintegrates into a mist. The mist is forced onto the sample surface using a carrier air stream. FOX 16 resist is mixed 1:10 with methyl isobutyl ketone as solvent, and then sprayed at a flow rate of 0.4 mL/min, with the robot passing the nozzle at 25 mm/s and line spacing of 0.88mm. Half of sample area was masked with cleanroom blue tape, and therefore not coated with HSQ.

Re-saturation with a solvent

Samples were transferred to the reflow chamber immediately after spray-coating. The reflow chamber consists of a bubbler bottle where inert gas is introduced to the MIBK solvent and then reintroduced back to the chamber to achieve fast exposure to the atmosphere saturated with solvent vapor. Samples are kept in the chamber for 30-60 minutes, at ambient temperature and pressure.

Curing

Samples were cured in an inert gas atmosphere oven, first for 8 hours at 70 °C to facilitate full solvent removal and then the temperature was ramped up to 400 °C for 1 hour to ensure full cross-linking. Heating was turned off and the oven temperature slowly ramped down to room temperature.

Sputtering of a reflective metallic film

To increase reflectance of the HSQ film and to avoid light transmission and reflection from the metal substrate, we sputter coated cured HSQ samples with a thin film of gold/palladium (80/20) alloy. We used the Balzers SCD 004 sputter coater, operated with 0.06-0.07 mBar pressure of argon. Samples have been processed for 240 seconds at 30mA current. A silicon wafer is always included to examine the effect of sputtering on roughness.

Characterization

We used a Sensofar optical profiler in the Vertical Scan Interference (VSI) mode with 5 scans per spot and a 100x DI interference objective. We selected our tested area to be approximately 85 x 85 µm, with the 512 x 512 pixels resolution, to be comparable with the AFM data. The pixel to pixel distance is 166 nm, comparable to the 176 nm for the AFM. Data was plane corrected. We measured 3 spots for each sample and treatment, each at least 2 mm apart.

We also characterized our sample surfaces in a tapping mode with an AFM PSIA XE-150. We selected the maximal area, approx. 90 x 90 µm and measured it with 512 x 512 pixels resolution, giving a pixel to pixel distance of 176 nm, comparable to the 166 nm for the optical profiler. We used a BudgetSensor aluminium coated tip. Collected AFM data was evaluated using XEI software, 1.8.0Build16 from Park Systems corp.

The samples were investigated in a Zeiss Crossbeam 1540 EsB. After transfer to the scanning electron microscope (SEM) the samples were tilted 54° relative to the beam. A focused ion beam (FIB) was used to selectively remove material from the samples in

ca. 10 µm wide trenches, revealing the profile, i.e. the inner structure perpendicular to the surface. The samples were imaged using 3 kV accelerating voltage.

Results and discussion

Aluminum disks having two different starting roughnesses were coated with a layer of hydrogen silsesquioxane (HSQ). The superfine sandpaper polished disk shows an initial area peak-to-valley roughness of 2.44(±0.99) µm while the paste polished disc shows 1.85(±0.63) µm. The HSQ layer was deposited by spray-coating, which is, unlike spin-coating, capable of coating non-planar surfaces and challenging geometries such as concave optical and micro-optical surfaces, molds for microfluidic devices and other geometries which would be impossible to polish by manual or mechanical means. Samples that have been spray-coated with HSQ and cured show considerably reduced roughness as shown in Figure 1.

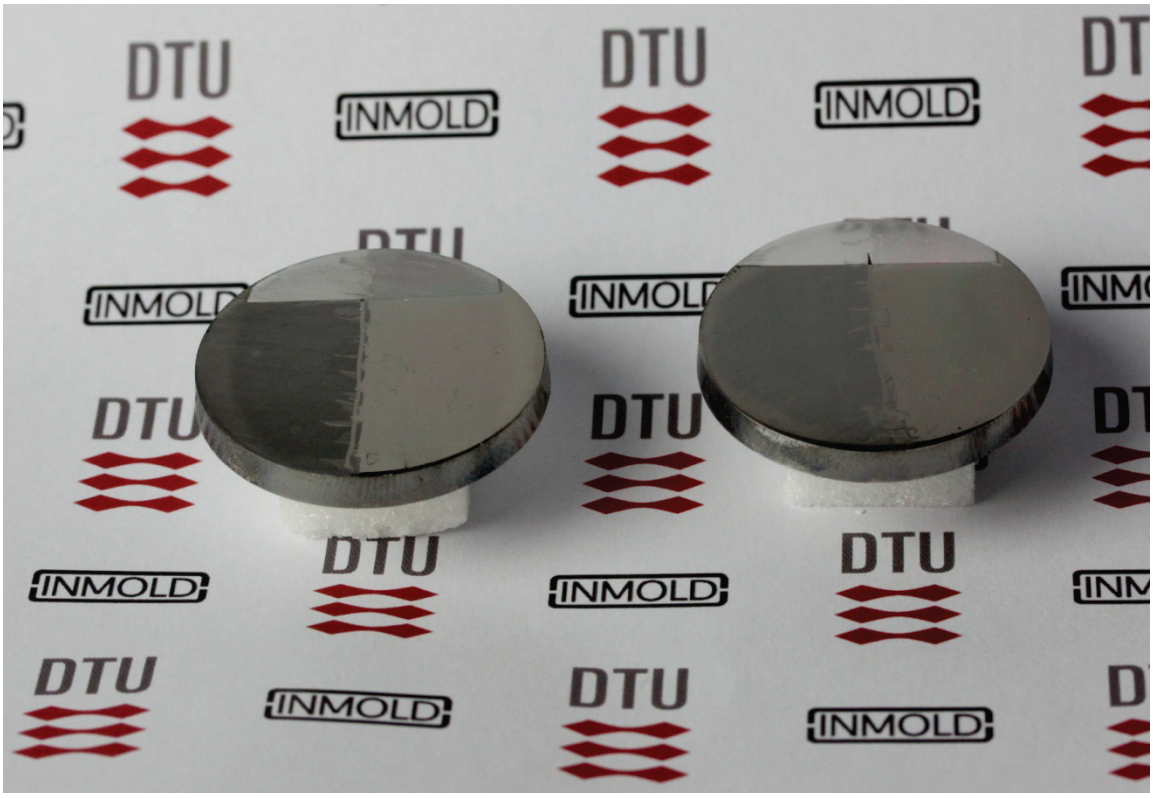

***Figure 1**. Photograph of two aluminium samples. The diameter of disks is approximately 33 mm. The left sample was polished with P2500 sandpaper, and the right one with a polishing paste corresponding to grit 11000. Vertical divide on each sample is the border between the left side, which was masked, and the right part which was coated with silsesquioxane, thus having substantially lower roughness. Horizontal line at the top section of each of shown samples marks an area that was protected by a silicon wafer during deposition of a reflective metallic film.*

The left sample is rougher as it was wet polished with superfine P2500 sandpaper, while the right sample was polished with a polishing paste corresponding to grit 11000. We can see a vertical line on each sample, dividing it into two parts. The left part was masked and is thus uncoated, in the original state, and the right part, which was coated with HSQ, has substantially lower roughness.

Films, spray-coated under the described conditions consists of almost solvent-free particles of un-cross-linked HSQ. Such films do not reduce roughness per se; they have to be re-saturated with solvent prior to full cross-linking. However during re-saturation with solvent, the surface energy of the soft, plastic, solvent re-soaked film is minimized by self-smoothing. A soft HSQ film reflows to achieve the minimal surface area. This state and shape is then fixed by re-evaporation of solvent, which makes the HSQ films harder, yet still capable of a plastic deformation. This is especially true when the HSQ film is exposed to external forces, such as nanopatterning by imprinting [73]. However, if we cure a smooth, solvent free film at an elevated temperature, it fully cross-links and forms a hard coating with a substantially reduced roughness, compared to the starting roughness of the metal substrate. This is demonstrated in Figure 2. The fully cross-linked HSQ film on the metal substrate is capable of and has been tested to withstand more than 10.000 injection molding cycles, when applied on the metal mold insert. We have been also able to demonstrate use of HSQ resist for a mold repair and refurbishing [74].

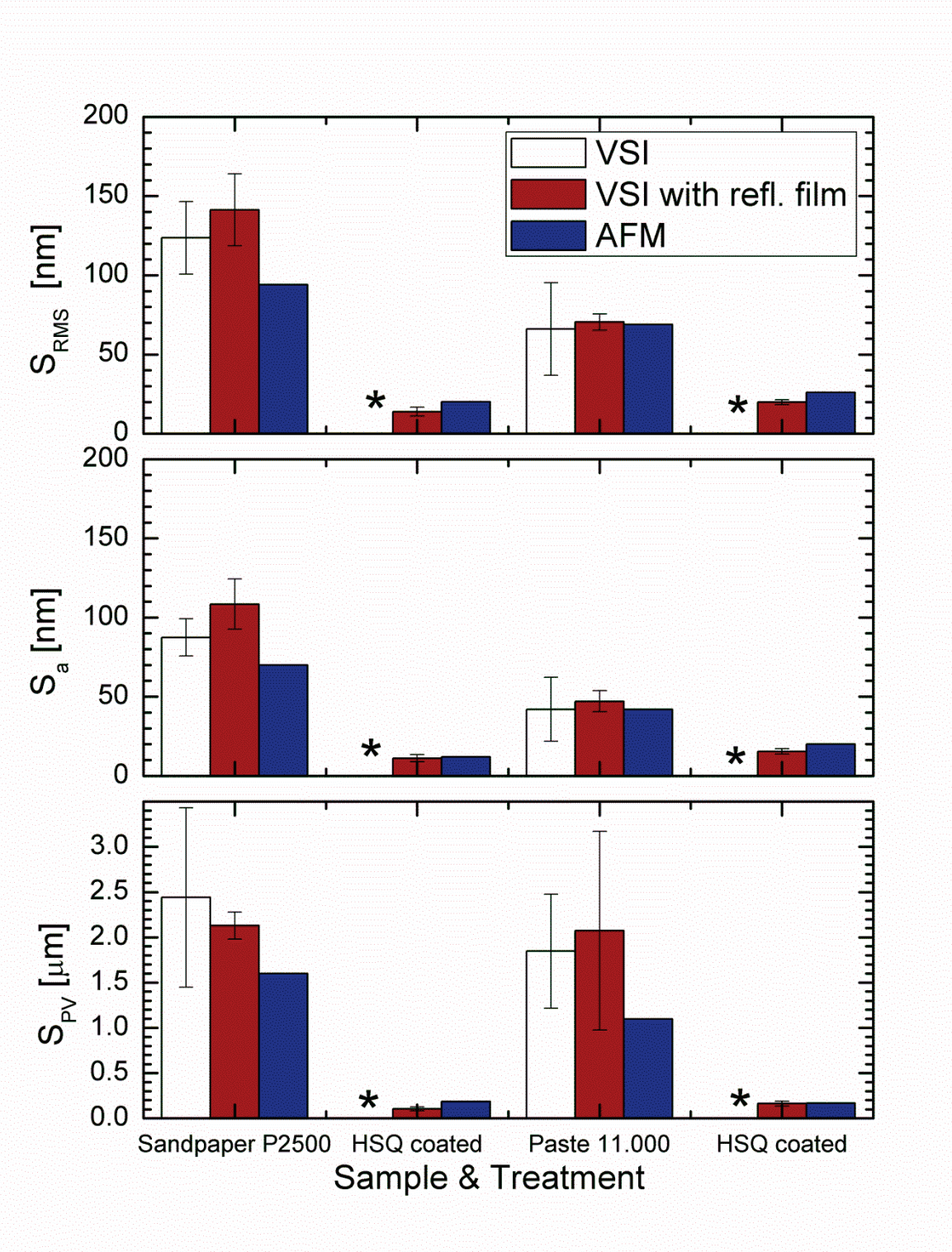

***Figure 2**. The root mean square (RMS) roughness (top panel), the roughness average (S_a), which is normally used to describe the roughness of machined surfaces (middle panel), and the peak-to-valley roughness (S_{PV}) all dramatically decrease once samples are coated with the hydrogen silsesquioxane (HSQ) film. This was observed on sandpaper and on paste polished samples and is valid for both optical (vertical scan interferometry [VSI]) and AFM data. VSI roughness data cannot be measured on HSQ coated samples without coating them with a reflective film first because HSQ coating is transparent.*

We characterized coated and uncoated surfaces with AFM and an optical profiler. An example of AFM topography is shown in Figure 3. For the 3-D optical profiler measurements on surfaces coated with the cured HSQ films it was necessary to sputter a thin layer of a reflective film in order to characterize roughness of HSQ coated surfaces. This is essential as the HSQ film alone is transparent, and has, according to the literature [75], a relatively low refractive index of about 1.36-1.39. Hence, HSQ only reflects approximately 2.4-2.7% of incident light, assuming perpendicular incidence and no roughness. This, together with an uneven, rough and highly reflective metallic substrate surface under the HSQ prevents reliable optical characterization without metallization. Neither the HSQ film thickness nor the surface topography/roughness can be reliably measured without metallization.

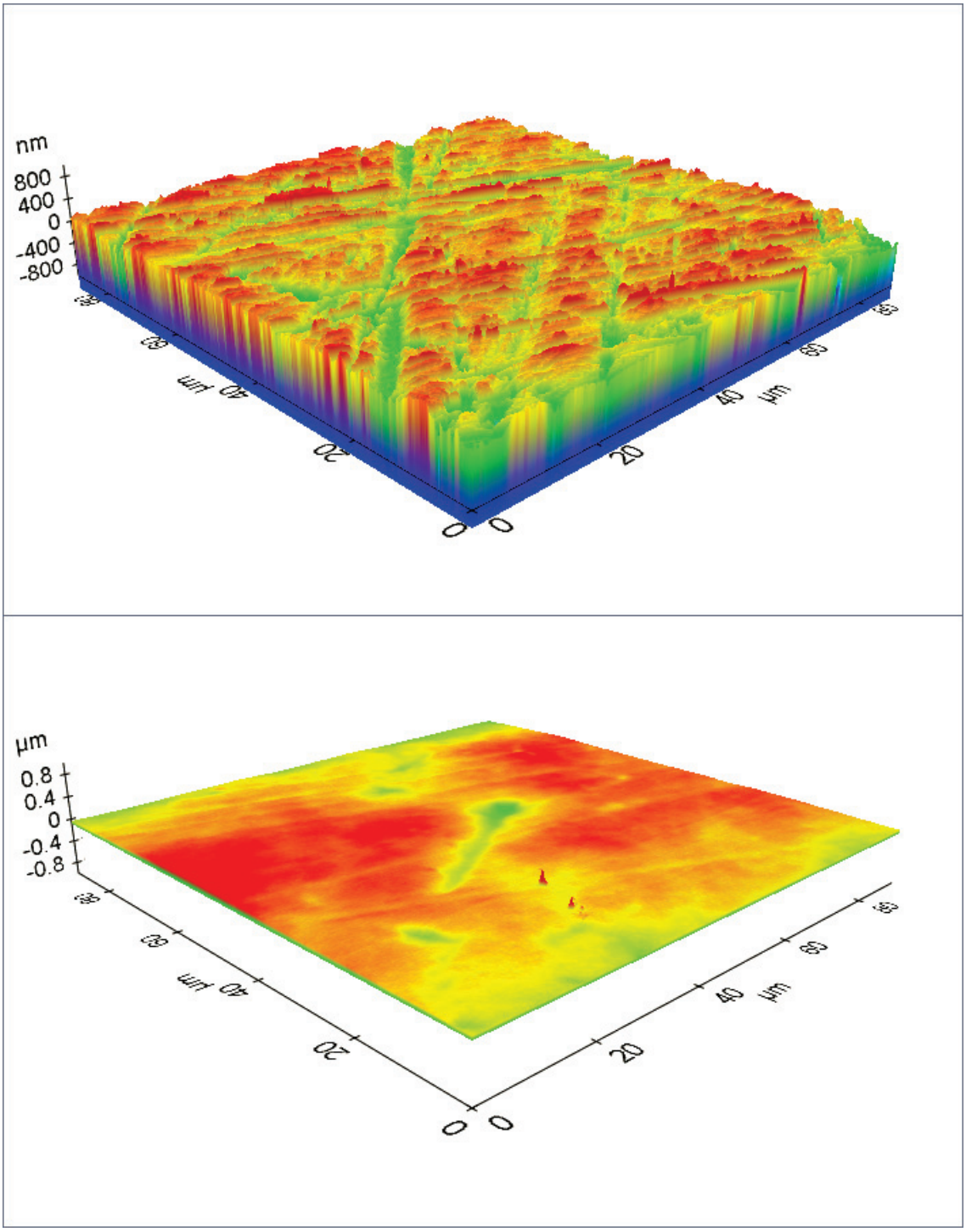

Figure 3. *Atomic force microscopy data showing the topography of superfine sandpaper polished sample surfaces. Top panel shows the uncoated surface and the bottom panel shows the silsesquioxane coated and cured surface. Surface roughness is strongly reduced.*

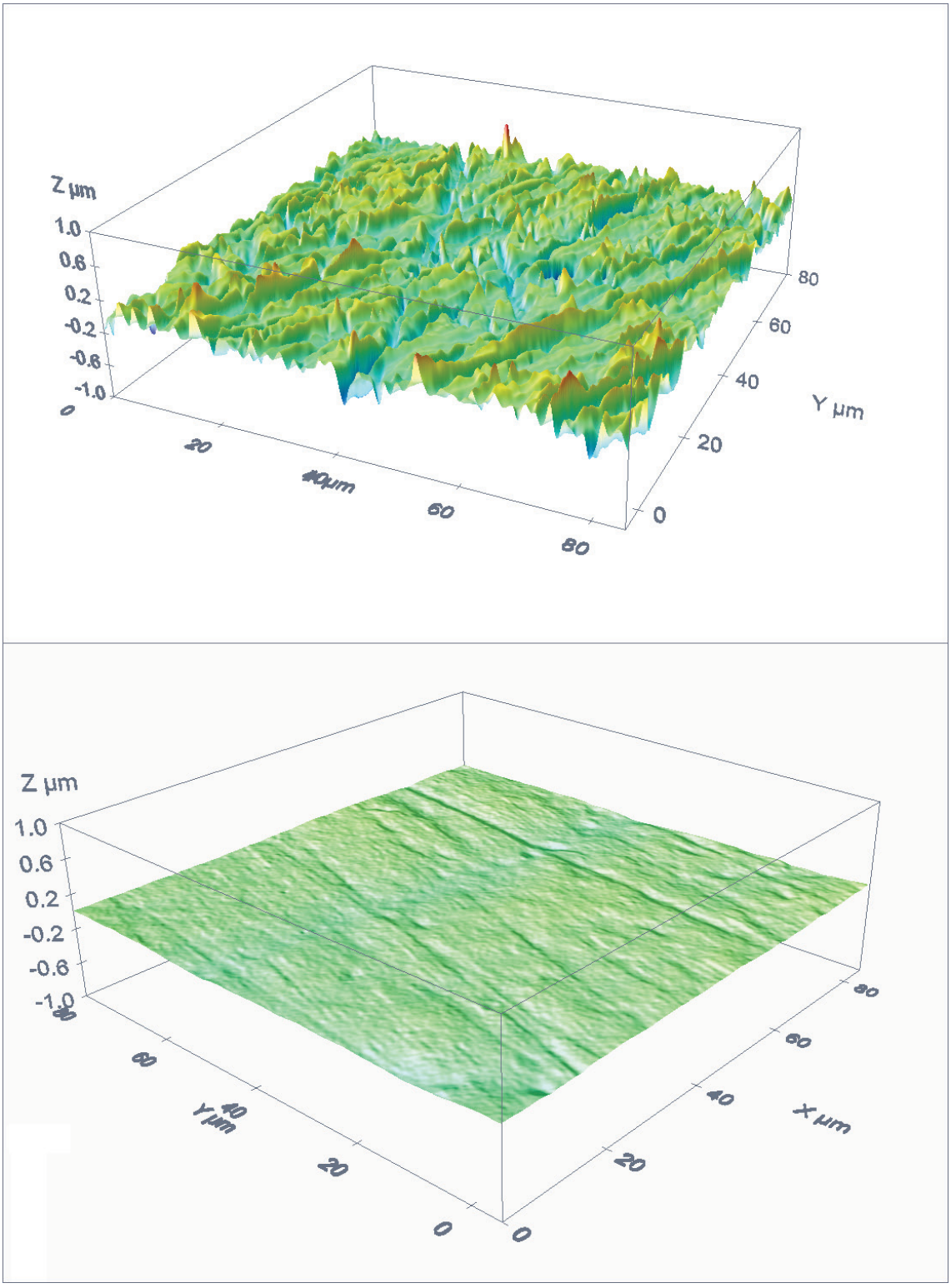

Figure 4. *Optical profiler data showing the topography of superfine sandpaper polished sample surfaces. Top panel shows the uncoated surface and the bottom panel shows the silsesquioxane coated and cured surface. Surface roughness is strongly reduced.*

However, when sputtering of a thin, reflective layer of metal on top of the HSQ, we can increase reflectance to well over 50% without altering the surface topography significantly. Using Fresnel equations and optical constants from literature [76,77] we can easily calculate that, for instance, as little as 14 nm of gold gives a perpendicular reflectance R = 0.51 for a wavelength of 500 nm, which is sufficient for characterization using an optical profiler and the vertical scan interference method. One should note that the optical constants of an extremely thin (less than 15 nm) metallic film differ slightly from the properties of the bulk metal [78,79] and that they usually form islands and voids instead of a continuous film. We can see this effect in the FIB-SEM profile micrographs, shown as Figure 5, where the non-continuous metal film is seen as the uppermost layer.

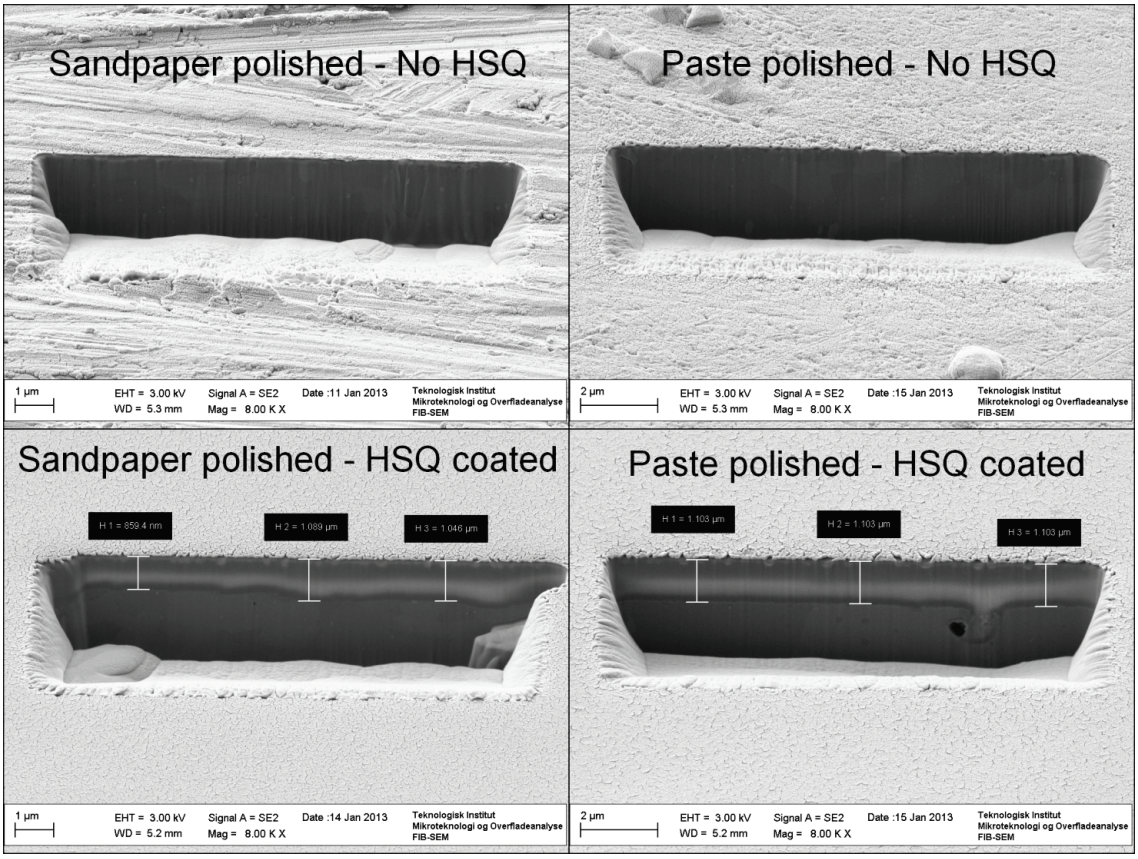

***Figure 5**. FIB-SEM micrographs showing profiles of a sandpaper polished sample (left column) and a paste polished sample (right column). Top row shows uncoated surfaces, bottom row shows surfaces with the HSQ film. Tilt angle is 54° and HSQ film thickness is approximately 1.3 µm.*

Therefore we sputtered thin reflective films not only on HSQ coated samples but also on silicon wafer samples, to verify the topography change due to the sputtering of a reflective film. We observed that a pristine silicon wafer sample shows root mean square roughness S_{RMS} of 2.4±0.3 nm while a sputter coated wafer with gold-palladium reflective film shows S_{RMS} of 1.96±0.2 nm, and the peak-to-valley roughnesses are

16±2.30 nm and 13.6±1.6 nm respectively. We can see that the topography change due to sputtering of a reflective film is indeed very small (see Supplementary Table S10 in Appendix A) thus the effect is negligible. This finally allows surface topography measurement on HSQ coated substrates using a 3-D optical profilometer, as shown in Figure 4.

Areal roughness parameters, root mean square (RMS) roughness (S_{RMS}) and the roughness average (S_a) are defined as the average of the height deviations and the mean surface (quadratic mean), and the arithmetic average (mean) of the 3-D roughness, taken over the evaluation area , therefore they are statistical parameters, and we present them in Figures 3 and 4. They are less sensitive to outliers and more independent from the choice of the evaluation area / region of interest. We see substantial decrease of roughness on the HSQ coated samples; approximately 10 times for a sample with initially higher roughness and 3 times for a sample with initially lower roughness.

For the peak-to-valley roughness (S_{PV}), defined as being the distance from the highest to the lowest point in the evaluation area, the decrease is the most dramatic one, as shown Figure 2. We see a more than 20 times lower value for the sample with a higher starting roughness and a more than 10 times lower value for the paste polished sample with a lower starting roughness. Despite the fact that the peak-to-valley roughness is the one most affected by the region-of-interest-selection, and unlike the roughness average and the root mean square roughness it is not a statistically robust parameter, it is a very a important parameter since it dominates the sample appearance, the optical properties and the perception of quality. Even samples with decent, fairly low S_a and S_{RMS} can easily be ruined by a few deep scratches, thus, the reduction of the peak-to-valley roughness is a very important effect.

We see a very good correspondence between results from two fully independent methods, AFM and 3-D optical profilometry (after deposition of a reflective film) as can be seen by comparing Figures 3 and 4. This result is in agreement with the FIB-SEM micrographs, presented in Figure 6. We can see cross-sections of a sandpaper polished surface with a visible tool marks in the left column and a paste polished surface in the right column. The bottom row shows profiles of same surfaces coated with a cured HSQ film. We can easily see an apparent film thickness and un-even morphology of an underlying metal substrate. With a known tilt angle and scale we can calculate The HSQ film thickness of approximately 1.3 µm for selected spray parameters. We can also directly see a low roughness top surface, with islands and voids of metal from a deposition of a reflective film.

Conclusion

We observed smoothing of HSQ spray-coated and solvent re-saturated films on rough and polished metallic substrates. This reduction of surface roughness was measured with two independent methods, Atomic Force Microscopy (AFM) and Vertical Scan Interference (VSI) optical profilometry and their results are in a perfect agreement. Sample cross-sections micrographs, measured with a FIB-SEM confirm the same result.

The peak-to-valley surface roughness (S_{PV}) was reduced more than 20 times for an initially rougher sample, wet polished with superfine sandpaper and more than 10 times for an initially less rough sample, polished with paste. The roughness average (S_a) and the root mean square roughness (S_{RMS}) were reduced 10 and 3 times, for the rougher and smoother substrates, respectively.

In conclusion, we have been able to show that a relatively thin HSQ film on metallic substrates such as molds for injection molding is able to greatly to decrease surface roughness. This is important, since such coating can withstand more than 10.000 molding cycles and is capable of reducing roughness on otherwise inaccessible surfaces and geometries. This result opens new possibilities for molding affordable plastic parts with perfect finish.

Acknowledgment

This work was funded and supported by the DTU Nanotech, the Danish National Advanced Technology Foundation (HTF) projects “Integrated Camera Module” (grant no. 051-2008-3) and “Advanced Technology Platform NanoPlast” (grant no. 007-2010-2) and the Copenhagen Graduate School for Nanoscience and Nanotechnology (C:O:N:T). Authors would like to thank Dr. Kathrine Bjørneboe from the Danish Technological Institute for the FIB-SEM micrographs and Dr. Eric Jensen for proofreading.

Supplementary data

Supplementary data, namely supplementary table **S10**, associated with this chapter can be found as an Apendix A of this thesis.

Chapter 6: Development of a toolbox for the extreme pressure embossing

"The true method of knowledge is experiment."
William Blake (1757– 1827)

Preliminary experiments are called preliminary for a reason, as the interpretation of an outcome, a result, positive or negative, can be tricky at best, or completely misleading at worst.

In early January 2011, more than two years ago, I was able to make *one* successful nanostructure imprint in a hydrogen silsesesquioxane (HSQ), a hard, glass-like resist. I used a mere 50 bar of pressure, still an order of magnitude more than what is used during "normal" soft lithography or thermal nanoimprint lithography processes. A commercial, of-the-shelf OBDUCAT system was used, same as in the chapter 4. I used a spin-coated HSQ layer on a flat wafer and a flat, 100 µm thick Zeonor COP polymer foil stamp with nanopattern. An encouraging result, to some extent in a disagreement with previous literature reports, but looking like I have a perfect system for nanopatterning of highly curved surfaces, including those on injection molding inserts. Way to go!

The only problem with this result was, that, as it turned out to, I was unable to imprint again for next year and half.

This chapter does not cover results of embossing into HSQ. It covers development of a toolbox, in particular nanopatterned masters and dedicated embossing devices. I discuss design, development, testing and failure analysis, as well as a few steps of redesign and retesting a dedicated embossing system, capable of delivering hydrostatic pressure in excess of 1000 bar. A rather unusual nanoimprinting device. For an illustration, a peak combustion pressure in a Renault gasoline spark-ignition engine is about 50 bar [80]. A peak combustion pressure in a diesel engine cylinder of personal car is 160[81] to 180 bar [82], and values around 200 bar are reported [81,83] for a heavy duty commercial truck engines. Pressure at the bottom of the Mariana trench, the deepest part of the world's oceans, 10 911±40 m below the mean sea level is 1086 bar, comparable to the 1100 bar inside a rifle barrel, when a 5.56 mm NATO round leaves the muzzle[84]. As I learned the hard way, many materials behave very different at such conditions, for instance, density of water, in first approximation

considered incompressible, is increased by as much as 4.96% at the bottom of the Mariana trench.

Materials and methods

This section covers details of a process to form large area nanopatterned stamps using interference lithography and description of few developed embossing devices. Development of nanopatterned tool was carried out at DTU Danchip and DTU Fotonik at RISØ. Development of embossing devices was done using workshops of DTU Mechanical Engineering and DTU Danchip, and labs at DTU Nanotech. The designed process flow is shown as the Figure 1.

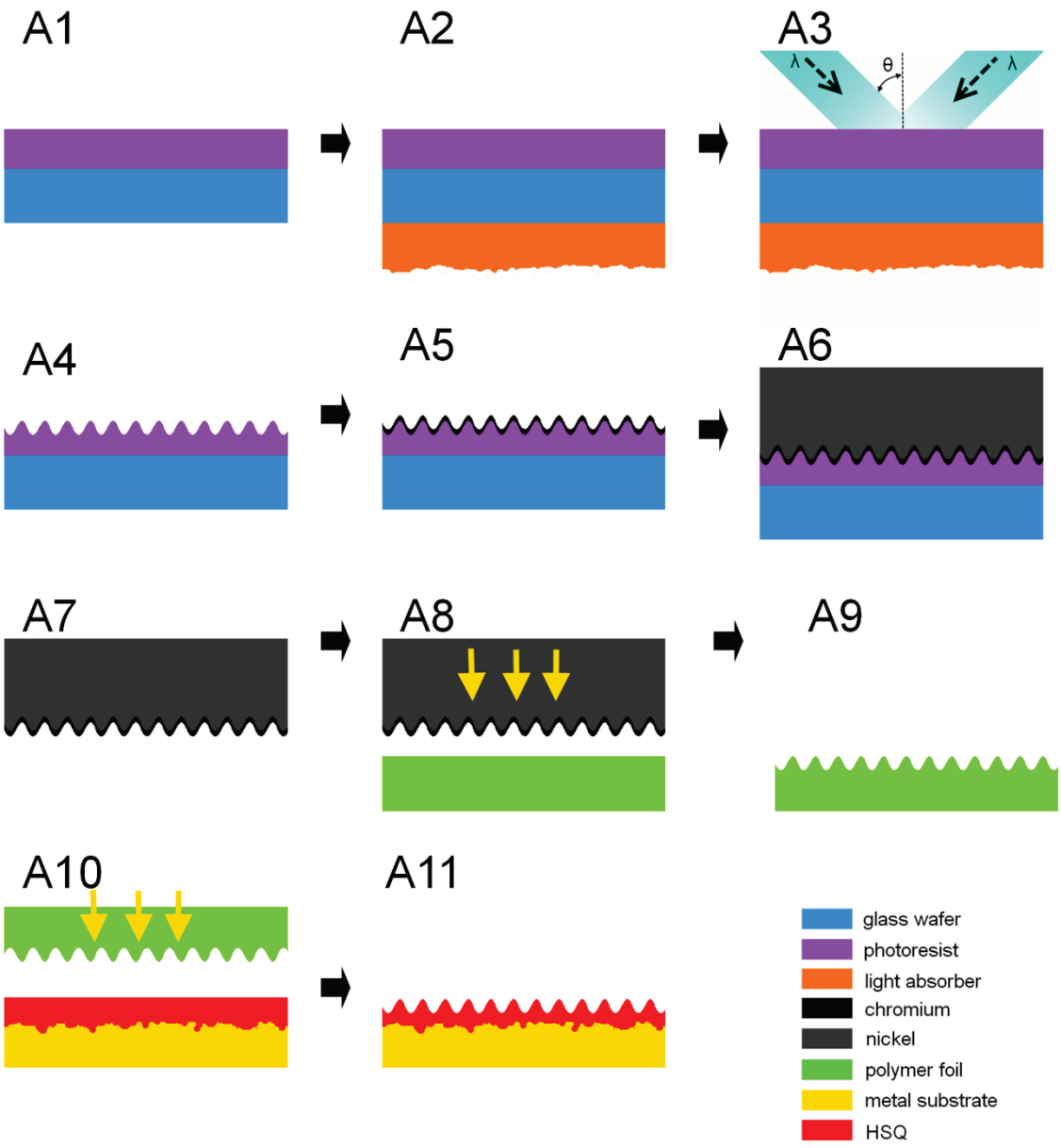

Figure 1. *The process flow, where a polymer foil stamp is used to emboss into HSQ film. A1: glass wafer is spin-coated with 1.5 µm of AZ5214E resist. A2: backside absorber is deposited. A3: Interference lithography exposure(s), a fringe pattern recorded. A4: resist development, a corrugated, phase grating formed. A5: Chromium seed layer (60 nm) evaporated. A6: Nickel electroplating, 25-350 µm. A7. Separation, cleaning and FDTS coating of Ni foil. A8. A Zeonor polymer foil is thermally imprinted with Ni foil. A9: Separation of foil. A10: Foil used as a stamp to emboss into HSQ. A11: Nanopattern replicated in an HSQ, ready to be cured and used as a mold.*

Method to make imprinting tool with nanopattern

The selected nanopattern is a cross-grating (two superposed gratings rotated by 90 degrees) formed by the light interference. This allows us to reach a period below the wavelength of used light and this method is known to be extremely precise. Since the

period in both gratings is identical for all practical purposes, one can use such a pattern as a metrological device to characterize deformation and to calibrate and evaluate other machines and methods.

I used a 100 mm boron glass wafers, double side polished, thickness 500±10 µm. The wafer carrier was open inside the cleanroom and wafer surfaces have not been cleaned as I observed that it would contaminate them more than if they were left alone.

The chemical treatment priming with Hexamethyldisilazane (HMDS) prior to the spin coating was used to promote the adhesion of the applied photoresist. A Star2000 system from IMTEC was used to do vapor deposition of HMDS under the low pressure and high chamber temperature. The cycle consists of dehydration and purging with nitrogen for 12 min., priming with HMDS vapor for 7 min. at 150 °C, purging and exhaust for 5 min., venting with return to atmospheric pressure for 3 minutes. Full process takes cca 27 minutes. Primed glass wafers have been placed outside HMDS oven at ambient cleanroom atmosphere for approximately 15 minutes, to cool down.

Immediately after cooling down to room temperature, the wafers were been spin-coated. A Maximus 804, SSE (Sister Semiconductor Equipment) automatic spinner was used. I selected AZ5214E resist, to allow further processing at DTU Danchip, and the recipe was a standard one, named “1,5 4inch”. This recipe is designed to form 1.5 µm thick photoresist on a 4 inch substrate, and perform a soft-bake on the internal hotplate at 90° for 90 s. At the end of this process, substrates with resist are ready for exposure.

After depositing resist layers on glass wafers, I closed them in opaque wafer carrier and transported them to the DTU Fotonik at RISØ where first, the polymer absorber was deposited (poured) on the backside and left overnight for full curing. Second, another day, interference lithography exposures were carried out.

A schematic chart of the interference lithography setup is shown in figure 2. A He-Cd metal vapor laser operating at 441.56 nm in continuous wave mode was used. Setup is placed on a vibration isolated optical table, with a massive PMMA box enclosing the whole table to limit the influence of an air flow. The main parameter varied is the exposure time, which is discussed later. Tested exposure times range from 2 to 480 s. The exposed area is not the full wafer but roughly circular with a diameter of 60-70 mm. Setup is operated remotely, by an electronic shutter with delay, to limit even the slightest vibration sources. The Sample (wafer with resist and backside absorber) is placed on a rotational stage, so one can easily perform 2 subsequent exposures with a rotation by exactly 90°.

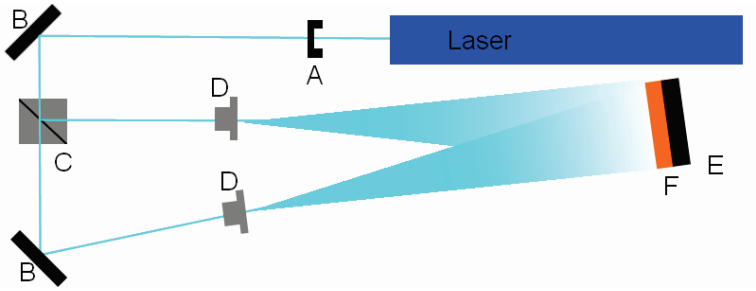

***Figure 2**. Schema of an interference lithography setup. A: Electronic shutter. B: Dielectric mirrors. C: Beamsplitter. D: Spatial filters. E: Sample stage F: Sample.*

After exposing the resist layer on a glass wafers, I peeled off an elastic backside absorber, packed them again in an opaque wafer carrier and transported back to DTU Danchip. There, the exposed wafers were developed using the developer-2 bath consisting of AZ351 developer and water (1:5) mixture at 22±1 °C. I processed 1 to 6 wafers at a time and made fresh developer prior to every use. The development time suggested by Danchip for 1.5 µm AZ5214 resist is 60 s. I found it completely inadequate for my laser exposed samples and I tested times from 50 s up to 4 minutes, as discussed later. Wafers were rinsed in DI water and spin-dried.

The next step is the deposition of a conductive seed layer; I again used the Wordentec QCL 800 system to deposit 60 nm of chromium via e-beam deposition. This technique is reliable and uncomplicated, as it is easy to achieve conformal coverage on a relatively shallow sinusoidal cross-grating.

Electroplating of the cross-grating created in resist, with the chromium seed layer on top, was carried out using Technotrans microform.200. This system is dedicated to electrochemical deposition of nickel. The thickness of the deposited Ni layer depends on total passed charge, and foils with thicknesses from 25 to 350 µm were prepared. At the end of process, the obtained stack with say 300 µm Ni foil on one side, seed layer and resist layer in center and the glass wafer on the other side is removed from electroplater. The resist layer self-separates from the used glass wafer and stays on the Ni film, which then may be transferred outside the cleanroom, and carefully rinsed with a few batches of acetone, IPA and ethanol and blow dried.

Prior to preparing polymer or HSQ replicas, the nanopatterned nickel foil is FDTS coated using MVD system and 4 cycle process STAMP, well described in previous chapters.

Pattern transfer to a flexible polymer foil is carried out using a commercial device CNI (Compact NanoImpriter) from NIL Technology. This system is a typical thermal nanoimprinter, but miniaturized and with fairly fast operation. I used a stack consisting of a solid wafer-sized ceramic stamp, 100 µm PTFE copolymer foil, a dummy Si wafer coated with FDTS coating, polymer foil sample (Zeonor COP), Ni stamp (tool) with

previously created nanostructures, 500 µm PTFE foil, and inflatable silicon cushion in the lid, to deliver pressure.

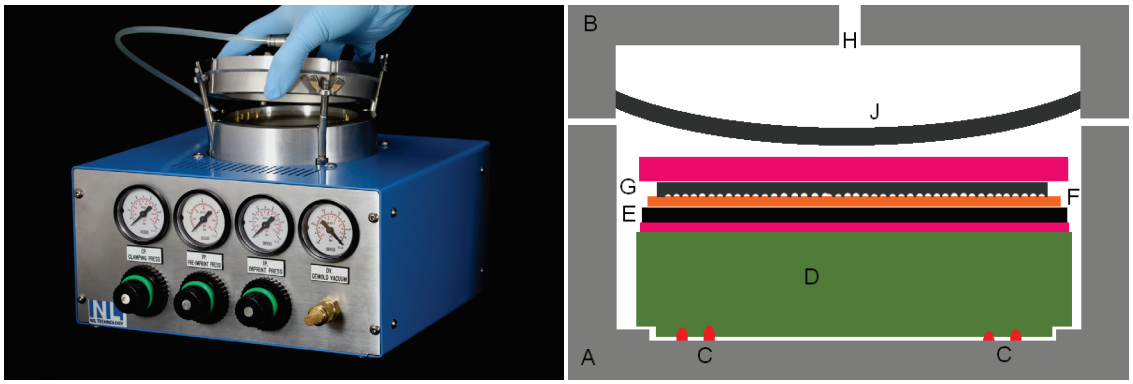

***Figure 3**. The Compact NanoImprinter from NIL Technology, Left: Photo. Right: Principle of operation. The bottom part A is closed with lid B, and current is passed between pins C, rapidly heating solid stamp D. A dummy FDTS coated wafer E ensures a clean and flat backside as the actual polymer foil F is imprinted by the nanopatterned stamp G (nickel foil). The stack begins and ends with soft, PFTE copolymer foil. Imprint force is delivered once an inert gas is pumped via opening H to a cavity above the soft, inflatable cushion J.*

Used polymer foils are ZEONOR COP, thickness 188 µm, grade ZF14-188, lot no: 201055-20100224, thickness 100 µm, grade ZF14-100, lot no: 20090318-2009-12-18-02 and thickness 50 µm, grade ZF-14-050, lot no: T26X097.

Stamp process development

The first task in development of the system to transfer nanopatterns to highly curved surfaces is, unavoidably, creation of the nanopattern in question. As the goal is not only to create nanopatterned surface suitable for use as an injection molding mold, but also to characterize stretching and conforming of planar stamp to non-planar substrate, one needs a perfectly precise stamp with highly homogeneous period. Fortunately, there is great answer for this demand.

Interference lithography

Interference lithography technique where the period is given only by the wavelength of the used laser and the angle of interfering beams, is a suitable solution. One can rely on the interference of two laser beams 1 and 2. If the phase relation is constant (beams are within their coherence length) and the wave front is not distorted, structure of well defined lines is obtained. This pattern is usually referred to as a diffraction- or Bragg-grating, and their period Λ, which depends only on the angle(s) and wavelength can be calculated using

$$\Lambda = \frac{\lambda}{\sin\theta_1 + \sin\theta_2} \quad (1)$$

Where λ is the laser radiation wavelength and θ_1 and θ_2 are the angles between normal of the exposed surface and normal of the wavefront of the beam 1 and 2 as shown in figure 4 left. The intensity of the pattern is sinusoidal and this can be used to expose pattern in photoresist. Such a recorded pattern is then a grating by itself, first, an amplitude grating, as the resist is photo-darkened or photo-bleached, then, after development, when the exposed or the unexposed part is removed, one obtains a regular phase grating (with corrugated surface).

If divergent and not collimated (parallel) beams are used, the period error (or variation) is

$$Error = 100 \times \left(1 - \frac{1}{\cos\left(\frac{\beta}{2}\right)}\right)\% \quad (2)$$

where β is the angle between the two most distant points of an exposed substrate and the point source of the exposing beam. However, this error can be easily reduced if one uses a collimating lens after the spatial filters. With a properly designed setup, the period error can easily be well below 0.05%. Spatial filters (figure 4 right) can be used to select part of the Gaussian power distribution across the beam, as they consist of an objective and a pinhole. The incoming beam is focused to the pinhole and only a part of the beam which gets through is used.

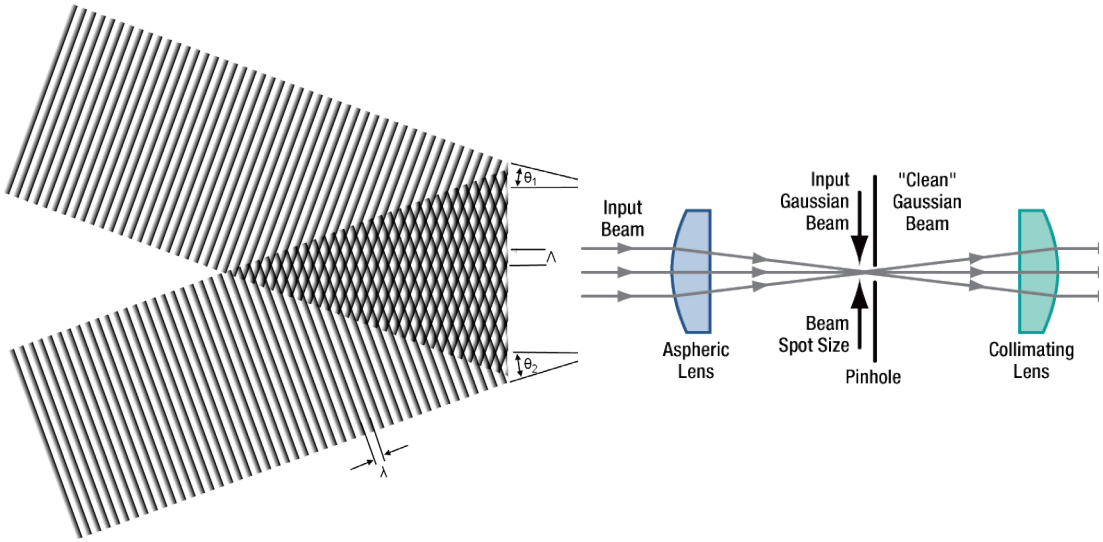

***Figure 4**. Left: Wavefront interference. Right: spatial filter, taken from* [85].

There is an obvious tradeoff; if the focus is imperfect, only a small part of the beam will be used after pinhole, and the total intensity will be strongly reduced, but the resulting intensity profile will be very flat and uniform. This means that the photoresist will receive almost the same (low) dose in the center and on the periphery of the exposed area. If, on the contrary, the beam is focused almost perfectly (or the pinhole is bigger than needed), practically all light from the laser will get through, and intensity behind will be higher but less even. Low intensity can be compensated by a longer exposure, to assure the same dose. But long exposure will be inherently much more prone to vibrations and path variations. This is reason why I used a setup on the vibration isolated optical table with massive PMMA box, which not only provides safety, but more importantly, restricts air flow over setup, which is another potential source of error due to path variations.

Reflections

The exposing beams do not stop after they reach substrate with photoresist. There is a slight absorption, which is in fact inducing changes in the resist, making it work, but since the photoresist film is only 1.5 µm thick and the absorption coefficient α is only 0.04 - 0.08 μm^{-1} for the unexposed AZ5214E photoresist at 440 nm, one can calculate, using

$$I_{after} = I_0 \exp(-\alpha \, d_{resist}) \quad (3)$$

Where I_0 is the initial intensity and d_{resist} is resist thickness, that 88.6 to 94.1% or the light is still there after the first pass of photoresist layer. AZ5214E resist is primarily developed for i-line and h-line (365 and 405 nm), which explains low absorption. This clearly explains why I used glass wafer. If silicon wafer is used, one can calculate that with the real part of the refractive index of Si at 440 nm being n = 4.79 [76], and the refractive index of our resist at 1.664 (the mean mean value for exposed and unexposed resist from [86]), reflection back into resist, according to Fresnel's law,

$$r = \left(\frac{n_1 - n_2}{n_1 + n_2}\right)^2 \tag{4}$$

will be enormous, almost 25% for normal incidence, ruining the exposed pattern. However, for a borofloat glass wafer with n = 1.48 [87], the reflected intensity is well below 0.5%. This shows why glass is a much better choice. Unfortunately, light will not stop in glass, but reaches the backside of a glass wafer. There, according to the same equation (4) as before, using n=1 for air, portion of light (4%) will be reflected back. This would be again able to seriously degrade the created pattern, so a countermeasure is used. Backside of the glass wafer is coated with almost 1 mm thick film of polymer with an orange-red dye and the refractive index of this layer is again matched to be very close to the one of glass and the resist, so reflection on the interface is neglible, but the dye is strongly absorbing and almost no light is left after this backside absorber.

Exposure and development

With all this considered, one can start testing the first 7 steps (A1 to A7) of the process depicted in Figure 1. One of unknown parameters is the exposure time, as the sensitivity of the used resist to monochromatic laser light is not known. The first estimate is the time used for the same thickness in a conventional mask aligner. This is, according to DTU Danchip, 5-7 s. However, the mask aligner uses mercury lamp and the intensity seems to be much higher. I attempted to estimate the dose and compare it with the intensity and the dose from laser, but since the intensity at the substrate plane of interference setup is not known, one cannot use this way to predict optimal dose. I decided to run a preliminary test across 2 orders of magnitude, from 2 to 480 seconds, for a single exposure, no cross-grating attempted. Only the exposures at 64, 128, 256 s yielded structures with visible diffraction. This allowed for the initial exposure dose estimate to be made. The experiment was, as a set II, repeated after few weeks, this time with a cross-grating and 2 half-time exposures. Results of this and other sets (III, IV and V) are shown as figure 4. One can see that the optimal exposure half-time, if the maximum depth is to be optimized, lies likely between 90 and 180 seconds. Exposures at 160 seconds have been used most, and are shown as bottom panel of the same figure 5.

The observed effect of the development time does not appear to be significant, and does not appear to be very systematic within the “proper” range, which is was found to be 3 to 4 minutes, again much different than 50-60 s, suggested in the recipe for optical lithography at Danchip. Developed wafers are then rinsed, spin-dried, chromium seed layer is deposited and used to electroplate nickel of selected thickness.

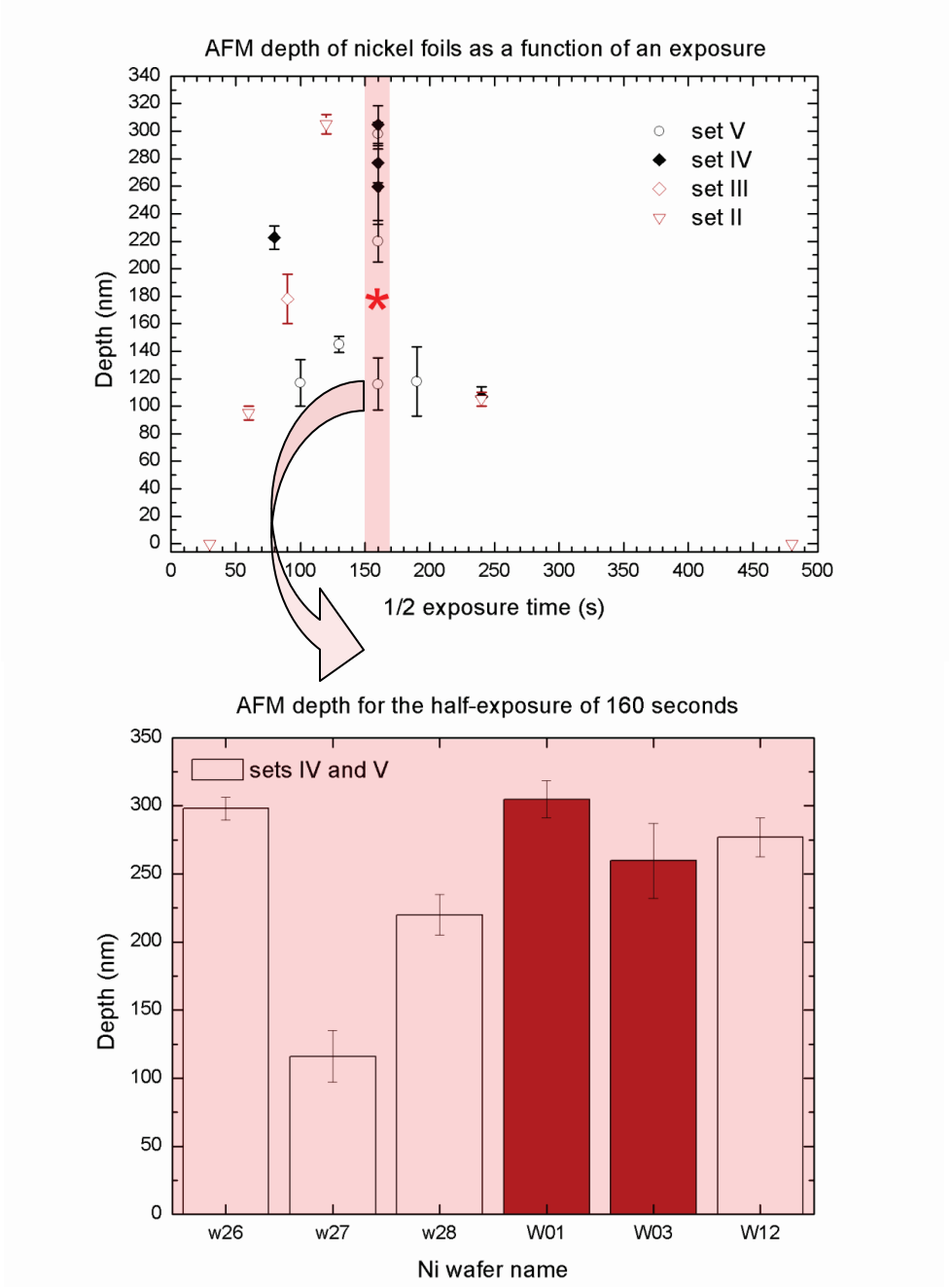

Figure 5. *Top panel: Depth of nickel foils as a function of an exposure time, as measured by an AFM, shows that the optimal cross-grating half exposure time for a selected photoresist and thickness is between 120 and 160 seconds. Red star and red background indicate exposures for 160 seconds, which are shown separately in the bottom panel for better visibility. Bottom panel: Overview of all half-exposures at 160 seconds, plotted separately. Red filled columns indicate 240 second development time, white filled are developed for 180 seconds. Wafers w26,w27,w28 are from set V, W01,W03 and W12 from set IV.*

Characterization of nickel tools

The prepared nickel tools have been characterized with usual methods, namely SEM and AFM. The AFM system used in this step is a metrology system at DFM, calibrated with a traceable standard. The estimated mean period is 426.2±0.5 nm. The highest observed period difference for both gratings across whole wafer is below 0.2%. The highest period difference in same spot is 0.04% or less. Results are presented in figure 6.

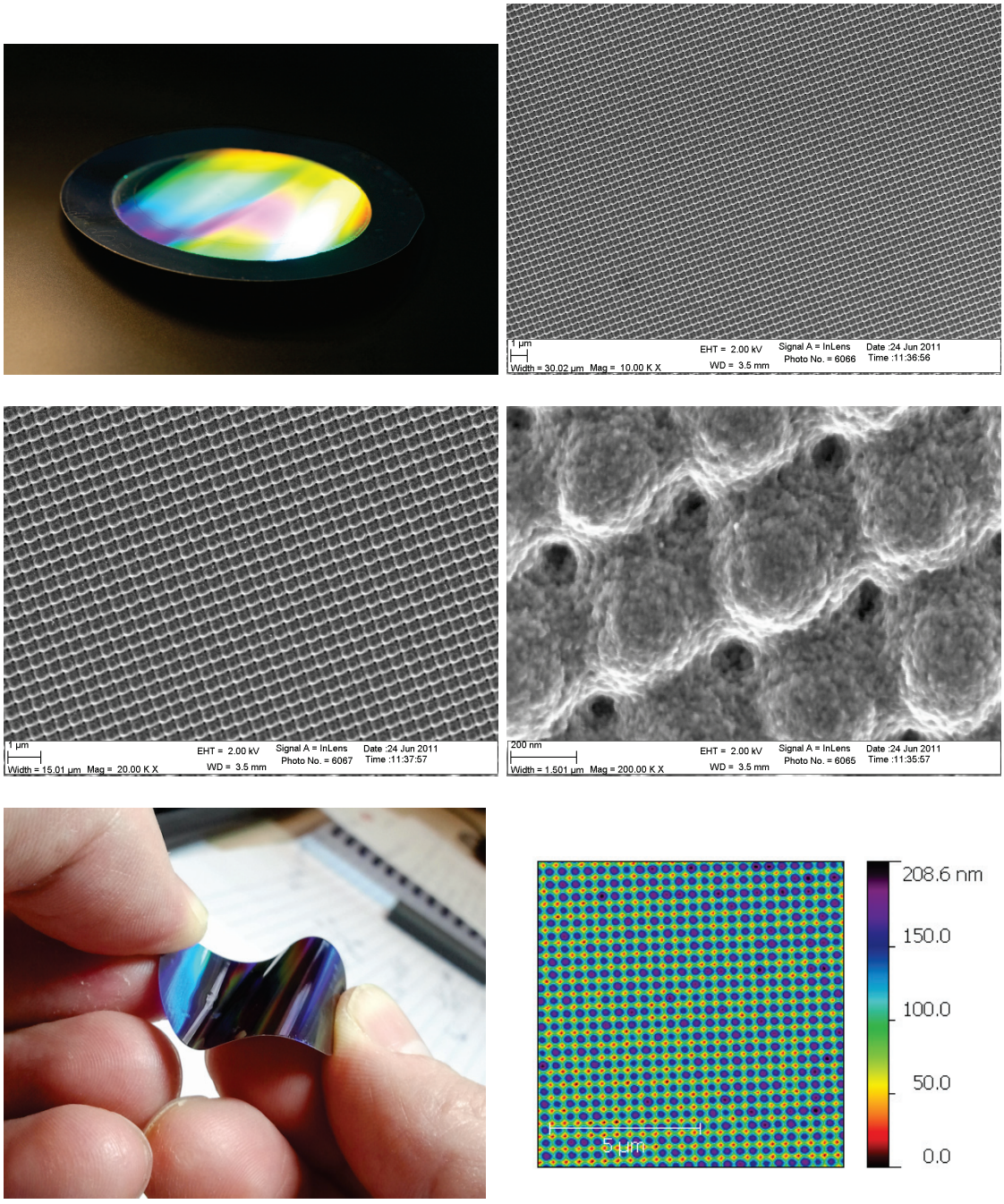

Figure 6. *Prepared Ni tools with cross-grating nanopattern.*

Alternative use

The resulting nanopatterned nickel foils can be useful by *per se*. Thick foils (approximately 300 μm) can be cut with a special tool to form 85 mm disk, which can be directly used as a mold insert for injection molding. This can be used as a viable method to produce affordable nanostructured polymer samples using injection molding. Moreover, if one uses a macroscopic shadow mask, laser-cut from black paper sheet, to restrict the exposed area, the nanostructured area is restricted as well. This can be seen on the Ni shim shown in the top panel of Figure 7. If this shim is used as a mold insert, small, microscope slide-sized plastic parts can be produced. They have part of the surface nanopatterned and are thus diffractive, as demonstrated in the bottom panel of the figure 7.

Figure 7. *Photo of a Ni tool with nanopattern only on the area not shielded by a laser cut shadow mask (top) and photo of injection molded polymer microscope slides, created using the same tool, showing logo of The Danish National Advanced Technology Foundation (bottom).*

Common defects

The most common defects observed on nickel foils with large area nanopatterns created by interference lithography are depicted in Figure 8. None of the observed defects affect the period of the nanopattern. One can see large, centimeter wide circular waves, which are barely visible, and do not affect depth too much. They likely come from the Gaussian-like intensity profile of beams. Second, a strange, triangular pattern of faint, few millimeters wide spots was observable on some samples. I was able to trace it down to the manipulation rods of an automatic spin coater. The photoresist on the wafer above the holes for manipulation rods is somehow modified. It may be due to different heat capacity and heat flux during resist evaporation or due to local, vacuum induced bow of unsupported wafer. Again, the pattern depth is not affected much. Third, in the last 2 sets of samples, small white spots can be observed. They can be traced to the air bubbles in the polymer mixture used for the backside absorber. The nanopattern depth is locally reduced.

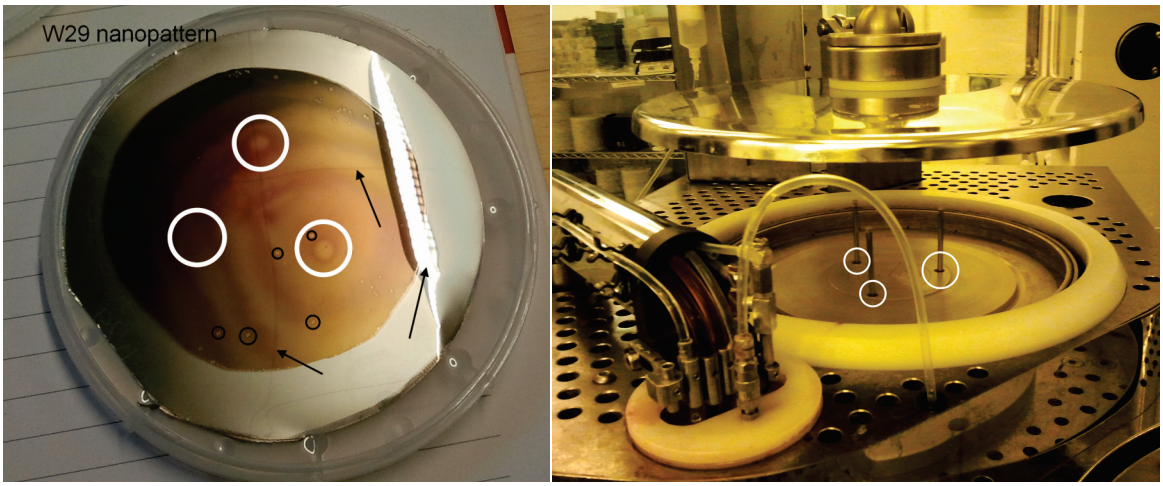

***Figure 8**. Common defects on nanopatterned nickel foil. Left: Photo of wafer with cross-grating pattern. Note the three types of defects; first, small pinhole-like spots, marked by black circles, can be traced to voids in the backside absorber. Second, 3 larger spots in a triangle pattern, marked by white circles, can be traced to manipulation posts in the Maximus automatic spinner (right panel). Large, centimeter sized, circular waves, are projection of a non-perfect Gaussian beam profile. Finally, light and dark lines, marked by arrows, are not defects; they are reflections of a ceiling structure and lamp at the lab.*

Replication of nanopattern to Zeonor foils

After the prepration of the Ni master, one can proceed to steps A8 to A9 of the Figure 1 with the general process description. I was able to use the Compact NanoImprinter (CNI), to replicate one of the best Ni master onto numerous Zeonor foils, with thicknesses 50,100, and 188 µm. Foils are flexible and transparent; areas with the

cross-grating are slightly diffractive since they act as a phase grating. Replication was carried out at 165 °C, well above the glass transition temperature of Zeonor COP (136°C) and cushion pressure was 6.5 to 7 bar. The operation principle of device is shown in Figure 3, and actual results are shown in Figure 9, together with the foils. An interesting observation is a high degree of electrostatic charging once the foils are separated from the Ni and the dummy wafer. It might be probably reduced by quick dip in DI water in the cleanroom, immediately after imprinting, as the dust-collecting effect of foils is a nuisance in further steps.

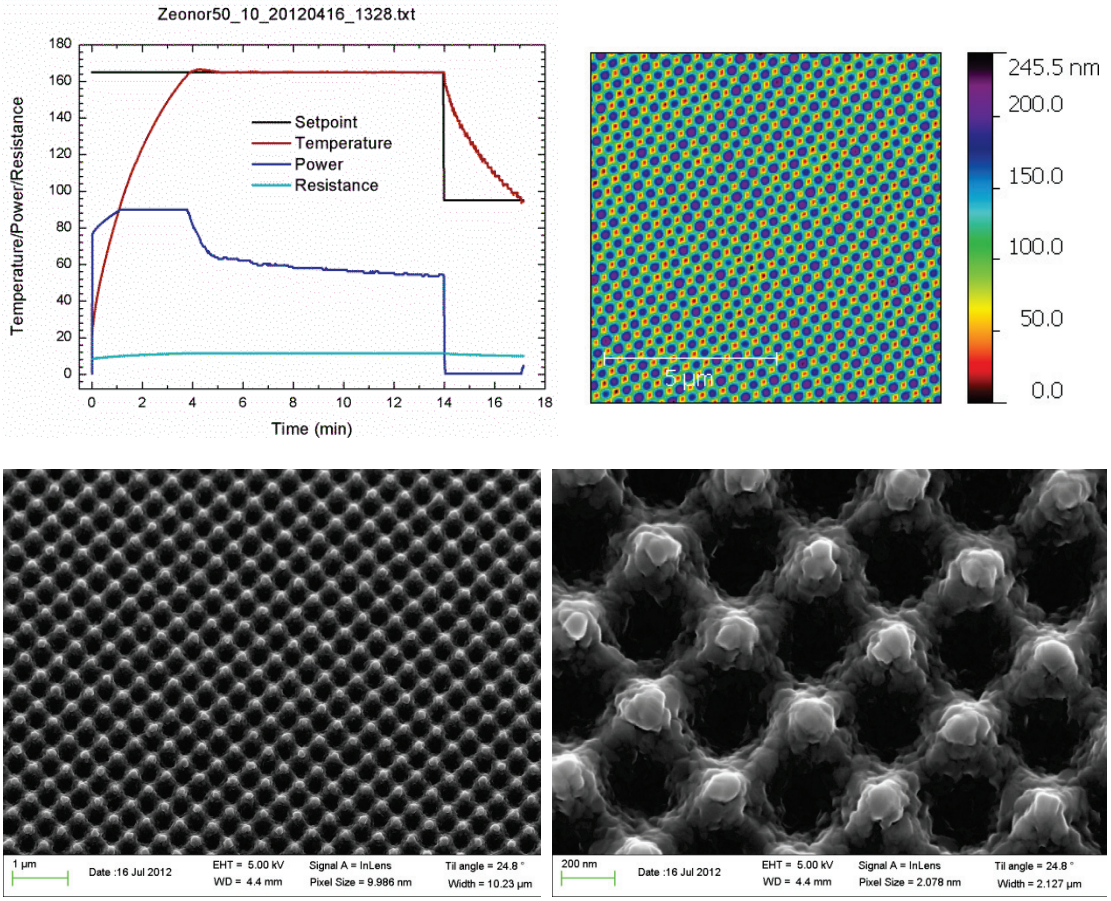

Figure 9. *A typical operation cycle of the Compact NanoImprinter (top left). Note a relatively short cycle time, even prior to any optimalization. AFM and SEM micrographs of Zeonor foil with nanostructures. Both depth and period appears identical to the Ni master used.*

Embossing tool development

The initial tests with embossing have been done in the commercial Compact NanoImprinter device, already described and shown in Figure 3. It can be referred to as device 0. The maximum pressure, **6.5 – 7 bar**, is limited not only by its delicate construction but also by the external supply in the cleanroom. With the pressure this low, there was no imprint or even a roughness change of an HSQ film.

A more robust device, commercial Obducat NIL 2.5 is well described in previous chapter. It can be referred to as device 1. It uses gas pressure in the chamber, separated by a thin, deformable aluminium foil from the imprinted stack. Maximum pressure, if there are leaks in system, is claimed to be 70 bars, but during numerous trials I found it practically impossible to reach more than **65-67 bar**. Imprinting, with one notable exception, mentioned at the beginning of this chapter, was not observed as the pressure is not sufficient.

The next step was design and fabrication of a dedicated high pressure device. I aimed for simplicity, and proposed the device depicted on figure 10, which will be referred to as the **Embossinator 2**.

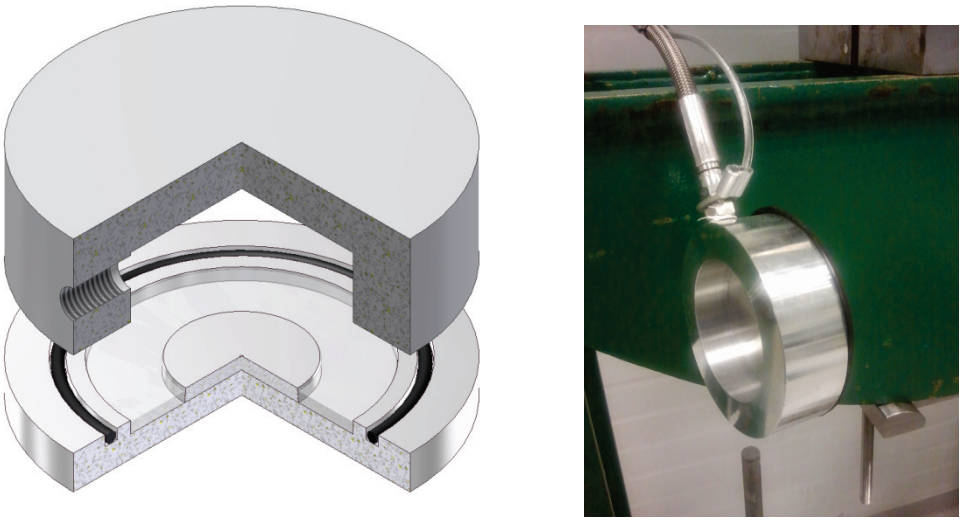

***Figure 10**. Embossinator 2, a dedicated high pressure embossing device.*

The high pressure source is an external gas cylinder with compressed argon or nitrogen, which is then introduced to the system either directly or *via* a high pressure reduction valve. This pressure is then used as a hydrostatic pressure at the top side of a nanopatterned polymer stamp. The full stamp is slightly bigger than the o-ring in the base (bottom part), and is therefore clamped between the base and the lid (top part) when system is closed. HSQ coated substrate; either aluminum disk or 50 mm wafer, is placed on top of a laser-cut PMMA spacer. Whole system is clamped tight in a massive hydraulic press. Theoretical pressure limit is 200 to 230 bar as found in a full gas

cylinder. I designed the wall thickness according to the thickness of an aluminum scuba cylinder wall (11.8-15.5 mm [88]), which is rated for 200 and 300 bar. After reading about few catastrophic failures [89,90] of the aluminum scuba tanks, I added 50% reserve.

The device is made out of 6061 aluminum. This is the first system where I was able to regularly obtain imprint in an HSQ film, but the imprint depth was extremely low, typically below 10 nm. There are a few important observations; first, clamping force of a hydraulic press must be well above 5 tons, if not, force on the base (with projected inner cavity diameter of 66 mm) at 150 bar is 5.4 tons, thus exceeds the clamping force of press. This leads to opening of the system and explosive decompression. Another effect is an extrusion of the o-ring, which is then projected across the lab. Consequently, I used a full face motorcycle helmet when I operated this device. Second, if a direct connection with no reduction and bleed valve is used, pressure limit is identical to pressure in the used cylinder; say 180 bar, which is good. However, a controlled venting of the system at the end of process is then almost impossible. If a high pressure reduction valve is used, pressure losses occur and I was unable to reach pressure over **150 bar**. Overall, despite its simplicity, this device is useful, but certainly not suited for production environment.

Another dedicated designed and fabricated very high pressure embossing device is the **Embossinator 3**, system shown in the figure 11. I dropped the concept of gas pressure and moved to the use of a fluid as hydrostatic pressure delivery medium. Water or hydraulic oil does not seem to be suitable fluids, as they would unavoidably contaminate substrate and stamp and HSQ is extremely sensitive to humidity. I selected PDMS, the material used as a stamp in previous chapters. At the projected pressure, **150-400 bar**, PDMS gel will be deformable and incompressible as a fluid.

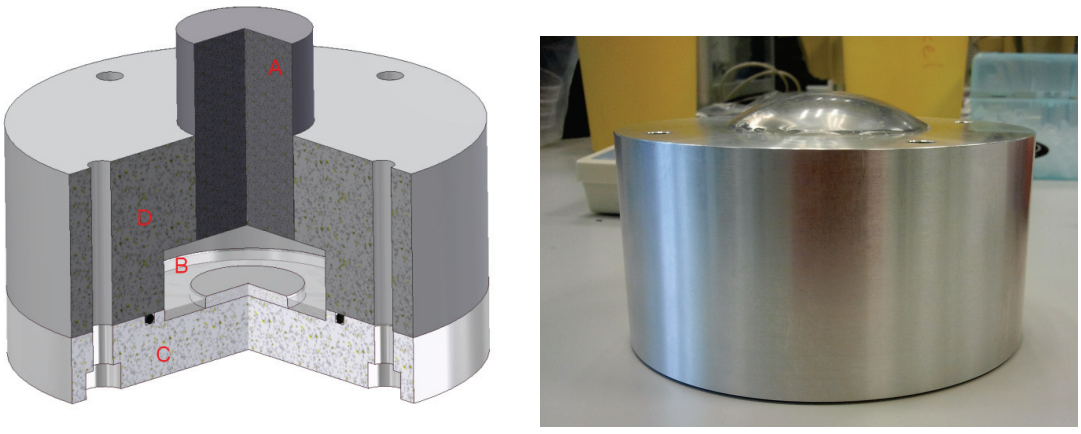

***Figure 11**. Dedicated very high pressure embossing device Embossinator 3.*

Operation principle is obvious; the bulk aluminum piston A is pressed by a hydraulic press and compresses the fluid-like PDMS disk of the size and shape of the cavity B in

top part of device. This pressure is then transferred to the nanopatterned stamp which is embossed into HSQ layer on substrate, curved or flat, aluminum disk or 50 mm wafer. The whole device (C and D) is held together by bolts. Since it is a closed hydraulic system, one can easily calculate the fluid pressure from the piston diameter and force acting on piston. This is shown as Table 1. One can see that for 400 bar pressure, a force of approximately 5 ton needs to be applied to the piston. Required clamping force is 2.72 times higher, in the ratio of the area of cavity bottom to the area of piston. Minimum tensile strength of an M8 (class 8.8 medium carbon steel) bolt is 800 MPa [91] . A single bolt is thus able to sustain approximately 41 kN, before failing, and one can easily devise that 4 such bolts (M8) can sustain more than 16 tons force, more than needed at 400 bars. Force at 400 bar is also below the minimum yield strength of used bolts, so no permanent deformation should occur.

The device was again made out of aluminum, this time of an unknown grade. PDMS discs have been repeatedly cast, using the device as a mold. I did not observed any difference in PMMS stiffness when the ratio of curing agent to the Sylgard 184 base was varied from 1:10 to 1:20, and curing temperature (65-95°C) also does not seem to be critical. The used PDMS blocks are shown in figure 12. This device was repeatedly and successfully used for imprinting in spin-coated HSQ films on flat samples, but pressure is insufficient for spray-coated HSQ films. Nevertheless, I was able to learn few important lessons from operating this device.

F [ton]	P [bar]
0	0
0.5	39
1.0	78
1.5	117
2.0	156
2.5	195
3.0	234
3.5	273
4.0	312
4.5	351
5.0	390
6.0	468
7.0	546
8.0	624
9.0	702
10	780

Table 1. *Conversion of force to hydrostatic pressure for 40 mm piston.*

First, the PDMS (fluid-like) based device is inherently a lot safer than the compressed gas system. Higher pressures are easily achievable. A fair share of the positive results reported in next chapter was achieved using this device.

Second, the device disassembly was extremely difficult, especially when higher pressure > 300 bar was used. When pressure is applied, a slit between device top and base opens, and separates them by a fraction of a millimeter, seemingly regardless of how tight the system was during assembly. The piston sinks a few millimeters into the cavity, filled with allegedly incompressible PDMS. After the release of force acting on piston, it does not always fully recover. Finally, when a higher piston force, 6 tons, leading to the hydrostatic pressure of about 470 bar, was used, the device ultimately failed, regardless of being previously reinforced by another 4 M8 bolts, as shown on Figure 12.

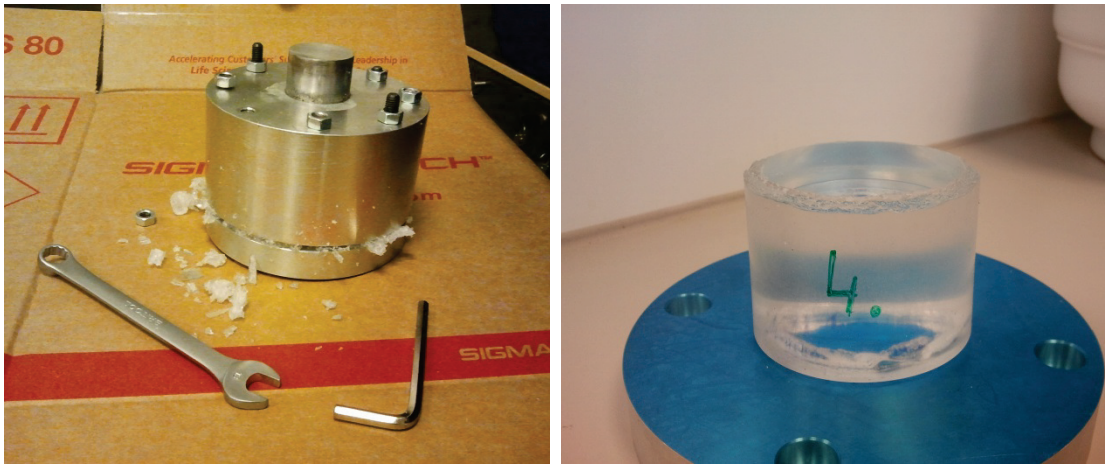

***Figure 12**. Photograh of Embossinator 3 after its ultimate failure (left). Used PDMS disc (right). Note damaged edge of disc due to creep out of cavity.*

Next I will explain how all of those effects described in previous paragraph are related. One can calculate that the piston force, needed for, say 300 bar of hydrostatic pressure, is approximately 4 tons, and the same force multiplied by 2.72, is then applied to the bolts. Hence, about 10.8 tons of force is applied. Load proof strength of 4× M8 bolts is 11.1 tons, minimum yield strength is 12.9 tons and minimum tensile strength is 16.1 tons and if 8 bolts are used, one can double those numbers. This should be perfectly safe and there is no reason why the device opening was a two-man job with heavy duty tools.

The answer lies in the right panel of Figure 12, with photo of the used PDMS disk. Note the edge damage. I was able to observe that PDMS clearly acts like a fluid and creeps into even a tiniest slits, such as the one between top and bottom of my device, or one between piston and top part. This, together with PDMS compression, explains why piston sinks a few mm into cavity, and why the piston does not fully recovers. It also gives a hint on the difficulty of opening, as the system stays pressurized and is opened under tension. It, however, does not explain why I was able to clearly observe plastic deformation of the used steel bolts, where a thread pitch on used bolts changed. For that, one has to look on another effect, transient, elastic bolt elongation, which I observed and later found that this is called "Tie-Rod Stretch" and is known in some hydraulic systems [92] . From basic mechanics, we can calculate elongation of the stretched member to be:

$$elongation = \frac{L \times F}{S \times E} \tag{5}$$

Where *L* is length of a member, in our case 10 cm long bolt, *F* is the force, which is product of used hydrostatic pressure and area onto which is it projected to at the "bottom" of the Embossinator, *S* is the bolt(s) cross-section and *E* is Young's modulus of used steel. Once this elongation is calculated, it explains the temporary slit between top and bottom of my device, which appears once pressure is applied. This slit, easily 0.5 mm wide (see table 2), allows PDMS to creep even further. And, as it creeps, area onto which the hydrostatic pressure is applied grows, with the square of diameter growth. So grows the force on the bolts, which leads first to plastic deformation and then, finally, to critical failure. This was observed as well, in my case it was a shear failure of a nut, when 6 tons of pressure was applied for system reinforced with 8×M8 bolts. Initial force on the bolts was cca 16 tons, a tensile limit is 32 tons. After approximately 2.5 minutes, when PDMS is creeping into now elastically open 0.2 mm

slit, the diameter onto which the hydrostatic pressure is projected grows, the force grows with a square of that diameter, exceeding 32 tons and device ultimately fails.

After this, I was unable to open the device again, and it was accomplished only with the use of an angle grinder powertool.

bolt	Hydrostatic pressure [bar]		
	500	750	1000
4xM8	0.425	0.638	0.851
8xM8	0.213	0.319	0.425
4xM12	0.189	0.284	0.378
8xM12	0.095	0.142	0.189
4xM18	0.084	0.126	0.168
8xM18	0.042	0.063	0.084
4xM22	0.056	0.084	0.113
8xM22	0.028	0.042	0.056

Table 2. *Elastic elongation of tightened bolts in mm. 10 cm long bolts, used in an Embossinator with cavity diameter of 66 mm elastically elongate after pressure is applied, which opens a slit, where fluid (PDMS) can creep out of the cavity.*

Finally, in late January 2013, the last device, an extremely high pressure embossing device, the **Embossinator 4**, was developed. It reflects all knowledge learned and incorporates a few advanced features. The system is shown in the figure 13. The system is made of a tool steel and uses 8 massive M18 bolts.

First, to prevent any PDMS creep between top and bottom, I have designed a tiny 0.3 mm, blade-like rib at the bottom edge of top part cavity. This steel rib is then forced into a polyethylene (PE) spacer, resulting in both plastic and elastic deformation. Once pressure is applied, the system opens, but, due to 8 massive M18 bolts, only by 0.04-0.08 mm, as shown in the Table 2. Since the rib is already 0.3 mm in the PE spacer from assembly, this slit is closed by an elastic springback of PE spacer.

Second, to address creep of PDMS between piston and bore, a deformable 0.5 mm thick PFTE foil is used on the top of PDMS disk and the piston is heavily lubricated by high viscosity Teflon-based vaseline.

This allows the use of this system at pressures up to **1000 bar**, as I tested, but I used only up to 800 bar with a real nanopatterned samples. Actual double-curved nanoimprited surfaces have been prepared successfully with this system. The assembly and disassembly is easy, takes only minutes, the system is cleanroom compatible and is usable directly, without any further modifications.

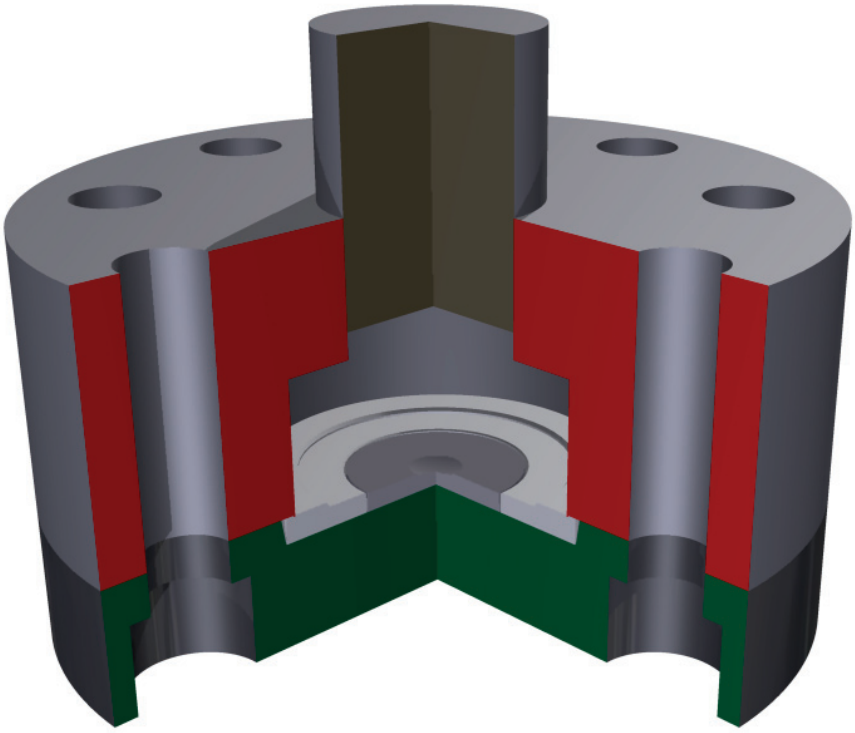

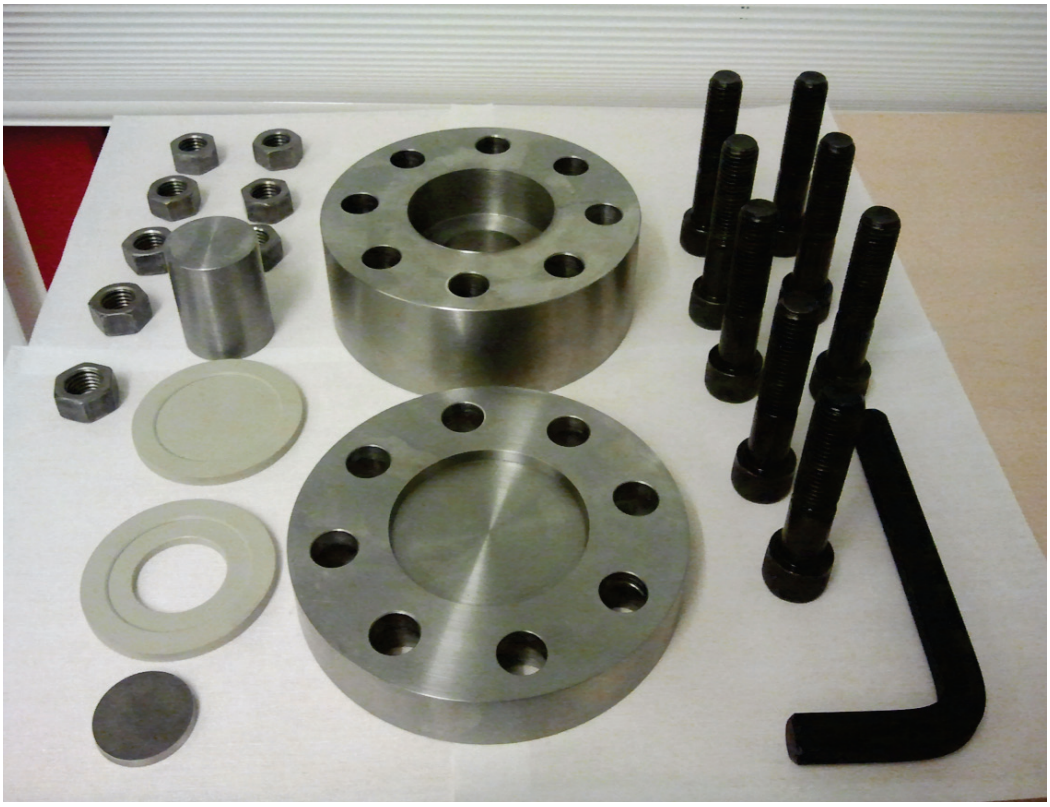

Figure 13. *Dedicated extremely high pressure embossing device Embossinator 4.*

HSQ layer deposition development

Hydrogen silsesquioxane was developed as an ultra-high resolution e-beam resist. Typical layer thickness used in this application is less than 50 nm. This thickness is insufficient for the purposes of both roughness reduction and of nanoimprinting. New methods and parameters for the deposition of a much thicker layer need to be developed. Out of the possible methods, one can quickly identify spin-coating and spray-coating as the most suitable candidates. Dip coating is impractical, provided the cost of HSQ solution (10.000 EUR per liter). A spray-coating process was shown in the previous chapter; and spin-coating is described here. In Figure 14 I present spin curves for the FOx-16 resist on 50 mm substrate, with the aim to reach a film thickness over 1 µm, as measured by mechanical profiler.

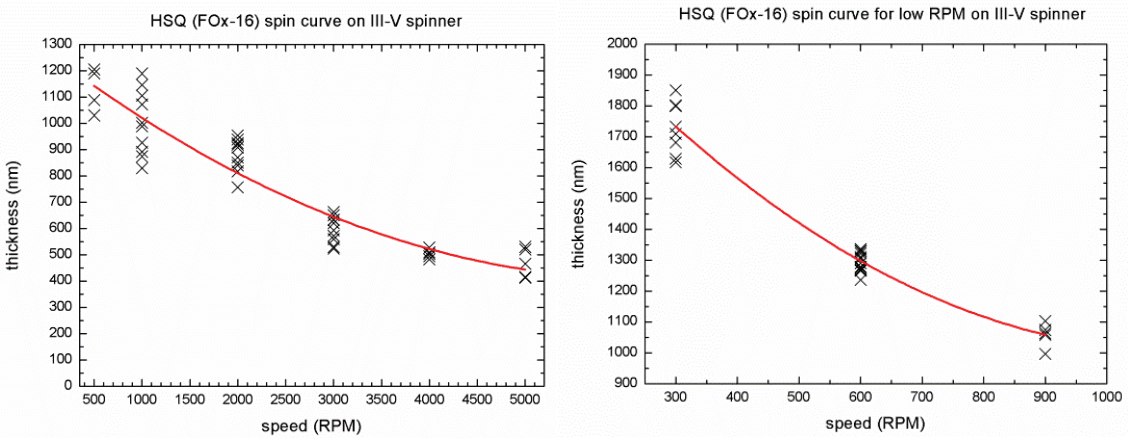

Figure 14. *Spin curves for HSQ on 50 mm substrate. Left: A regular RPM range. Right: Very low RPM range needed to obtain layer thicker than 1000 nm.*

One can see that speeds as low as 300-900 RPM are needed. If this speed is used alone, result is a massive, few millimeters wide edge bead, a region with excess resist at the edge of substrate. One can however observe, if spinning with an open lid, that the interference colors changing, which indicates thinning of HSQ film stops after a certain time. It can be concluded that film is stable after that time and it is possible to accelerate to remove/reduce the edge bead. This time is the shown in table 3.

Speed [RPM]	time [s]
300	8
600	10-13
900	20-21

Table 3. *Spin-coating time necessary for the stabilization of the center of an HSQ film.*

So, if one waits this time, the HSQ film in the center of 50 mm wafer is already stable and solvent free. It is possible to accelerate quickly to 3000-5000 RPM and continue spinning for another 15 s. At the end of this modified process, no edge bead formation is visible and I was able to reproducibly achieve thicknesses above 1.7 µm on flat substrates, as demonstrated by the mean thickness of 1733 nm, with SD of 78.6 nm (N=10), and median 1721 nm at 300 RPM.

Conclusion

To conclude this chapter, I was able to develop tools for nanimprinting on HSQ films. First, I developed a process to form a very precise nanopattern using interference lithography. This pattern was transferred into electroplated nickel foils of selected thickness, 25 to 350 µm, some of which may be used directly as an insert for injection molding of polymers. Patterns on nickel foils were transferred to the Zeonor COP polymer foils with thicknesses of 50,100 and 188 µm. The prepared polymer foils as well as Ni masters have been thoroughly characterized.

Second, I developed a few dedicated devices for hydrostatic imprinting; the last one was tested at pressures up to 1000 bar, and used with the real HSQ nanopatterned sample at pressures of up to 800 bar. Actual non-planar nanoimprited surfaces have been prepared successfully with this system.

Third, an HSQ spin-coating process, originally used for films < 50 nm was studied and optimized to produce films thicker than 1.7 µm.

Supplementary information

Technical drawings of prepared devices are available as an Appendix B of this dissertation.

Chapter 7: Nanopatterning of HSQ coated double curved surfaces

This chapter shows the results of nanoimprinting into spin- and spray-coated surfaces, using stamps from a Ni foil, and from a Zeonor polymer foils. Imprinted surfaces are flat Si wafers, and aluminum cones and spherical caps. The imprint depth as a function of pressure and stamp material is shown and pattern distortion is analysed.

Nanopatterns on curved surfaces are usually realized with soft elastic stamps made from materials such as PDMS or PMMA, as reported by Choi *et al*. [5], where spherical substrates with radius of 10 mm were used. Polyvinyl alcohol and nickel stamp was used by Hong *et al*. [6], where the force was delivered by gas pressure (5 bar) and a cylindrical substrate with radius of 20 mm was used. Weng *et al*. reports [8] an interesting method where a flexible, PDMS stamp is cast with a magnetic layer, then applied to the surface with 1 bar of gas pressure , and after reaching sufficient contact with the substrate, an electromagnet is activated which increases the force to 13 bar. Fully functional, insect eye-like PMMA hexagonal lenses on curved spherical surface with radius of 3.5 mm have been recently (2012) reported by Liu *et al.* [9]. Another quite successful set of experiments with PMMA and PDMS transferred onto highly non-planar ribs and channels for microfludics was reported by Farshchian *et al.* [10-12].

All of such systems, where pattern is formed in a PMMA or another plastic, are unfortunately not a viable option for a heavy duty, high temperature use as mold insert for injection molding. For that, a good option is to nanopattern HSQ films.

When HSQ is mentioned in texts regarding nanopatterns and imprinting, it usually serves as a tool or a stamp, as something you are imprinting with, not as something you are imprinting to. HSQ is a highly versatile material; films may be nanostructured using variety of methods, including x-ray lithography, e-beam lithography [62,63], ion-beam lithography [31,93], and room temperature nanoimprinting, the latter of which was reported by Matsui *et al.* [65,94], Igaku *et al.* [95], Sung et al. [96] and Nakamatsu *et al.* [97]. Reported articles note problems with high pressure needed for imprint, 50-400 bar, where imprinting does not work reliably even on planar substrates, and HSQ is highly sensitive to temperature and humidity. A recent paper by Kang et al. [66] reports the use of a high boiling point solvent to reduce the issues with pressure, although this solution is unfortunately not viable with a Ni stamp.

There is also an interesting recent report by Yang *et al.* [98], where a nanopatterned PDMS film is cast, coated with HSQ and used to direct-print HSQ to substrates, including cylinder with unknown radius.

Methods and materials

This section describes how an HSQ coated non-planar surfaces have been patterned, how the stamp stretch was assessed, and how the system was modeled.

Nanoimprinting into HSQ films

Non-planar highly curved RSA aluminum substrates have been single point diamond turned by our collaborator at NTU Singapore. We carefully rinsed surfaces with acetone and IPA, blow dried and primed surface in the air plasma, using same conditions as in chapter 5. Planar aluminum substrates were prepared the same way and planar 50 mm silicon wafers, used for spin coated HSQ, were cleaned but not plasma treated.

HSQ was deposited using protocols developed in previous chapters, for spin-coated samples, HSQ was applied, sample was spinned at 500 RPM for 20 s and then at 3000RPM for 15 s, to limit edge bead formation. Spray-coated samples have been prepared using protocol identical to the one described in chapter 5.

There is, inavoidably, a delay between an HSQ layer deposition and processing. Spin coated samples have been stored in closed plastic wafer carriers for individual wafers, either with our without tiny piece of cleanroom long fiber cloth soaked with MIBK solvent to mimic reflow. The time to processing was usually less than 120 min. For spray-coated samples, regular reflow chamber with a forced circulation of solvent vapor was used and samples were exposed to solvent vapor for at least 90 min and processed immediately after removing from the reflow box.

Imprinting was carried out using specially developed devices, as described in detail in previous chapter, the Embossinators. Spin-coated samples were tested using CNI and NIL 2.5 Obducat, and actually imprinted using Embossinator 2 (up to 150 bar), and Embossinator 3 (up to 390 bar). Spray-coated samples were successfully imprinted at pressure 600 to 800 bar, using the Embossinator 4.

Imprinted samples that were characterized using AFM, were measured using the AFM PSIA in a tapping mode. SEM characterization is described elsewhere. Optical microscopy was done using low magnification optical microscope with digital image capture device.

Pattern distortion assessment

One can expect pattern distortion due to strain from intrinsically planar stamp conforming to the double curved substrate.

FEI Nova 600 NanoSEM, operated at a low vacuum mode to limit sample charging, and the variable pressure secondary electron (LVD) detector, was used to characterize nanopatterns formed in HSQ film on non-planar surfaces. We used strictly a top view, zero stage-tilt geometry, and avoided use of a beam tilt, while keeping also the magnification and focus as fixed as possible during image series. Sample movement was realized solely by the stage movement.

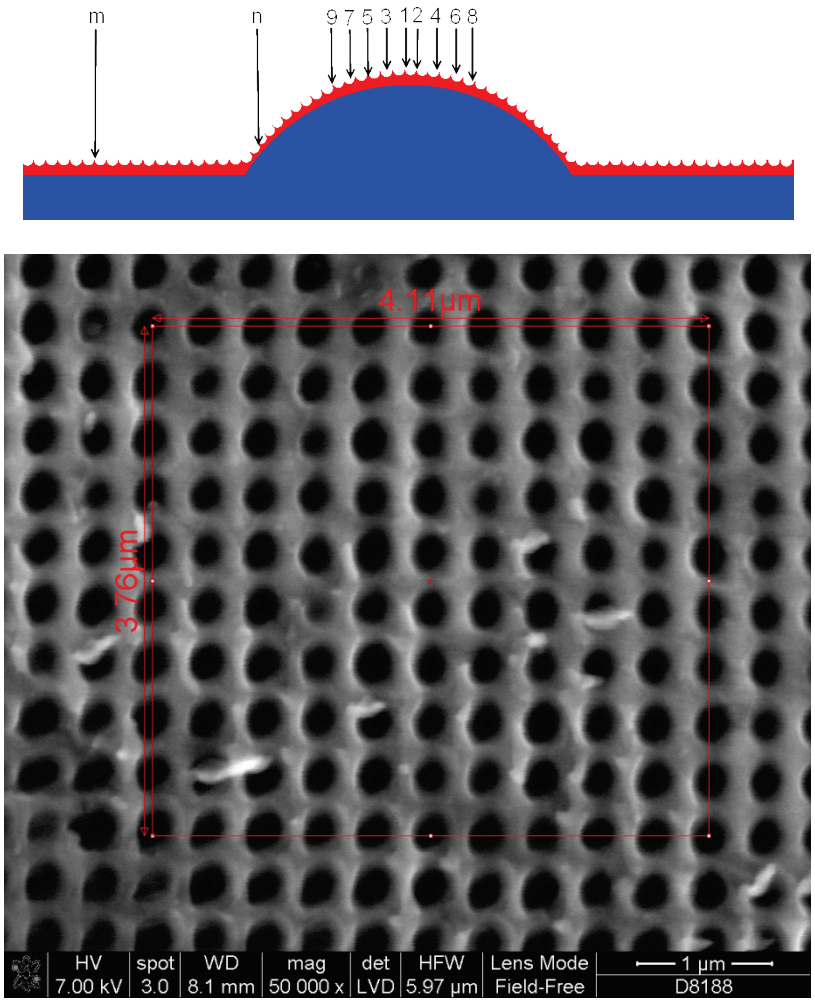

***Figure 1**. Pattern distortion assessment. Top view SEM images are taken at the center of nanopatterned curved structures, and in increasing off-center distances on alternating sides, as indicated by the numbers at the top panel. With known off-center distance for each image, one can measure distances on each micrograph, divide them by the number of periods in the X and Y directions, and calculate the X and Y periods and the mean period at each investigated spot. Note the need to compensate data by geometrical mapping, as the period seen at point* n *is in fact larger than it appears.*

Collected data have been processed to extract the period in both directions and the mean period for each investigated spot. There is obviously a need for the "geometrical mapping" or "tilt correction" of collected raw data, as the sample is non-planar and the period in the tangential plane for each spot is larger than observed period. This effect is far more significant for points far off the structure center. The corrected period Λ_{REAL} is then calculated using:

$$\Lambda_{REAL} = \frac{\Lambda_{MEASURED}}{\cos(\vartheta)} = \frac{\Lambda_{MEASURED}}{\cos\left(acrsin\left(\frac{l}{R}\right)\right)} = \frac{\Lambda_{MEASURED}}{\sqrt{1-\left(\frac{l}{R}\right)^2}} \quad (1)$$

Where ϑ is

$$\vartheta = \arcsin\left(\frac{l}{R}\right), \quad (2)$$

and the l and R are distances on a spherical surface, according to the sketch below.

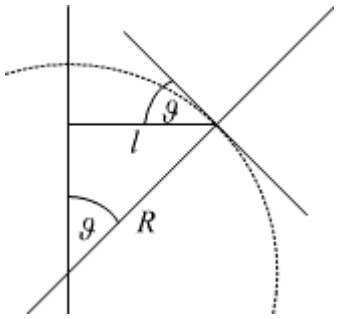

Another SEM, LEO 1550 (currently Zeiss) was used for the measurements on actual used and plastically deformed Ni masters, as they are, unlike cured HSQ films, not dielectric and one can easily use high vacuum mode.

For the estimation of the error in the measured period, we assumed that our measurement bar may be positioned up to $^1/_8$th of the actual period length in error. If we assume that half a period is of the opposite color, then ¼ is a visibly wrong position and $^1/_8$ th is realistic assumption for upper limit. This 1/8 (12.5%) length is then divided by the total number of periods measured with that particular measurement bar. We added 0.12% as the maximum possible rounding error. This method leads to the error of 1.1-1.4% for the HSQ surfaces, and less, below 1% for used foils, where we were able to use another SEM, at a lower magnification, thus dividing the same 1/8 period length with more periods.

FE model

The model of deformation of the foil developed by our collaborators at DTU MEK uses the following assumptions, nickel Young's modulus E=200 GPa and Poisson's ratio 0.31 as was found in the literature [99]. Standard mechanical model based on the solution of static force equilibrium equations was used, and the large strain theory was used for the strain description, which renders the system geometry non-linear. The yield stress was found by backing it from the stress-strain curve of Ni, as found in [99].

The contact between nickel stamp and HSQ coated aluminum substrate was modeled using standard Coulomb friction, where the coefficient of friction, empirical property of materials in contact, was found in literature [100] to be 0.35 between nickel and aluminum, disregarding the HSQ layer, for which the experimental friction data are not available.

The equation system was numerically discretized, using finite element method and solved using the general purpose FE code ABAQUS.

Results and discussion

We were able to devise, successfully develop and test process for nanoimprinting into HSQ films deposited by spin-coating and by spray-coating on planar and on a set of double-curved substrates with very high curvatures (radius as low as 500µm). This process involved an extremely high pressure (600-800 bars). An example of a nanopatterned HSQ on a flat and a highly-curved spherical substrate is shown in figure 2.

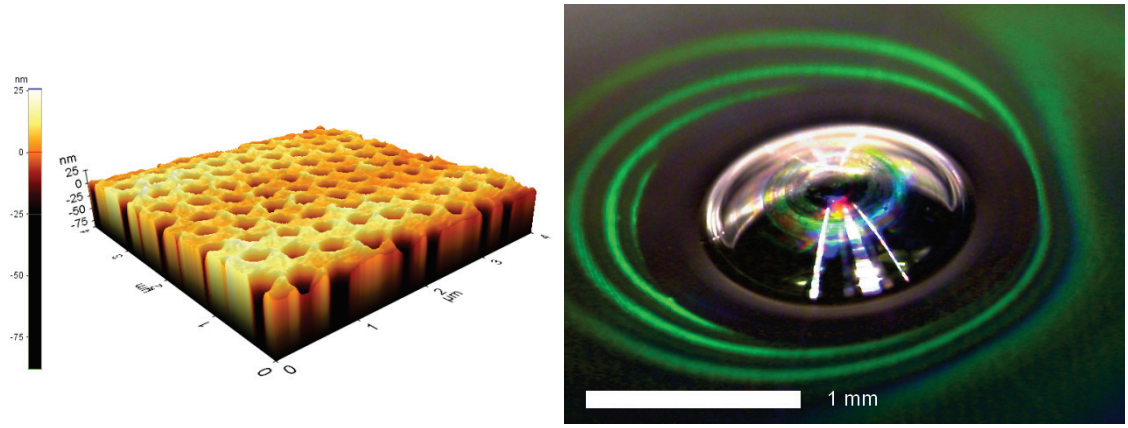

***Figure 2**. Example of patterns imprinted in HSQ film. Left: One of the early samples, flat, imprinted at 236 bar for 10 min. Depth (from AFM) 75±9 nm, 70% of master. Right: Optical micrograph of a nanopattern (1 min@650 bar,) with cured HSQ film on a spherical cap, radius 1 mm, base diameter 1.2 mm, heigth 200 µm. Note the presence of diffraction effects.*

Such patterns have been thermally cured and can be used as mold inserts for an injection molding of polymer articles.

There are some important observations regarding imprinting into HSQ. First, we used spin-coated HSQ films and both Zeonor and Ni stamps and investigated depth as function of pressure, as shown in figure 3, top panel. One can see that no imprint is achieved at 7 and 60-70 bars, which is the limit of both commercial devices used.

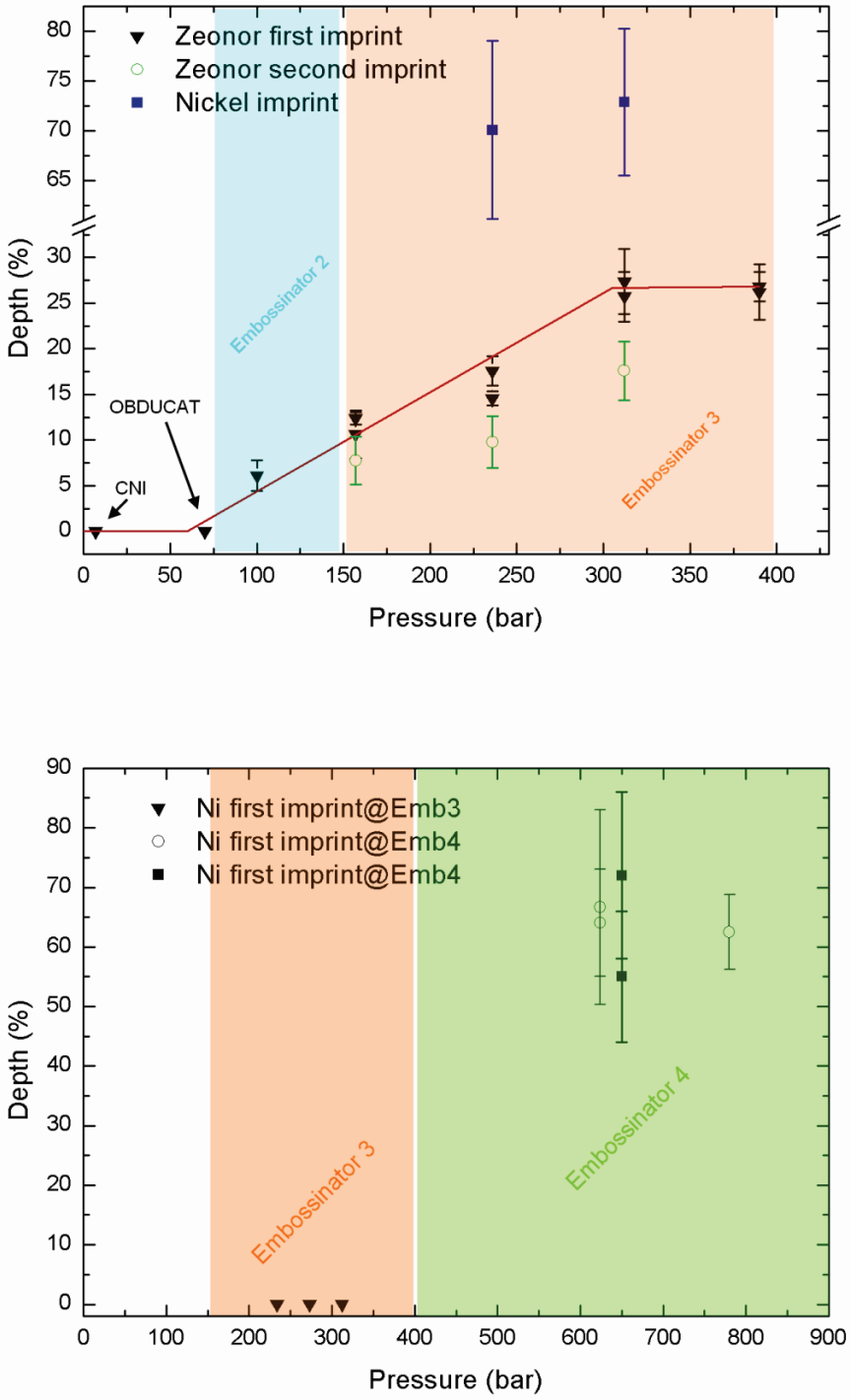

***Figure 3**. Depth of an imprint in HSQ as a function of the embossing pressure. Top panel shows results for spin-coated HSQ films. Bottom panel shows results for spray-coated HSQ films. Results, observed for these 2 methods differ.*

Only when the pressure is increased to 100-150 bars, which is an effective limit of Embossinator 2, an imprint is made. Note the depth; it is only 5-10% of the Zeonor master depth. Interestingly enough, we did not observe any direct effect of solvent reflow. (as used in chapter 5) This was realized with the presence or absence of a

cloth, soaked in MIBK solvent, in a closed transport box during transport from cleanroom to lab. There is also no evident effect of delay, or time between the HSQ film deposition and processing. We tried to keep this time as short as possible, but since the disassembly of Embossinator 3 was rather slow, this time was often 30-90 min.

Imprints become much more reliable with new device, Embossinator 3, which allowed reaching over 300 bars routinely. Achieved imprint depth increased, with increased pressure, but only to some extent, to approximately 25% of master depth, as demonstrated in Figure 3 top panel. When the pressure was increased further, to 390 bars, making the device operation seriously obnoxious, depth did not increased any further.

There is a possibility that, at such pressures, Zeonor foil is plastically deformed, hence, no further increase of depth. To test this, a few experiments, where the same piece of a Zeonor foil was used more than once, was carried out, and the result is rather clear, as can be seen on figure 3. The second imprint with the same foil is always more shallow. Moreover, if an AFM is measured directly on the Zeonor foil (see figure 4) one can see that master depth is reduced, likely due to plastic deformation.

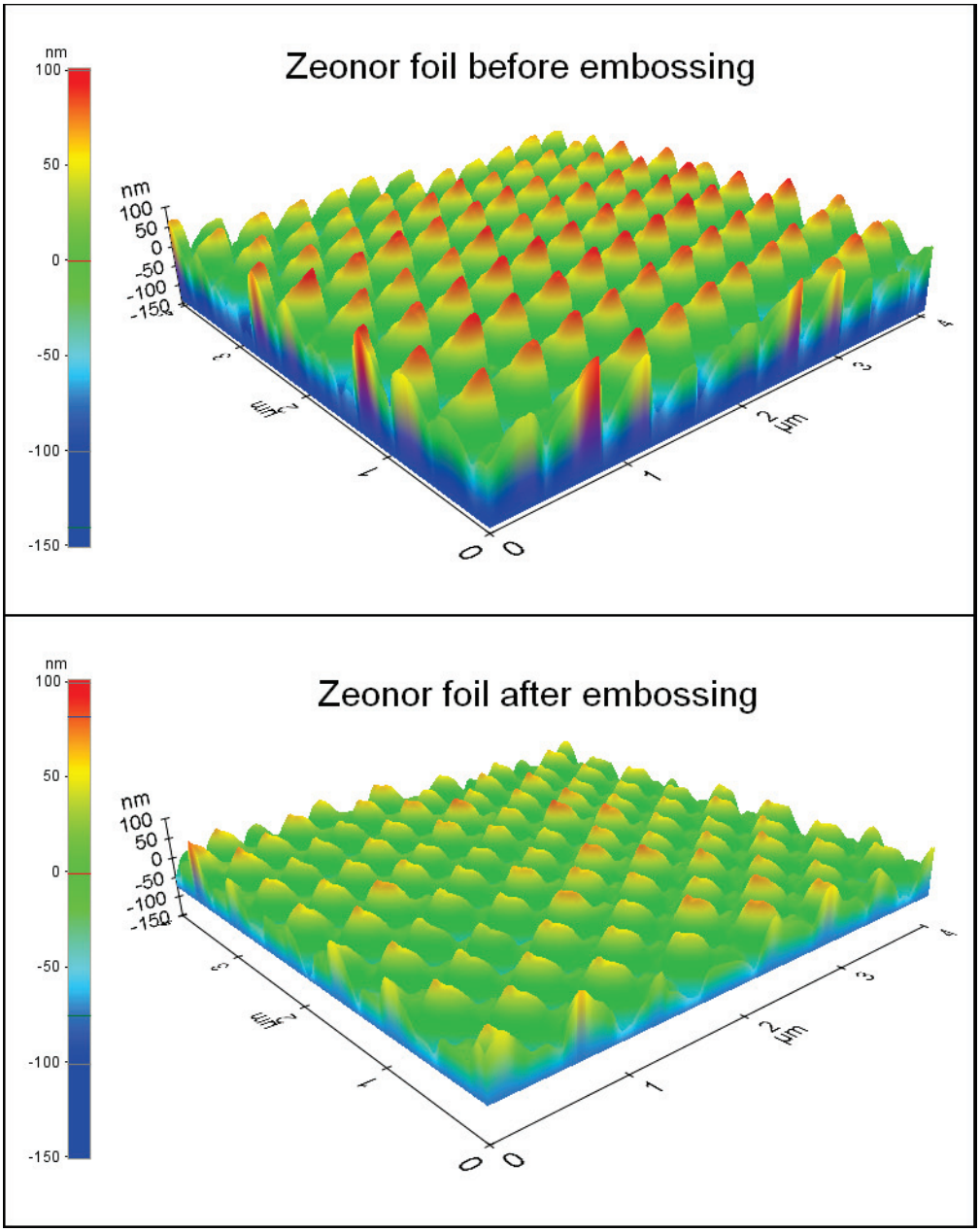

***Figure 4**. ZEONOR polymer foil is plastically deformed during an embossing into the HSQ film as evidenced by an AFM measurement. Top Panel: Fresh foil shows a nanopattern depth of 179.4 ±16.5 nm. Bottom panel: The same foil was used once to emboss into HSQ film at 236 bars and a nanopattern depth is reduced to 95.1±11.2 nm. Additionally, the elastic portion of a deformation is transient, therefore is not captured.*

This observation was the reason to review the proposed process (Figure 1 at Chapter6) and drop the use of disposable polymer foils. We prepared few more sets of nickel masters, this time with lower thickness; FDTS coat them, and used them directly on HSQ film, skipping steps with Zeonor. This immediately yielded much better imprints, with a higher replication depth both in absolute depth and in ratio to the depth of master, as demonstrated by 2 points in figure 3, top panel, at 70% and 75% depth.

Naturally, the obvious question is, does the nickel foil plastically deform as well? If so, then to what extent? This was tested and result is shown in figure 5. We used same piece of nickel foil three (!) times, imprinting each time for 10min at 236 bars. Initial depth was 107±6, final depth 106.7±8 nm, well within the SD, which suggests no permanent damage to nickel at 236 bar.

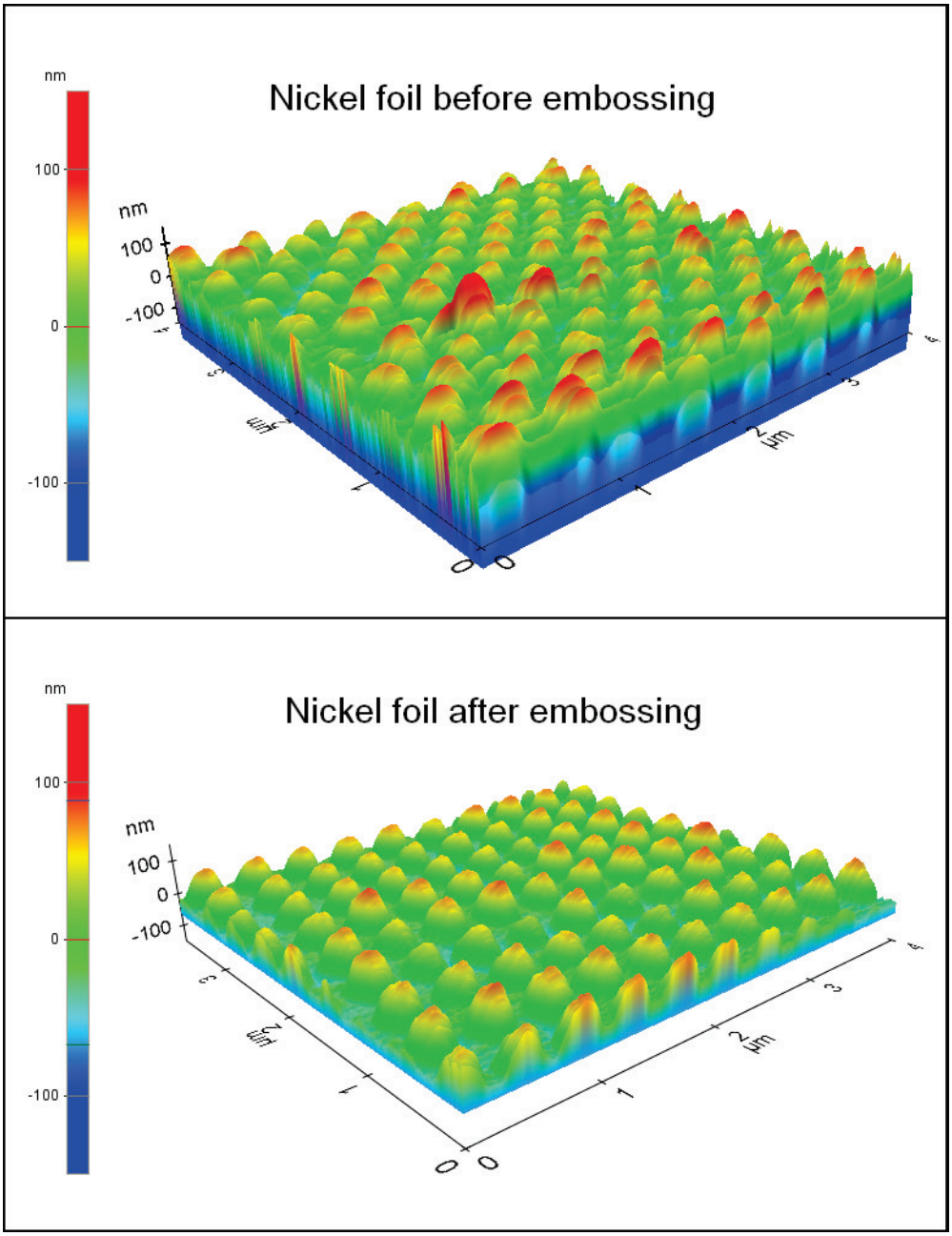

***Figure 5**. The nickel foil is not deformed during an embossing into the HSQ film as evidenced by an AFM a measurement. Top Panel: Fresh foil shows a nanopattern depth of 107±6 nm. Bottom panel: Same foil was used three times (!) to emboss into HSQ film at 236 bars for 600 seconds, and a nanopattern depth is not reduced, but stays at 106,7±8 nm. The depth of a replicated nanopattern is approximately 70% of the depth on the nickel foil. However, possible elastic portions of deformation could be transient and therefore not captured, but may be responsible for the remaining 30% or a part of it.*

Again, in this stage the process looks like a well working solution, where reliable imprinting was achieved at 236 bars using Ni. Note that all experiments discussed so far involve spin coated HSQ, i.e. top panel of figure 3.

Real, non-planar samples need to be spray-coated, using a previously specified protocol, described in the chapter 5. Once again, there was no imprint regardless of variation in reflow time, embossing time and the pressure variation from 234 to 312 bar, which were perfectly suitable conditions for spin-coated films.

When a further increase of pressure was attempted, catastrophic failure of Embossinator 3 occurred, despite being reinforced by 4 more tempered carbon steel bolts. Reasons are discussed in detail in a previous chapter, together with lessons learned. This allows (and dictates) building of one last device, Embossinator 4, which was tested in late January 2013.

Since the device is capable of reaching 1000 bar, additional experiments with spray-coated HSQ have been devised and performed, as shown in the bottom panel of Figure 3. Finally, using the pressure of 600 to 800 bar (figure 3), good replications with depths well over 50% were observed on spray-coated HSQ. This system is suitable for the double-curved mold surfaces. At least 14 substrates have been imprinted, showing signs of nanopatterning (diffraction of visible light) but not all the depths were investigated with AFM due to lack of time.

Occasionally we have been able to observe minor issues with particles, as shown in figure 6. The diffraction on and around particles is reduced, indicating a similar reduction in pattern depth, which was indeed confirmed by the AFM, as shown in figure 6 bottom right panel. The source of particles is not entirely clear. Since the experiment was carried out in a class 10 cleanroom, dust or some other contamination is not likely source of particles. Provided that they start to appear during reflow, when is the HSQ film exposed to the MIBK solvent vapor, even prior to the embossing, one can speculate that the source may be the spray-coating process itself. It produces airborne semi-dry particles, and if some of them deposit to the surface after a delay, already partially cross-linked, they may be sufficiently hard to produce this effect. They can possibly act also as some sort of a nucleation centers, and, when the rest of the film softens as solvent is introduced, they may facilitate cross-linking in their vicinity. Another proposed explanation is that, as the HSQ solution is ultrasonically atomized during spray-coating, local ultrasonic cavitation may occur and that leads to locally increased pressures and temperatures, which cross-links HSQ and forms particles or their seeds. The observation of particles is not exemption, but not a rule, and a thorough cleaning of the spray-coating system, including the HSQ delivery tubing and syringe seems to alleviate the problem.

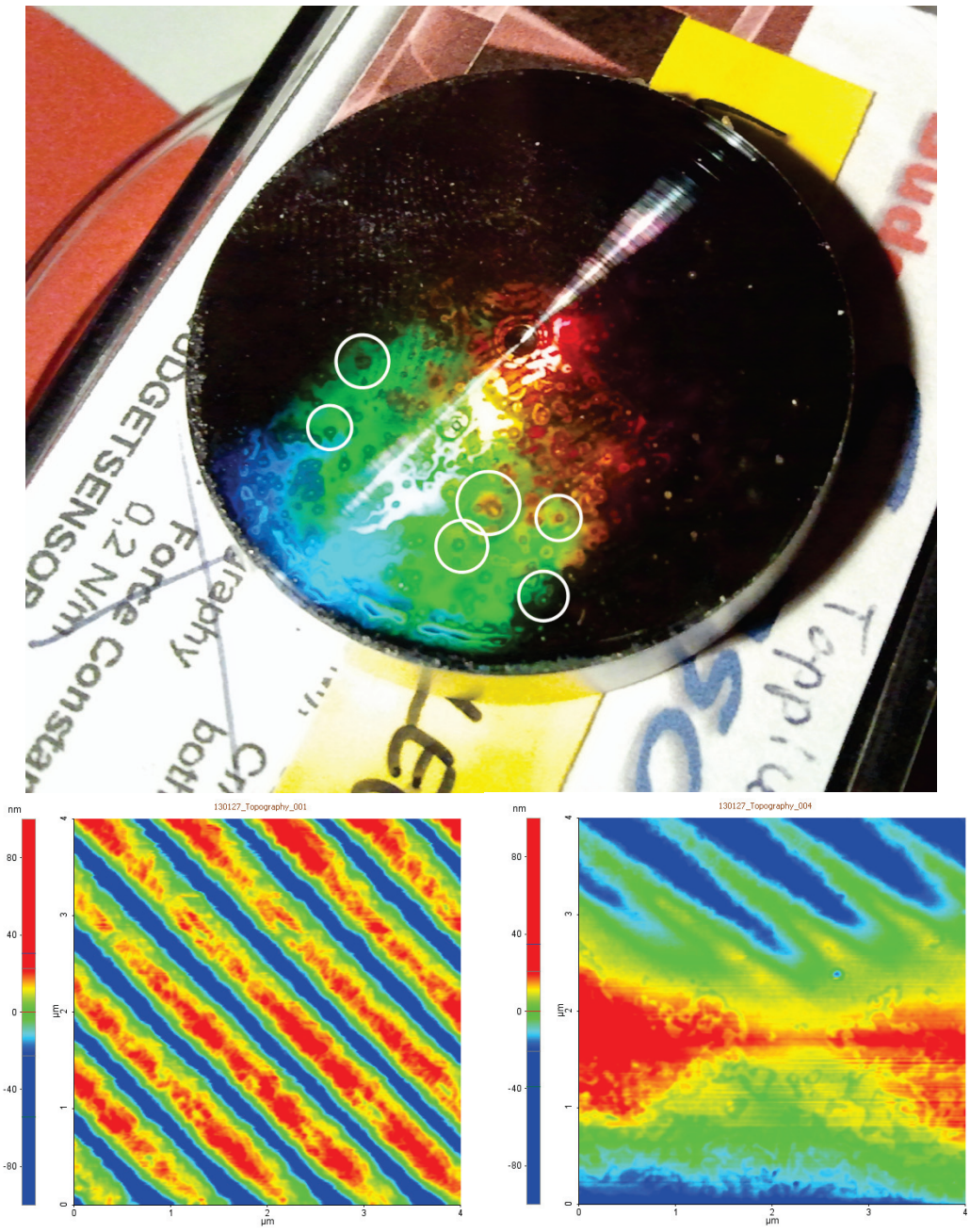

***Figure 6**. An HSQ coated disk, with tested conical surface in the center. The photo (top) shows clear signs of a diffrraction on nanostructures imprinted in the HSQ and the particle contamination, marked with cicles. AFM shows nice, well replicated pattern with depth over 50% of the master and a gradual loss of replication in the vicinity of a particle.*

In the figure 7 is shown a selection of prepared double-curved surfaces, together with their respective profiles. We can see the spherical surface cavity, with the radius of 2000 µm, the series of spherical caps with the radii of 2000, 1000 and 500 µm, and the cones, corresponding to the unsuccessful manufacturing of spherical caps with the radii of 1000 and 500 µm. We can see that all those substrates have been nanopatterned as by the diffraction of a white light from the microscope illumination.

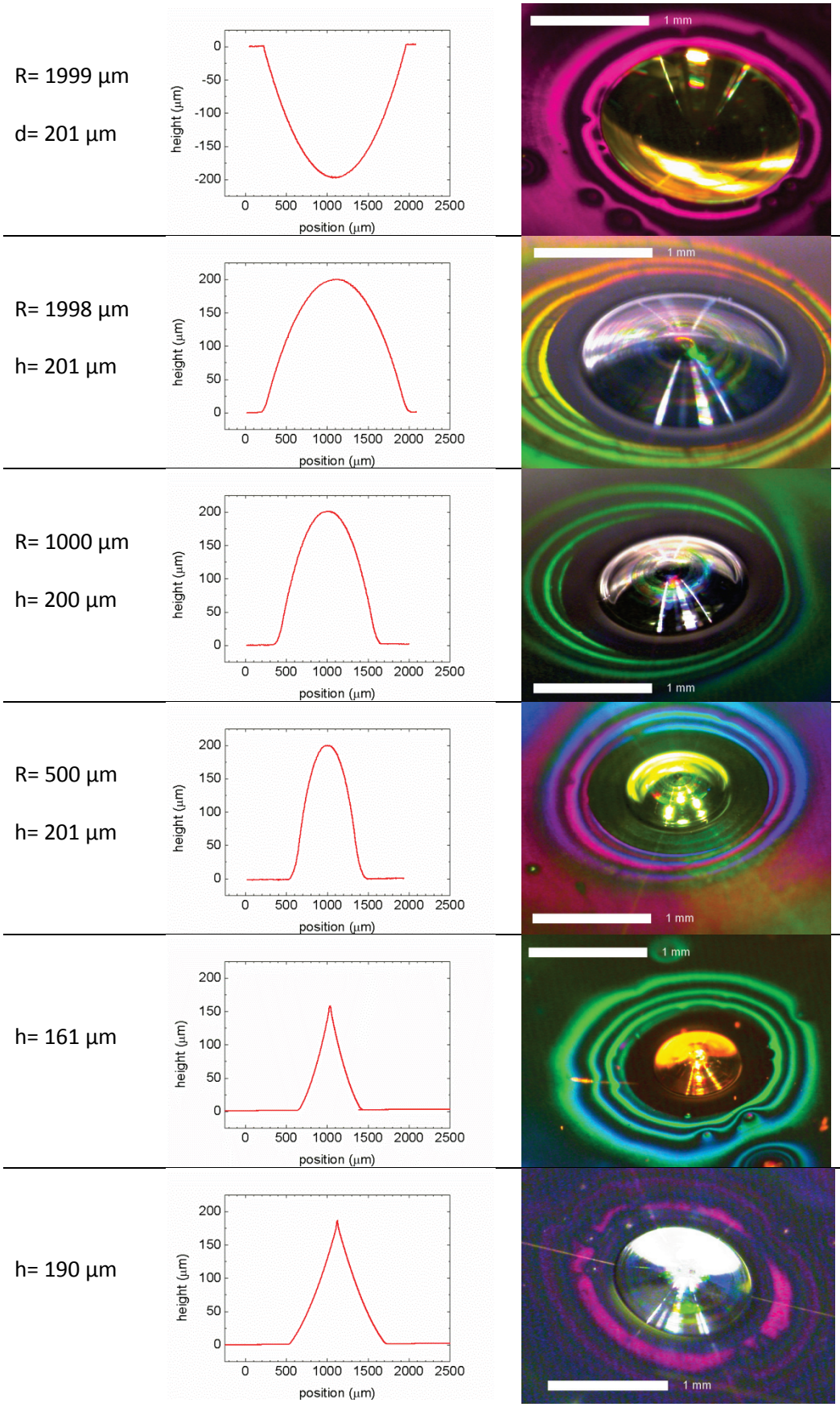

Figure 7. *The right column shows a gallery of the nanopatterned non-planar surfaces, note the diffraction, the left one shows profiles as measured by a stylus profilometer.*

Now, as the nanopatterned surfaces have been prepared, we can proceed to study the pattern distortion which can be seen as a strain of intrinsically planar stamp, forced to conform to the spherical surface. For this, only the 3 spherical protrusions with radii 2000, 1000 and 500 µm have been selected.

Using the SEM and the method, described in the first section of this chapter, the mean period of nanopattern as a function of the radial position was calculated, using the X and Y period of the imprinted nanopattern. This can be seen on the top panel of figure 8.

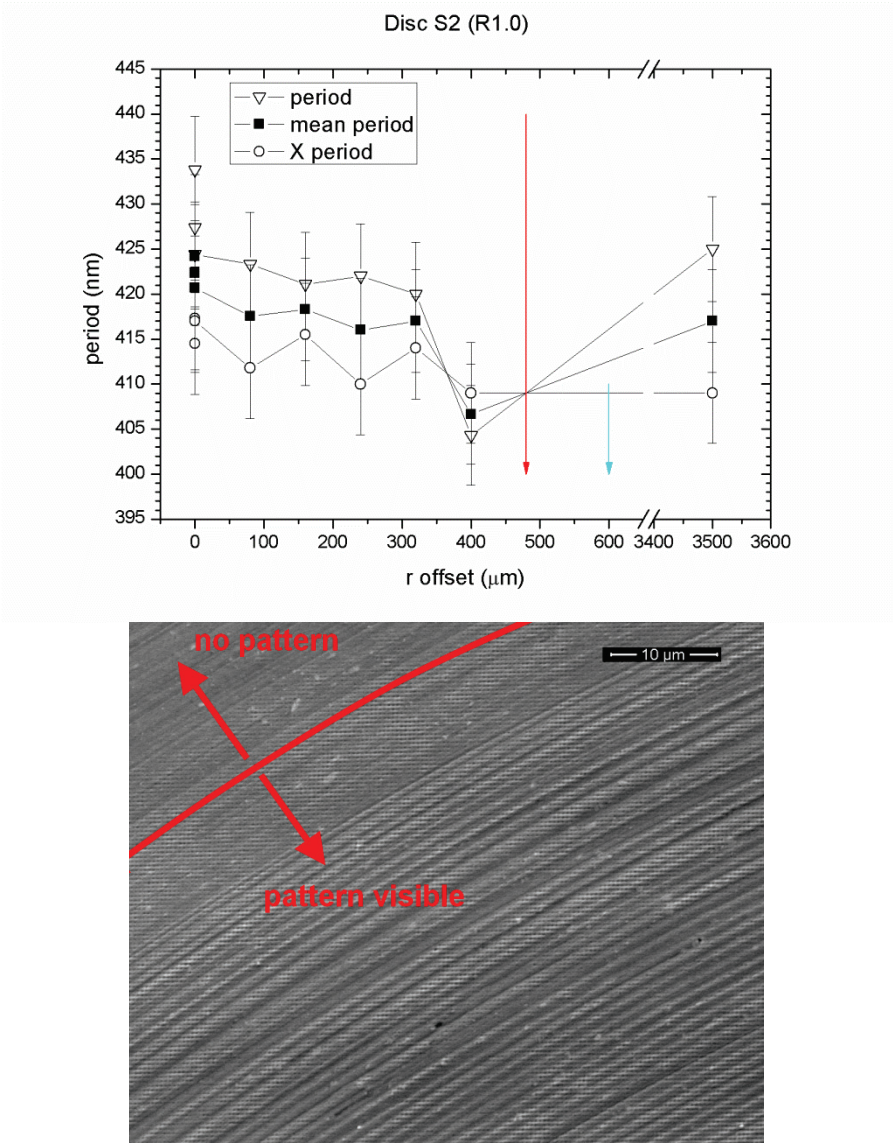

***Figure 8**. An unmapped, top-view period of a pattern on surface with the spherical radius of 1000 µm on top, and the radial imprint limit, cca 480 µm from the apex.*

Note also the red and blue markers, the blue is placed at the end of a spherical surface, where the substrate becomes planar, and red is observed limit of imprinting, the radial boundary behind which the nanopattern was not replicated. On this sample,

with the spherical radius of 1000 µm, is the boundary approximately 450 nm from the apex.

After we use the equation 1 to perform a geometrical mapping to get the real pattern period, we can compare it with the period calculated using the FE model, developed by our collaborator from DTU Mek. Lets first present some results from the model, on figure 9 are shown contourplots of the deformed nickel foils, as it stretches on the spherical protrusions. False color corresponds to the maximum logarithmic strain.

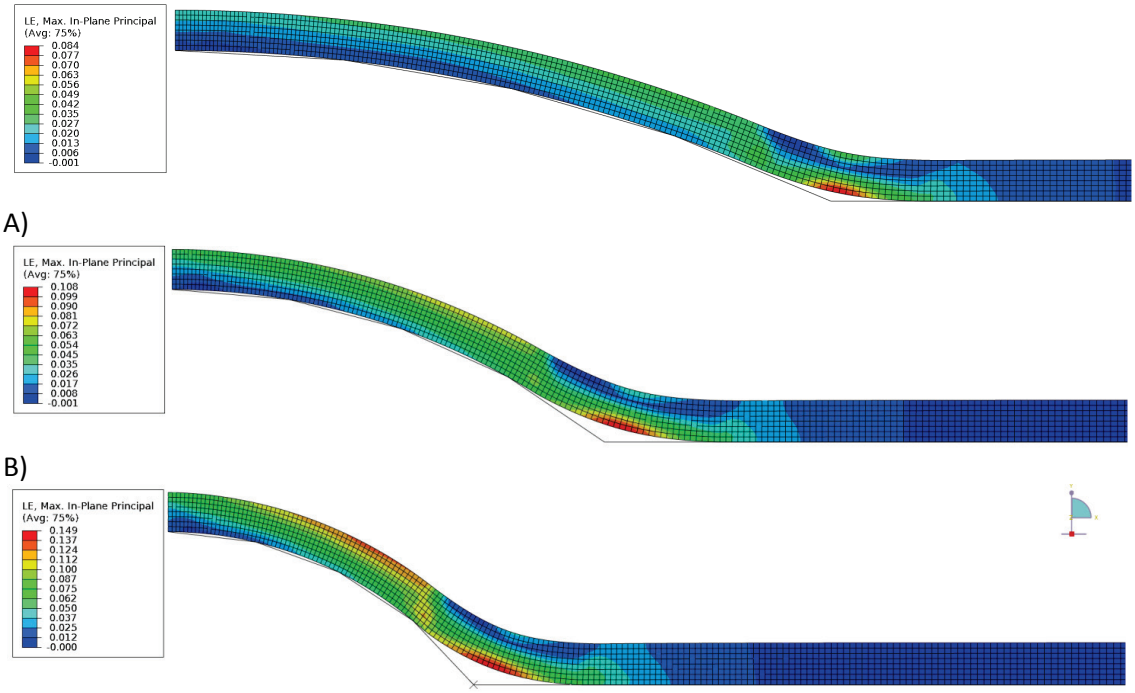

***Figure 9**. Contourplots of the deformed shapes of the nickel foils pressed down to the aluminum substrate in the three different test cases: A) 2000 µm, B) 1000 µm and C) 500 µm.*

With the strain along the surface, we can calculate the expected mean period and compare it to the actually measured, and to geometrically corrected mean period. This comparison is shown as figure 10, for all three modeled radii.

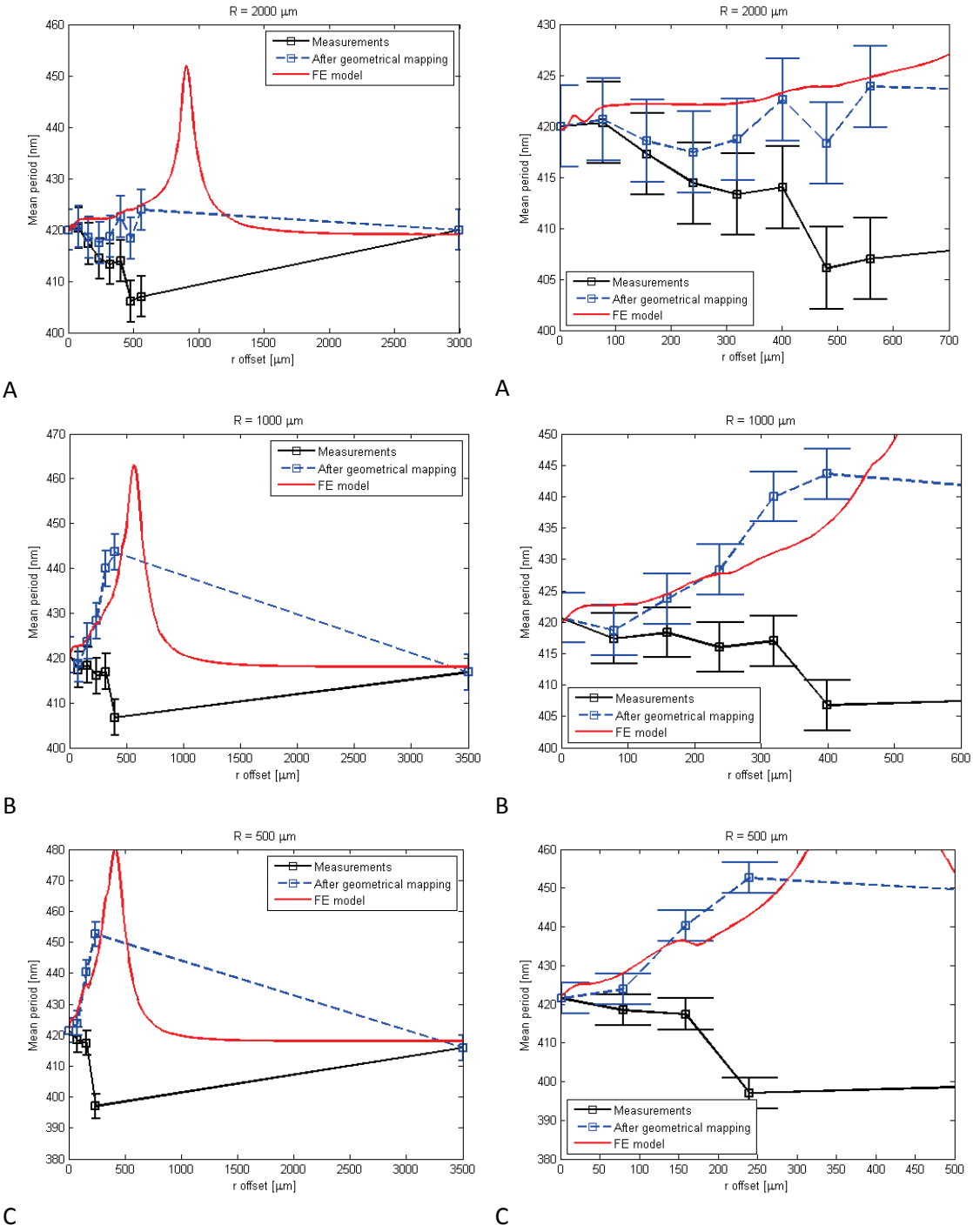

***Figure 10**. The comparison of measured and numerically calculated periods of the nanopattern. A) 2000 µm B) 1000 µm C)500 µm. The right collumn is rescalled to better show experimental data points.*

As we can see, there is very good agreement between the experiment and the FE model. From figures 9 and 10 is also clear, that the maximum strain is outside the area, where the two surfaces are in a contact, in the area where the pattern in not replicated, behind the observed radial boundary. And, if the contact pressure between the nickel foil and the aluminum substrate is extracted from the model, we can plot it

as a function of the radial distance, as shown in figure 11. As we can see, the contact pressures, devised from the FE model for each radius, show increase and a sudden drop, which is perfectly corresponding to the radial boundary, behind which is the pattern no longer replicated. This boundary, observed experimentally is marked by the dotted lines in figure 11.

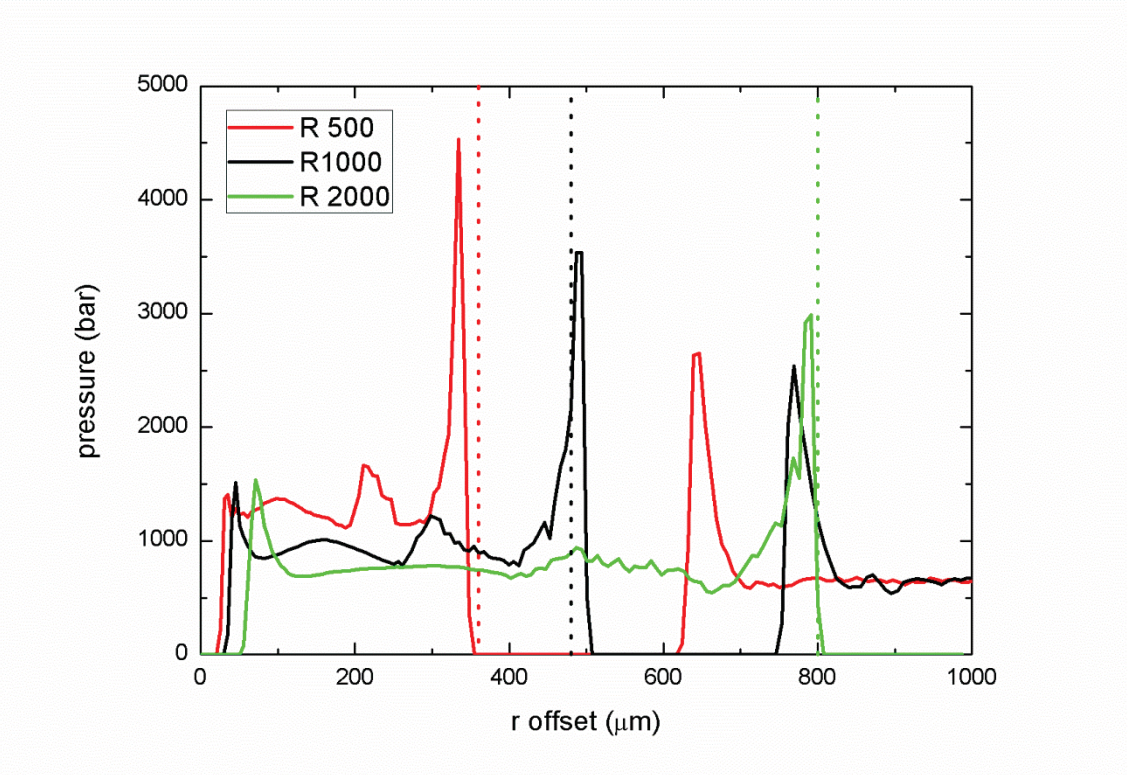

Figure 11. *The contact pressure between the nickel foils and spherical substrates, as calculated from the model (full lines) shows sudden drop on the position which corresponds to the experimentally observed radial boundary (dotted lines) behind which is the pattern not replicated.*

Conclusion

We successfully imprinted nanopatterns into HSQ films on both planar and non planar, double-curved surfaces, with a radius of curvature as low as 500 μm.

The onset pressure for nanoimprinting into HSQ is fairly high, compared to other resists. This is, to some extent, in agreement with literature [66]. Observed pressure onset for spin-coated HSQ films is 100-150 bars, and a pressure over 200 bars usually yields an imprint. On the other hand, a pressure of 312 bar did not yield any imprint for spray-coated HSQ, whereas the pressure over 600 bars works most of the time. This suggests a possible difference between those HSQ films.

Both Zeonor plastic foils and Ni foils were used as a nanopattern master. There is a sizeable difference between depths achieved at the same pressure with Zeonor and Ni, and the highest depth achieved with Zeonor was only around 50 nm, below 30% of master depth. With a Ni master, the same pressure yields an imprint depth up to 65-80% of master.

There is an observable difference between the first and subsequent uses of the same Zeonor master, where the depth achieved during subsequent uses reduced, suggesting plastic deformation of the nanopattern in polymer. This is not a completely surprising effect considering the pressure.

Well defined nanopattern on non-planar substrates with different radii allows good assessment of pattern distortion. It was carried out, using measurement of pattern period as a function of the position on a spherical and a conical surface. This way the pattern-strain functions for spherical surfaces of 3 different radii were measured.

During this investigation, the boundary behind which the nanopattern was not replicated was observed. The same boundary was also found during the investigation of the used, plastically deformed Ni foils. The position on used foils is perfectly corresponding to the boundary on HSQ coated substrates.

An FE numerical model, devised to predict strain of 55 μm Ni foil hydrostatically pressed onto a spherical substrate with radii of 500, 1000, and 2000 μm is found to be in good agreement with experimental data. If the same model is used to calculate a contact pressure between aluminum substrate and nickel foil as a function of a position, it predicts both an existence and a position of the observed boundary with high precision.

Chapter 8: Conclusion and outlook

The goal of this work was to fabricate non-planar surfaces with nanostructured patterns that are suitable for injection molding tools and, to some extent, also the methods used. First, in order to facilitate de-molding of nanopatterned plastic parts, I needed to test if the previously established anti-adhesive monolayers, such as FDTS, are sufficiently stable and resistant also on surfaces of molding tools repeatedly exposed to molten polymer.

Using data, methods and results from chapters 2 and 3, one can conclude that an FDTS layer does not significantly alter the surface topography, and that there is a detectable fluorine concentration and a highly increased contact angle even after 500 molding cycles. This demonstrates the presence of the FDTS, thus showing that FDTS prevails well on mold surfaces of aluminum, titanium, and nickel.

Using the same results, the coating lifetime can be estimated with the assumption of a linear removal, as is presented in chapter 3. There, I show and compare four methods, two of which uses calculated surface energies, and two of which uses quantitative XPS data, either the absolute fluorine concentration or the ratio of fluorine to the primary metal. If I conservatively take the lowest estimate for each respective metal, I can rank them in the order of suitability for the FDTS coated mold substrate. They are, in descending order, aluminum, titanium and nickel.

Methods and metrics developed in chapters 2 and 3 are well suited to assess stability of FDTS on the surface of HSQ coated mold inserts, flat or micro- and nanostructured. As I show in chapter 5, spray-coated HSQ films can be used to reduce surface roughness of manufactured surfaces, planar or freeform. The peak-to-valley roughness was reduced 20 times on initially rougher sample and 10 times on initially less rough sample. This, together with the ability of HSQ to withstand IM, can facilitate much simpler, faster and cheaper manufacturing of molds, as they can be manufactured with less tight roughness tolerances, and consequently spray-coated with HSQ film to reduce roughness and an FDTS monolayer to facilitate de-molding. This way, one can fabricate for instance freeform optical and microoptical articles, where the roughness is critical. As the dimension of a spray-coated mold is not inherently limited, one can envision a promising outcome, large injection molded parts with excellent high-gloss surfaces.

A highly curved spherical PMMA surface may be nanostructured, as shown in the chapter 4, using a flexible soft stamp from PDMS and a hydrostatic pressure to facilitate the contact between the two. Structures as small as 420 nm have been successfully imprinted onto the spherical surface with a radius of 1 mm. In this chapter

we show sizeable pattern distortion (up to 14% of the base period) and the fact that the nominal, geometrically predicted 7.7% strain of the pattern is not distributed evenly on a spherical surface. There is also large difference between the use of thick and thin stamp. Nanostructured PMMA surfaces cannot be used as a tool for injection molding, but they can be used directly i.e. in microfluidics, or as a mold for polymer casting.

In chapter 6, we were able to develop a process for fabrication of imprinting masters from nickel and from Zeonor polymer, with an extremely precise and uniform period. Estimated mean period is 426.2±0.5 nm, the highest observed period difference for two directions of a cross-gratings is below 0.2% across whole master. Next we were able to develop a process to deposit up to 1.7µm thick HSQ films, and a set of dedicated embossing devices, last of which is capable to reach 1000 bar pressure, without failing.

In chapter 7, using the tools developed in chapter 6, we demonstrated a room-temperature imprinting in HSQ films deposited by spin- and spray-coating methods. One can see that the pressure which is sufficient for imprint in a spin-coated film (200 bar) is not sufficient for a spray-coated film, where 600 bar or more was needed. We have been able to show imprinting of 420 nm patterns on flat, conical, and spherical surfaces, with radii of 2000, 1000 and 500 µm. Such surfaces have been FDTS coated, and are directly usable as IM inserts. We also found a limit, a radial boundary, behind which the pattern is not imprinted, for each radius.

With a well defined pattern, we measured distribution of pattern distortion (strain) across the diameter and this experimental data have been compared with a specially developed finite element analysis based computational model and found to be in a good agreement. This model can now be used to predict pattern for other geometries. The model is also able to precisely predict contact pressure between the nickel stamp and spherical substrate, thus also the precise position of the abovementioned radial boundary for each diameter.

Moreover, if an FDTS coating, tested in chapters 2 and 3, is deposited after forming of the functional nanostructures in the mold, as we show in chapter 7, affordable, large, non-planar and nanopatterned surfaces would be available. As an example, I can name Fresnel-lens based solar cell concentrator with added nanostructures for antireflective properties, or large antifogging freeform plastic lenses for glasses, or small ones, for portable electronics or medical instruments.

Acknowledgments

The funding agencies and project numbers have been acknowledged on appropriate positions but I would like to thank all the actual people who helped me to accomplish this work and prepare this dissertation. In particlurar, to

Rafael Taboryski, my sole supervisor, for the guidance, motivation and support, with apology for my countless unannounced discussions in his office.

Henrik Pranov, CEO of Inmold Biosystems A/S, for financial and technical support in last few months of my research.

My Inmold co-workers, namely Guggi Kofod, Maria Matschuk and Swati Murthy, for their contribution.

Mads Rostgaard Sonne and Jesper Henri Hattel from DTU Mek for the finite element analysis computational model.

Henrik Chresten Pedersen, for unrestricted access to his interference lithography lab.

All the technicians from DTU Danchip and DTU Mek workshops, for speedy fabrication of Embossinators and accesories.

Cameron Smith, Eric Jensen and Lee MacKenzie Fischer for proofreading.

My colleagues and fellow students at DTU Nanotech:

Simone Tanzi, Emil Søgaard, Marco Matteucci, Peter Friis Østergaard, Simon Tylsgaard Larsen, Alicia Charlotte Johansson, Claus R. Poulsen, Nis Korsgaard Andersen, Alexander Bruun Christiansen, Jacqueline Trosborg, and Thomas Lehrmann Christiansen (who can fly 60mph, backwards, blindfolded and upside down. Without legs.) and others for the great help in last 3 years and for a lot of fun!

Ivanka Hajkova, my high school chemistry and math teacher, for making me who I am.

And, finally, last but not least, to my family, my wife Sylvia and my kids, Kristina and Tom, for their great attitude, patience and support.

List of publications

Publication within the frame of this dissertation

J. Cech *et al.*, High pressure HSQ nanoimprinting for injection molded non-planar functional surfaces, *manuscript in preparation*

J. Cech, H. Pranov, G. Kofod, M. Matschuk, S. Murthy, R Taboryski, Surface roughness reduction using spray-coated hydrogen silsesquioxane reflow. *Manuscript submitted to Appl. Surf. Sci., Jan 2013*

J. Cech, R. Taboryski, Stability of FDTS monolayer coating on aluminum injection molding tools, Appl. Surf. Sci. 259 (2012) 538-541.

J. Cech, R. Taboryski, Evaluation of stability of monolayer injection molding tools coating, Technical Proceedings of the 2012 NSTI Nanotechnology Conference and Expo, NSTI-Nanotech 2012. (2012) 679-682.

S. Tanzi, P.F. Ostergaard, M. Matteucci, T.L. Christiansen, J. Cech, R. Marie, R. Taboryski, Fabrication of combined-scale nano- and microfluidic polymer systems using a multilevel dry etching, electroplating and molding process, J Micromech Microengineering. 22 (2012).

Patent and Patent Applications

J. Cech, R. Taboryski, DTU Pat. 92871-12, Invention disclosure.

J. Cech, R. Taboryski, Silane based coating of aluminium mold, EP12158587.1 and US equivalent, filed 08 March 2012

Conference contributions

Poster: Cech, Jiri; Taboryski, Rafael J. Evaluation of stability of monolayer injection molding tools coating. Presented at: Nanotech 2012, Santa Clara, CA, USA (2012)

Poster: Cech, Jiri; Taboryski, Rafael J., Novel Ultrathin Molecular Coating for Injection Molding Tools. Presented at: PITTCON conference and expo 2012, Orlando, FL, USA (2012)

Poster: Christiansen, Alexander Bruun; Cech, Jiri; Kristensen, Anders; Taboryski, Rafael J. Fabrication of nanostructures on double-curved PMMA surfaces by thermal imprint with PDMS stamp. Presented at: The 55th International Conference on Electron, Ion, and Photon Beam Technology and Nanofabrication, Las Vegas, NV, USA (2011)

Poster: Cech, Jiri; Taboryski, Rafael J. Developing fabrication methods for nanostructured wafer-based precise polymer elements. Presented at: SPIE Optifab 2011, Rochester, NY, USA (2011)

Poster: Cech, Jiri; Christiansen, Alexander Bruun; Taboryski, Rafael J. Stamp deformation during nanopattern thermal imprinting on a double-curved substrate. Presented at: 37th International Conference on Micro and Nano Engineering, Berlin (2011)

Poster: Cech, Jiri; Taboryski, Rafael J. Towards Wafer Based Fabrication of Precise Optical Polymer Elements. Presented at: PITTCON conference and expo 2011, Atlanta, Georgia, USA (2011)

Publications outside frame of this dissertation

J. Cech, V. Swaminathan, P. Wijewarnasuriya, L.J. Currano, A. Kovalskiy, H. Jain, Fabrication of freestanding SWCNT networks for fast microbolometric focal plane array sensor, Proceedings of SPIE - The International Society for Optical Engineering. 7679 (2010).

A. Kovalskiy, J. Cech, C.L. Tan, W.R. Heffner, E. Miller, C.M. Waits, M. Dubey, W. Churaman, M. Vlcek, H. Jain, Chalcogenide glass thin film resists for grayscale lithography, Proceedings of SPIE - The International Society for Optical Engineering. 7273 (2009).

A. Kovalskiy, J. Cech, M. Vlcek, C.M. Waits, M. Dubey, W.R. Heffner, H. Jain, Chalcogenide glass e-beam and photoresists for ultrathin grayscale patterning, Journal of Micro/ Nanolithography, MEMS, and MOEMS. 8 (2009).

M. Vlcek, H. Pribylova, A. Kovalskiy, J. Cech, H. Jain, Evaluation of photosensitivity of As-S-Se thin layers for the fabrication of diffractive optical elements, Materials Science and Technology Conference and Exhibition 2009, MS and T'09. 1 (2009) 5-15.

R. Golovchak, O. Shpotyuk, A. Kovalskiy, A.C. Miller, J. Čech, H. Jain, Coordination defects in bismuth-modified arsenic selenide glasses: High-resolution x-ray photoelectron spectroscopy measurements, Physical Review B - Condensed Matter and Materials Physics. 77 (2008).

A. Ansaldo, M. Haluška, J. Čech, J.C. Meyer, D. Ricci, F. Gatti, E. Di Zitti, S. Cincotti, S. Roth, A study of the effect of different catalysts for the efficient CVD growth of carbon nanotubes on silicon substrates, Physica E: Low-Dimensional Systems and Nanostructures. 37 (2007) 6-10.

J. Čech, M. Kalbáč, S.A. Curran, D. Zhang, U. Dettlaff-Weglikowska, L. Dunsch, S. Yang, S. Roth, HRTEM and EELS investigation of functionalized carbon nanotubes, Physica E: Low-Dimensional Systems and Nanostructures. 37 (2007) 109-114.

U. Dettlaff-Weglikowska, V. Skakalova, J. Meyer, J. Cech, B.G. Mueller, S. Roth, Effect of fluorination on electrical properties of single walled carbon nanotubes and C60 peapods in networks, Current Applied Physics. 7 (2007) 42-46.

L. Hu, G. Gruner, D. Li, R.B. Kaner, J. Cech, Patternable transparent carbon nanotube films for electrochromic devices, J. Appl. Phys. 101 (2007).

M. Kalbáč, L. Kavan, M. Zukalová, S. Yang, J. Čech, S. Roth, L. Dunsch, The change of the state of an endoneural fullerene by encapsulation into SWCNT: A Raman spectroelectrochemical study of Dy3N@C80 peapods, Chemistry - A European Journal. 13 (2007) 8811-8817.

L. Kavan, I. Exnar, J. Cech, M. Graetzel, Enhancement of electrochemical activity of LiFePO4 (olivine) by amphiphilic ru-bipyridine complex anchored to a carbon nanotube, Chemistry of Materials. 19 (2007) 4716-4721.

A. Ansaldo, M. Haluška, J. Čech, D. Ricci, F. Gatti, E. Di Zitti, S. Cincotti, S. Roth, CVD synthesis of single wall carbon nanotubes devoted to ULSI electronic applications, Physica Status Solidi (B) Basic Research. 243 (2006) 3077-3081.

J. Čech, S.A. Curran, D. Zhang, J.L. Dewald, A. Avadhanula, M. Kandadai, S. Roth, Functionalization of multi-walled carbon nanotubes: Direct proof of sidewall thiolation, Physica Status Solidi (B) Basic Research. 243 (2006) 3221-3225.

S.A. Curran, J. Cech, D. Zhang, J.L. Dewald, A. Avadhanula, M. Kandadai, S. Roth, Thiolation of carbon nanotubes and sidewall functionalization, J. Mater. Res. 21 (2006) 1012-1018.

S.A. Curran, D. Zhang, W.T. Wondmagegn, A.V. Ellis, J. Cech, S. Roth, D.L. Carroll, Dynamic electrical properties of polymer-carbon nanotube composites: Enhancement through covalent bonding, J. Mater. Res. 21 (2006) 1071-1077.

M. Haluška, M. Hulman, B. Hornbostel, J. Čech, V. Skákalová, S. Roth, Synthesis of SWCNTs for C82 peapods by arc-discharge process using nonmagnetic catalysts, Physica Status Solidi (B) Basic Research. 243 (2006) 3042-3045.

J. Liu, D.L. Carroll, J. Cech, S. Roth, Single-walled carbon nanotubes synthesized by the pyrolysis of pyridine over catalysts, J. Mater. Res. 21 (2006) 2835-2840.

J.C. Meyer, J. Cech, B. Hornbostel, S. Roth, Progress in single-walled carbon nanotube based nanoelectromechanical systems, Physica Status Solidi (B) Basic Research. 243 (2006) 3500-3504.

D. Zhang, M.A. Kandadai, J. Cech, S. Roth, S.A. Curran, Poly(L-lactide) (PLLA)/multiwalled carbon nanotube (MWCNT) composite: Characterization and biocompatibility evaluation, J Phys Chem B. 110 (2006) 12910-12915.

U. Dettlaff-Weglikowska, J. Wang, J. Liang, B. Hornbostel, J. Cech, S. Roth, Purity evaluation of bulk single wall carbon nanotube materials, AIP Conference Proceedings. 786 (2005) 129-134.

P. Pötschke, A.R. Bhattacharyya, A. Janke, S. Pegel, A. Leonhardt, C. Täschner, M. Ritschel, S. Roth, B. Hornbostel, J. Cech, Melt mixing as method to disperse carbon nanotubes into thermoplastic polymers, Fullerenes Nanotubes and Carbon Nanostructures. 13 (2005) 211-224.

M. Vlček, S. Schroeter, J. Čech, T. Wágner, T. Glaser, Selective etching of chalcogenides and its application for fabrication of diffractive optical elements, J. Non Cryst. Solids. 326-327 (2003) 515-518.

References

[1] Y. Zhao, Z. Xie, H. Gu, C. Zhu, Z. Gu, Bio-inspired variable structural color materials, Chem. Soc. Rev. 41 (2012) 3297-3317.

[2] R.P. Feynman, There's Plenty of Room at the Bottom, Caltech Engineering and Science. 23:5 (1960) 22-36.

[3] X. Gao, X. Yan, X. Yao, L. Xu, K. Zhang, J. Zhang, B. Yang, L. Jiang, The dry-style antifogging properties of mosquito compound eyes and artificial analogues prepared by soft lithography, Adv Mater. 19 (2007) 2213. doi:10.1002/adma.200601946.

[4] L.J. Guo, Nanoimprint lithography: Methods and material requirements, Adv Mater. 19 (2007) 495-513. doi:10.1002/adma.200600882.

[5] W. Choi, O. Park, The fabrication of submicron patterns on curved substrates using a polydimethylsiloxane film mould, Nanotechnology. 15 (2004) 1767-1770. doi:10.1088/0957-4484/15/12/013.

[6] S. Hong, K. Han, K. Byeon, H. Lee, K. Choi, Fabrication of Sub-100 nm Sized Patterns on Curved Acryl Substrate Using a Flexible Stamp, Jpn. J. Appl. Phys. 47 (2008) 3699-3701. doi:10.1143/JJAP.47.3699.

[7] J. Chang, F. Cheng, C. Chao, Y. Weng, S. Yang, L. Wang, Direct imprinting using soft mold and gas pressure for large area and curved surfaces, J. Vac. Sci. Technol. A. 23 (2005) 1687-1690. doi:10.1116/1.2073447.

[8] Y.-. Weng, Y.-. Weng, S.-. Yang, J.-. Wong, A novel electromagnetism-assisted imprinting technology to replicate microstructures onto a large-area curved surface using a flexible magnetic mold, Polym. Adv. Technol. 20 (2009) 92-97. doi:10.1002/pat.1238.

[9] H. Liu, F. Chen, Q. Yang, P. Qu, S. He, X. Wang, J. Si, X. Hou, Fabrication of bioinspired omnidirectional and gapless microlens array for wide field-of-view detections, Appl. Phys. Lett. 100 (2012) 133701. doi:10.1063/1.3696019.

[10] B. Farshchian, A. Amirsadeghi, S.M. Hurst, J. Wu, J. Lee, S. Park, Soft UV-nanoimprint lithography on non-planar surfaces, Microelectron. Eng. 88 (2011) 3287-3292. doi:10.1016/j.mee.2011.07.010.

[11] B. Farshchian, S. Park, J. Choi, A. Amirsadeghi, J. Lee, S. Park, 3D nanomolding for lab-on-a-chip applications, Lab Chip. 12 (2012) 4764-4771. doi:10.1039/c2lc40572e.

[12] B. Farshchian, A. Amirsadeghi, S.M. Hurst, J. Kim, S. Park, Deformation behavior in 3D molding: experimental and simulation studies, J Micromech Microengineering. 22 (2012) 115027. doi:10.1088/0960-1317/22/11/115027.

[13] E. Cybulski, Plastic Conversion Processes, CRC Press, Boca Raton, FL, USA, (2009).

[14] S. Garidel, M. Zelsmann, N. Chaix, P. Voisin, J. Boussey, A. Beaurain, B. Pelissier, Improved release strategy for UV nanoimprint lithography, Journal of Vacuum Science & Technology B (Microelectronics and Nanometer Structures). 25 (2007) 2430-2434.

[15] M. Beck, M. Graczyk, I. Maximov, E.-. Sarwe, T.G.I. Ling, M. Keil, L. Montelius, Improving stamps for 10 nm level wafer scale nanoimprint lithography, Microelectronic Engineering. 61-62 (2002) 441-448.

[16] H. Li, X. Li, Q. Wang, H. Li, X. Li, Q. Wang, X. Li, The preparation of anti-sticking layers on stamps of nano-imprint lithography technology via vapor deposition process, Shanghai Jiaotong Daxue Xuebao/Journal of Shanghai Jiaotong University. 41 (2007) 1687-1689+1694.

[17] H. Schift, S. Saxer, S. Park, C. Padeste, U. Pieles, J. Gobrecht, Controlled co-evaporation of silanes for nanoimprint stamps, Nanotechnology. 16 (2005) S171-S175.

[18] Z.W. Zhong, X.C. Shan, Y.C. Yao, Investigation of Antiadhesive Coatings for Nanoimprinting Lithography, Mater. Manuf. Process. 25 (2010) 658-664. doi:10.1080/10426910903496888.

[19] P.F. Ostergaard, M. Matteucci, W. Reisner, R. Taboryski, DNA barcoding via counterstaining with AT/GC sensitive ligands in injection-molded all-polymer nanochannel devices, Analyst. (2013).

[20] J. Cech, R. Taboryski, Stability of FDTS monolayer coating on aluminum injection molding tools, Appl. Surf. Sci. 259 (2012) 538-541.

[21] J. Cech, R. Taboryski, Evaluation of stability of monolayer injection molding tools coating, Technical Proceedings of the 2012 NSTI Nanotechnology Conference and Expo, NSTI-Nanotech 2012. (2012) 679-682.

[22] M. Matschuk, N.B. Larsen, Injection molding of high aspect ratio sub-100 nm nanostructures, J Micromech Microengineering. 23 (2013) 025003. doi:10.1088/0960-1317/23/2/025003.

[23] A. Ladenburg, Annalen. 179 (1875) 143.

[24] Khotinski, Seregenkov, Ber. Dtsch. Chem. Ges. 41 (1908) 2946.

[25] J.A. Meads, F.S. Kipping, Organic derivatives of silicon Part XXIII On the so-called siliconic acids, Journal of the Chemical Society. 107 (1915) 459-468. doi:10.1039/ct9150700459.

[26] J.F. Brown, Polycondensation of Phenylsilanetriol, J. Am. Chem. Soc. 87 (1965) 4317. doi:10.1021/ja00947a017.

[27] J.F. Brown, L.H. Vogt, Polycondensation of Cyclohexylsilanetriol, J. Am. Chem. Soc. 87 (1965) 4313. doi:10.1021/ja00947a016.

[28] H.W. Ro, C.L. Soles, Silsesquioxanes in nanoscale patterning applications, Mater. Today. 14 (2011) 20-33. doi:10.1016/S1369-7021(11)70019-0.

[29] H.F. Yang, A.Z. Jin, Q. Luo, C.Z. Gu, Z. Cui, Y.F. Chen, Low-energy electron-beam lithography of hydrogen silsesquioxane, Microelectronic Engineering. 83 (2006). doi:10.1016/j.mee.2006.01.004.

[30] J.K.W. Yang, B. Cord, H. Duan, K.K. Berggren, J. Klingfus, S. Nam, K. Kim, M.J. Rooks, Understanding of hydrogen silsesquioxane electron resist for sub-5-nm-half-pitch lithography, J. Vac. Sci. Technol. B. 27 (2009) 2622-2627. doi:10.1116/1.3253652.

[31] W. Li, W. Wu, R.S. Williams, Combined helium ion beam and nanoimprint lithography attains 4 nm half-pitch dense patterns, J. Vac. Sci. Technol. B. 30 (2012) 06F304. doi:10.1116/1.4758768.

[32] L. Katgerman, F. Dom, Rapidly solidified aluminium alloys by meltspinning, Materials Science and Engineering A-Structural Materials Properties Microstructure and Processing. 375 (2004) 1212-1216. doi:10.1016/j.msea.2003.10.094.

[33] A. Bosch, R. Senden, G. Gubbels, B. van Venrooy, Optimisation strategy for aluminium optics using the meltspinning technology, 2011 (2009).

[34] A. Bosch, R. Senden, Melt spun aluminium for optical moulds, 2011 (2008).

[35] Kaleido Technology ApS, Tooling for wafer-level optics, 2011 (2011).

[36] B. Kobrin, T. Zhang, M.T. Grimes, K. Chong, M. Wanebo, J. Chinn, R. Nowak, An Improved Chemical Resistance and Mechanical Durability of Hydrophobic FDTS Coatings, International Mems Conference 2006. 34 (2006) 454-457. doi:10.1088/1742-6596/34/1/074.

[37] G.P.H. Gubbels, B.W.H. van Venrooy, A.J. Bosch, R. Senden, Rapidly solidified aluminium for optical applications - art. no. 70183A, Advanced Optical and Mechanical Technologies in Telescopes and Instrumentation, Pts 1-3. 7018 (2008) A183-A183. doi:10.1117/12.788766.

[38] M.B. Linford, C.E.D. Chidsey, Molecular layers covalently bonded to silicon surfaces, US Patent 5429708 (4 July 1995).

[39] B. Kobrin, J.D. Chinn, R. Nowak, R.C. Richard, Functional organic based vapor deposited coatings adhered by an oxide layer, US Patent Application 20070020392-A1 (25 January 2007).

[40] P.F. Reboa, K. Sand, Method for providing an anti-stiction coating on a metal surface, US Patent Application 20080074771-A1 (27 March 2008).

[41] J. Gao, W. Hu, M.N. Aryal, F. Buyukserin, X. Zhao, Compositions and methods of making non-spherical micro- and nano-particles, US Patent Application 20090196826-A1 (6 August 2009).

[42] E. Hoque, J.A. DeRose, P. Hoffmann, B. Bhushan, H.J. Mathieu, Alkylperfluorosilane Self-Assembled Monolayers on Aluminum: A Comparison with Alkylphosphonate Self-Assembled Monolayers, J. Phys. Chem. C. 111 (2007) 3956-3962. doi:10.1021/jp066101m.

[43] E. Hoque, J.A. DeRose, P. Hoffmann, H.J. Mathieu, Perfluorosilanized Aluminum Oxide Surfaces, Journal of Surface Analysis. 13 (2006) 178.

[44] J.F. Moulder, J. Chastain, Handbook of x-Ray Photoelectron Spectroscopy: A Reference Book of Standard Spectra for Identification and Interpretation of XPS Data, Physical Electronics Division, Perkin-Elmer Corp, 1992.

[45] S. Wu, J.Polym.Sci., Part C: Polym.Symp. (1971) 19.

[46] J.D. Bumgardner, R. Wiser, S.H. Elder, R. Jouett, Y. Yang, J.L. Ong, Contact angle, protein adsorption and osteoblast precursor cell attachment to chitosan coatings bonded to titanium, Journal of Biomaterials Science-Polymer Edition. 14 (2003) 1401-1409. doi:10.1163/156856203322599734.

[47] B. Kasemo, J. Lausmaa, Biomaterial and Implant Surfaces - on the Role of Cleanliness, Contamination, and Preparation Procedures, Journal of Biomedical Materials Research-Applied Biomaterials. 22 (1988) 145-158. doi:10.1002/jbm.820221307.

[48] M. Textor, C. Sittig, V. Frauchiger, S. Tosatti, D. Brunette, Properties and biological significance of natural oxide films on titanium and its alloys, in: P. Brunette, P. Tengvall, M. Textor and P. Thomsen

(Eds.), Titanium in Medicine: Material Science, Surface Science, Biological Responses and Medical Applications, Springer, Heidelberg, 2001, pp. 172-230.

[49] A.B. Christiansen, Master Thesis: Nanostructuring Double-Curved Polymer Surfaces, (Feb 2011).

[50] D. Qin, Y. Xia, G.M. Whitesides, Soft lithography for micro- and nanoscale patterning, Nature Protocols. 5 (2010) 491-502. doi:10.1038/nprot.2009.234.

[51] S. Tanzi, P.F. Ostergaard, M. Matteucci, T.L. Christiansen, J. Cech, R. Marie, R. Taboryski, Fabrication of combined-scale nano- and microfluidic polymer systems using a multilevel dry etching, electroplating and molding process, J Micromech Microengineering. 22 (2012) 115008. doi:10.1088/0960-1317/22/11/115008.

[52] K.O. Andresen, M. Hansen, M. Matschuk, S.T. Jepsen, H.S. Sorensen, P. Utko, D. Selmeczi, T.S. Hansen, N.B. Larsen, N. Rozlosnik, R. Taboryski, Injection molded chips with integrated conducting polymer electrodes for electroporation of cells, J Micromech Microengineering. 20 (2010) 055010. doi:10.1088/0960-1317/20/5/055010.

[53] C. Mitterer, F. Holler, D. Reitberger, E. Badisch, M. Stoiber, C. Lugmair, R. Nobauer, T. Muller, R. Kullmer, Industrial applications of PACVD hard coatings, Surf. Coat. Technol. 163 (2003) PII S0257-8972(02)00685-0. doi:10.1016/S0257-8972(02)00685-0.

[54] C.H. Hsu, D. Huang, W. Ho, L. Huang, C. Chang, Characteristics and performance of Cr2O3/CrN double-layered coatings deposited by cathodic arc plasma deposition, Materials Science and Engineering A-Structural Materials Properties Microstructure and Processing. 429 (2006). doi:10.1016/j.msea.2006.05.108.

[55] C.A.N. Estima, V.F. Neto, M.S.A. Oliveira, J. Gracio, Nanocrystalline Diamond Coating on Non-Planar Silicon Substrates, J. Nanosci. Nanotechnol. 12 (2012) 6700-6706. doi:10.1166/jnn.2012.4567.

[56] K. Bobzin, R. Nickel, N. Bagcivan, F.D. Manz, PVD - Coatings in Injection Molding Machines for Processing Optical Polymers, Plasma Processes and Polymers. 4 (2007). doi:10.1002/ppap.200730507.

[57] K. Bobzin, N. Bagcivan, M. Ewering, A. Gillner, S. Beckemper, C. Hartmann, S. Theiss, Nano Structured Physical Vapor Deposited Coatings by Means of Picosecond Laser Radiation, Journal of Nanoscience and Nanotechnology. 11 (2011). doi:10.1166/jnn.2011.3468.

[58] R. BANEY, M. ITOH, A. SAKAKIBARA, T. SUZUKI, Silsesquioxanes, Chem. Rev. 95 (1995) 1409-1430. doi:10.1021/cr00037a012.

[59] J. Zhao, I. Malik, T. Ryan, E. Ogawa, P. Ho, W. Shih, A. McKerrow, K. Taylor, Thermomechanical properties and moisture uptake characteristics of hydrogen silsesquioxane submicron films, Appl. Phys. Lett. 74 (1999) 944-946. doi:10.1063/1.123417.

[60] W. Volksen, R.D. Miller, G. Dubois, Low Dielectric Constant Materials, Chem. Rev. 110 (2010) 56-110. doi:10.1021/cr9002819.

[61] R. Kannan, H. Salacinski, P. Butler, A. Seifalian, Polyhedral oligomeric silsesquioxane nanocomposites: The next generation material for biomedical applications, Acc. Chem. Res. 38 (2005) 879-884. doi:10.1021/ar050055b.

[62] A.E. Grigorescu, C.W. Hagen, Resists for sub-20-nm electron beam lithography with a focus on HSQ: state of the art, Nanotechnology. 20 (2009) 292001. doi:10.1088/0957-4484/20/29/292001.

[63] J.K.W. Yang, B. Cord, H. Duan, K.K. Berggren, J. Klingfus, S. Nam, K. Kim, M.J. Rooks, Understanding of hydrogen silsesquioxane electron resist for sub-5-nm-half-pitch lithography, Journal of Vacuum Science & Technology B. 27 (2009). doi:10.1116/1.3253652.

[64] H.W. Ro, V. Popova, L. Chen, A.M. Forster, Y. Ding, K.J. Alvine, D.J. Krug, R.M. Laine, C.L. Soles, Cubic Silsesquioxanes as a Green, High-Performance Mold Material for Nanoimprint Lithography, Adv Mater. 23 (2011). doi:10.1002/adma.201001761.

[65] S. Matsui, Y. Igaku, H. Ishigaki, J. Fujita, M. Ishida, Y. Ochiai, M. Komuro, H. Hiroshima, Room temperature replication in spin on glass by nanoimprint technology, Journal of Vacuum Science & Technology B. 19 (2001). doi:10.1116/1.1417547.

[66] Y. Kang, M. Okada, S. Omoto, Y. Haruyama, K. Kanda, S. Matsui, Room temperature nanoimprinting using spin-coated hydrogen silsesquioxane with high boiling point solvent, J. Vac. Sci. Technol. B. 29 (2011) 06FC03. doi:10.1116/1.3653227.

[67] D. Morecroft, J.K.W. Yang, S. Schuster, K.K. Berggren, Q. Xia, W. Wu, R.S. Williams, Sub-15 nm nanoimprint molds and pattern transfer, J. Vac. Sci. Technol. B. 27 (2009) 2837-2840. doi:10.1116/1.3264670.

[68] G. Jung, Z. Li, W. Wu, Y. Chen, D. Olynick, S. Wang, W. Tong, R. Williams, Vapor-phase self-assembled monolayer for improved mold release in nanoimprint lithography, Langmuir. 21 (2005) 1158-1161. doi:10.1021/la0476938.

[69] W. Zhou, J. Zhang, Y. Liu, X. Li, X. Niu, Z. Song, G. Min, Y. Wan, L. Shi, S. Feng, Characterization of anti-adhesive self-assembled monolayer for nanoimprint lithography, Appl. Surf. Sci. 255 (2008) 2885-2889. doi:10.1016/j.apsusc.2008.08.045.

[70] N.B. Larsen, S.B. Nyrup, H. Pranov, Transferring heat sensitive material on polymer. US Patent 7,985,366 B2, Issue date: 26 Jul 2011.

[71] J. Cech, R. Taboryski, Stability of FDTS monolayer coating on aluminum injection molding tools, Appl. Surf. Sci. 259 (2012) 538-541. doi:10.1016/j.apsusc.2012.07.078.

[72] V. Miikkulainen, M. Suvanto, T.A. Pakkanen, S. Siitonen, P. Karvinen, M. Kuittinen, H. Kisonen, Thin films of MoN, WN, and perfluorinated silane deposited from dimethylamido precursors as contamination resistant coatings on micro-injection mold inserts, Surf. Coat. Technol. 202 (2008). doi:10.1016/j.surfcoat.2008.05.007.

[73] G. Kofod, Reflow polishing of injection molds, Workshop “Steel Polishing“, Aachen, Germany, November 19-20, (2012).

[74] H. Pranov, G. Kofod, S. Murthy, Mold Repair Test, Inmold Biosystems company records (2012).

[75] C. Yang, W. Chen, The structures and properties of hydrogen silsesquioxane (HSQ) films produced by thermal curing, J. Mater. Chem. 12 (2002) 1138-1141. doi:10.1039/b107697n.

[76] E.D. Palik, Handbook of Optical Constants of Solids, Elsevier Science & Tech, (1985).

[77] P. JOHNSON, R. CHRISTY, Optical Constants of Noble Metals, Phys. Rev. B. 6 (1972) 4370-4379. doi:10.1103/PhysRevB.6.4370.

[78] G. Pribil, B. Johs, N. Ianno, Dielectric function of thin metal films by combined in situ transmission ellipsometry and intensity measurements, Thin Solid Films. 455 (2004) 443-449. doi:10.1016/j.tsf.2003.11.243.

[79] M. Novotny, J. Bulir, J. Lancok, P. Pokorny, M. Bodnar, In-situ monitoring of the growth of nanostructured aluminum thin film, J. Nanophotonics. 5 (2011) 051503. doi:10.1117/1.3543816.

[80] P.S. Kuo, Cylinder Pressure in a Spark-Ignition Engine: A Computational Model, J. Undergrad. Sci. 3 (Fall 1996) 141-154.

[81] M. Heap, Compacted Graphite Iron, Engine Technology International. 2 (1999) 70.

[82] K. Vollrath, Motorguss – Werden die Werkstoffkarten neu gemischt? Kontruiren + Giessen. 28 (2003) 25-27.

[83] C. Mohrdieck, Innovations in Iron Casting for Automotive Applications , 5th CGI Machining Workshop. (Sept 2003).

[84] NATO, Thermodynamic Interior Ballistic Model with Global Parameters, NATO Standardization Agreements, STANAG 7367, 2nd ed., North Atlantic Treaty Organization, 2000, May 22.

[85] Thorlabs, Pinhole diagram, http://www.thorlabs.com/images/TabImages/Pinhole_raydiagram.gif

[86] Microchemicals, Optical Parameters of Photoresist, http://www.microchemicals.eu/technical_information/photoresists_optical_parameters.pdf

[87] SCHOTT Technical Glass Solutions GmbH, SCHOTT BOROFLOAT 33 http://psec.uchicago.edu/glass/borofloat_33_e.pdf

[88] Scuba Cylinder Servicing and High Pressure Valve Support Pages, http://www.scubaengineer.com/tank_servicingx.htm

[89] Offshore compressed air cylinder explosion report, http://www.scubaengineer.com/documents/j_botle_bang.pdf

[90] N.C. Henderson, W.E. Berry, R.J. Eiber, D.W. Frink, FINAL REPORT ON PHASE I INVESTIGATION OF SCUBA CYLINDER CORROSION TO U.S. NAVY SUPERVISOR OF DIVING NAVAL SHIP SYSTEMS COMMAND, http://www.dtic.mil/cgi-bin/GetTRDoc?AD=AD0712815 (September 1970).

[91] BoltDepot, Bolt Grades and Charts http://www.boltdepot.com/fastener-information/Materials-and-Grades/Bolt-Grade-Chart.aspx

[92] Calculating Tie-Rod Stretch, Product Catalog: Fluid Power & Automation Control, 47th Edition, Catalog 365, Womack Machine Supply Company, DALLAS, TX, page 486.

[93] D. Winston, B.M. Cord, B. Ming, D.C. Bell, W.F. DiNatale, L.A. Stern, A.E. Vladar, M.T. Postek, M.K. Mondol, J.K.W. Yang, K.K. Berggren, Scanning-helium-ion-beam lithography with hydrogen silsesquioxane resist, J. Vac. Sci. Technol. B. 27 (2009) 2702-2706. doi:10.1116/1.3250204.

[94] S. Matsui, Y. Igaku, H. Ishigaki, J. Fujita, M. Ishida, Y. Ochiai, H. Namatsu, M. Komuro, Room-temperature nanoimprint and nanotransfer printing using hydrogen silsequioxane, J. Vac. Sci. Technol. B. 21 (2003) 688-692. doi:10.1116/1.1545754.

[95] Y. Igaku, S. Matsui, H. Ishigaki, J. Fujita, M. Ishida, Y. Ochiai, H. Namatsu, M. Komuro, H. Hiroshima, Room temperature nanoimprint technology using hydrogen silsequioxane (HSQ), Jpn. J. Appl. Phys. Part 1 - Regul. Pap. Short Notes Rev. Pap. 41 (2002) 4198-4202. doi:10.1143/JJAP.41.4198.

[96] J. Sung, M. Lee, S. Lee, S. Park, E. Lee, B. O, Realization of various sub-micron metal patterns using room temperature nanoimprint lithography, Thin Solid Films. 515 (2007) 5153-5157. doi:10.1016/j.tsf.2006.10.078.

[97] K. Nakamatsu, S. Matsui, Nanoimprinting using liquid-phase hydrogen silsesquioxane, Japanese Journal of Applied Physics Part 2-Letters & Express Letters. 45 (2006). doi:10.1143/JJAP.45.L546.

[98] K. Yang, S. Oh, H. Park, H. Lee, Novel fabrication technique for nanoscale hydrogen silsesquioxane structures using a direct printing technique, J. Vac. Sci. Technol. B. 29 (2011) 051602. doi:10.1116/1.3628585.

[99] Atlas of Stress-Strain Curves, 2nd Ed., ASM International, (2002), 816 pages.

[100] D. H. Buckley and R. L. Johnson, Friction and wear of Nickel-Aluminum alloys and some sulfur-modified steels in vacuum to 10e-9 millimeter of mercury, NASA Technical note, (May 1964).

Appendix A: Supplementary data

Supplementary figures S1, S2 and S3 with unprocessed CA data associated with **Chapter 2: Stability of FDTS monolayer coating on aluminum injection molding tools**.

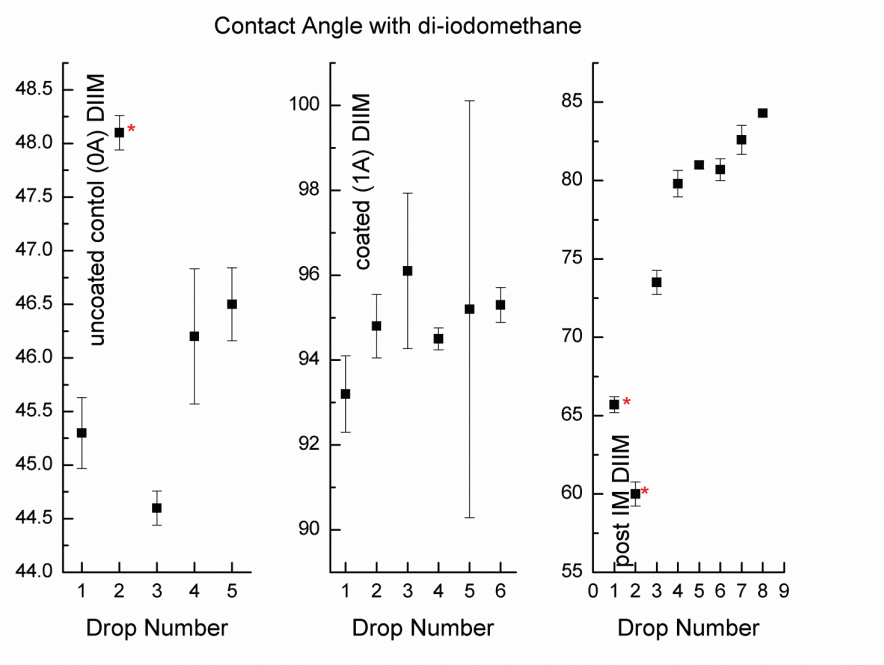

***Figure S1**. Raw results of CA measurement with multiple drops of diiodomethane for each sample treatment. Values marked with star are omitted for further calculation.*

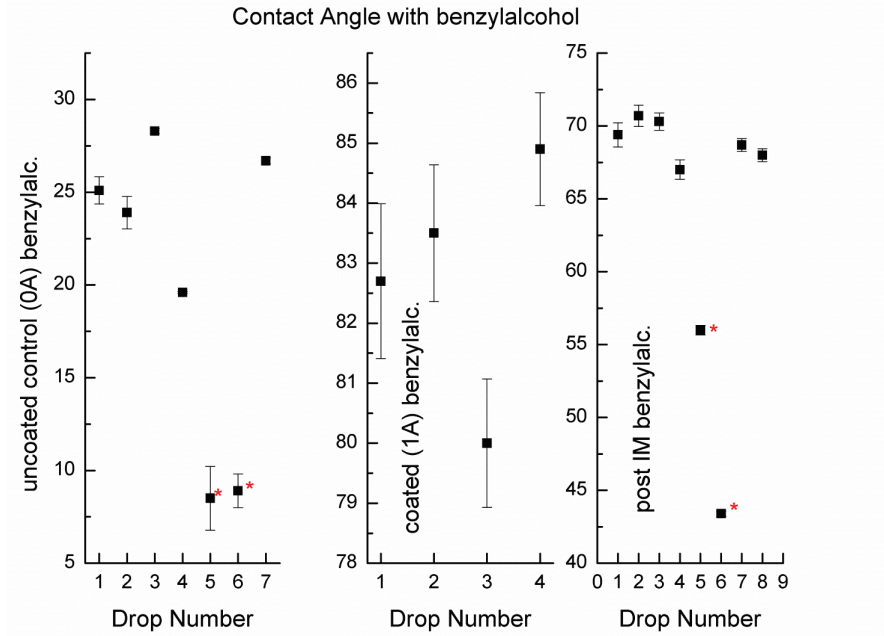

***Figure S2**. Raw results of CA measurement with multiple drops of benzylalcohol for each sample treatment. Values marked with star are omitted for further calculation.*

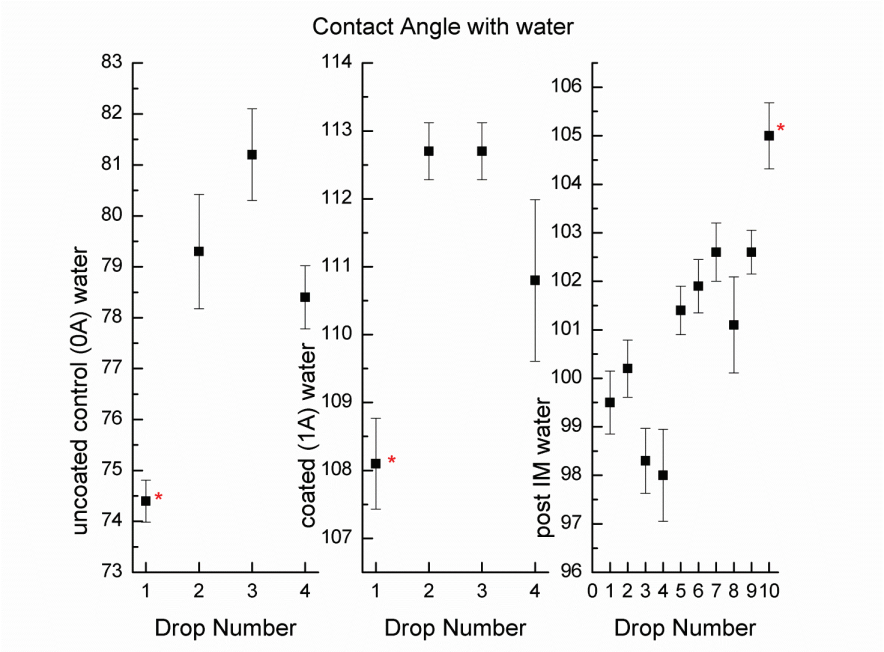

***Figure S3**. Raw results of CA measurement with multiple drops of water for each sample treatment. Values marked with star are omitted for further calculation.*

Supplementary figures S4-S9 with unprocessed CA data associated with **Chapter 3: Stability of FDTS monolayer coating on Ni and Ti injection molding tools**.

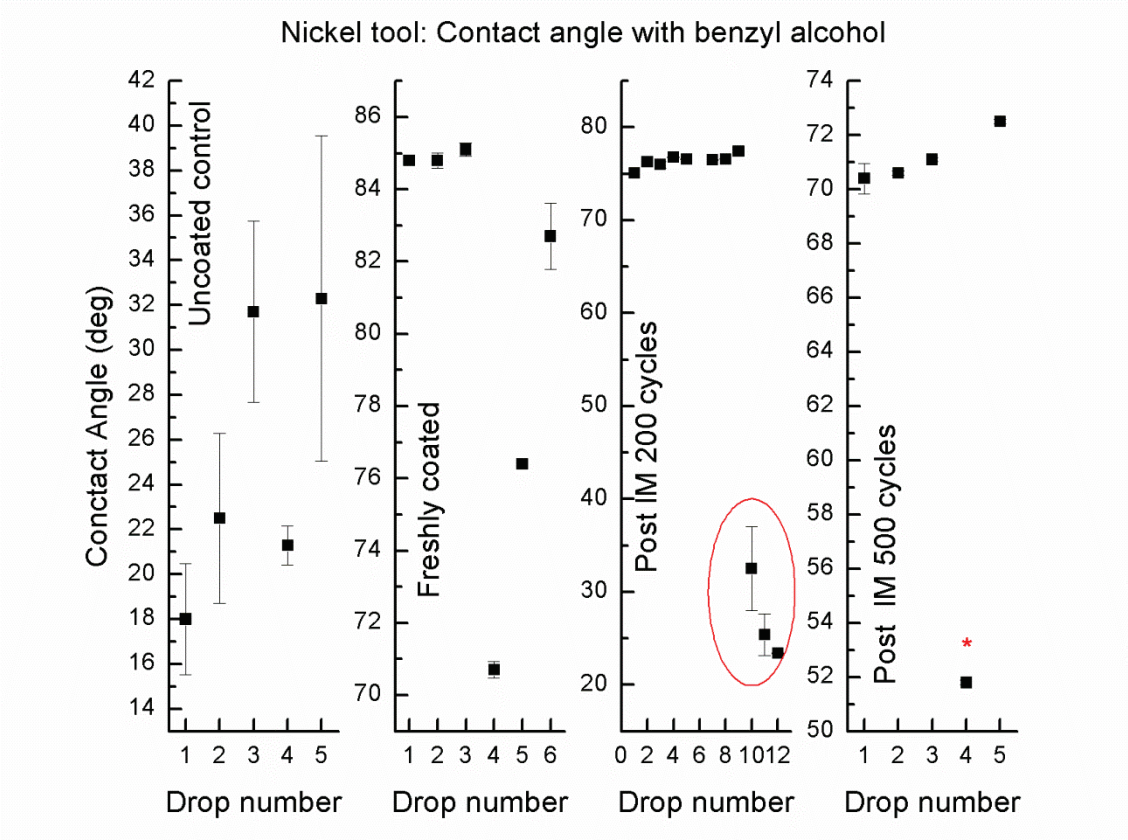

***Figure S4**. Contact angle measurement results for a nickel IM surface and BA, as a function of a sample treatment, left to right, for an uncoated sample, for sample freshly coated with FDTS, for sample after 200 injection molding 200 with cold (20°C) mold and after additional 300 cycles with heated mold (100°C), therefore total of 500 cycles. Values marked with star are omitted for further calculation. Values in red oval are not representative, they are measured inside a small surface region affected by so called diesel effect as discussed in chapter text.*

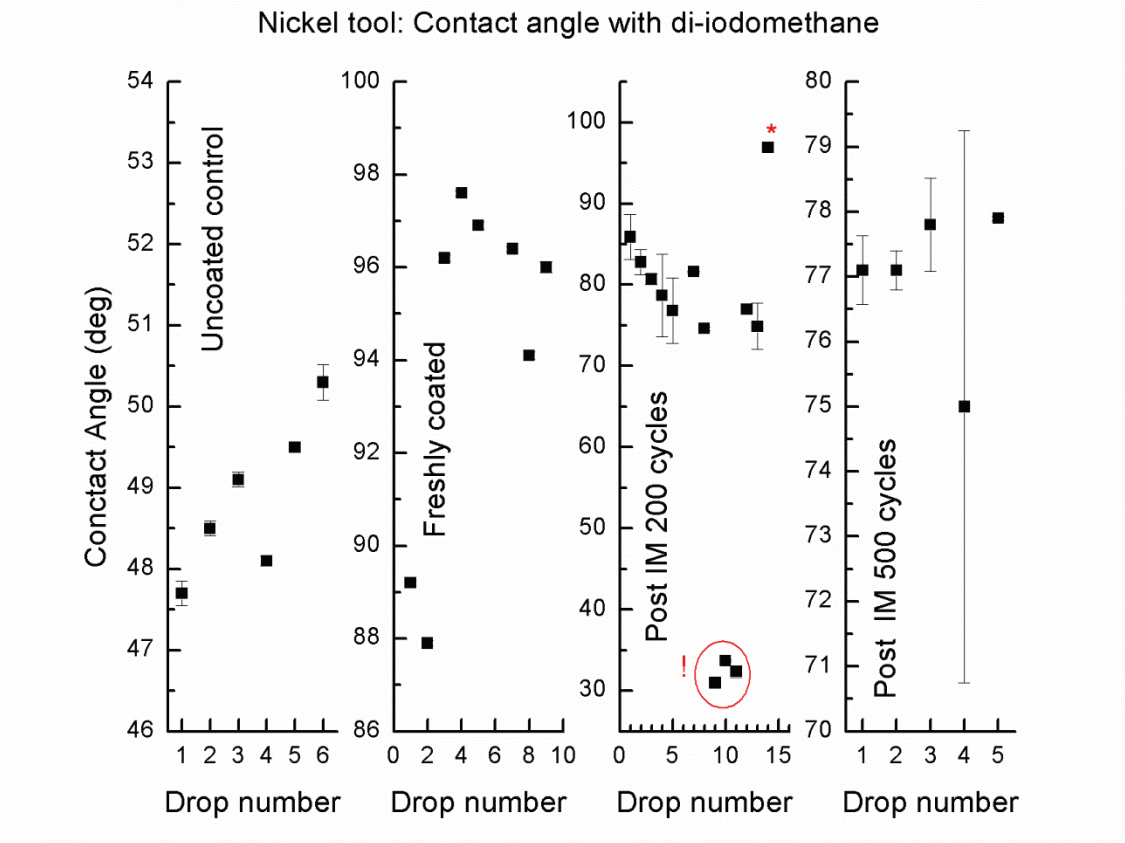

***Figure S5**. Raw contact angle measurement results for a nickel IM surface and di-iodomethane, as a function of a sample treatment, left to right, for an uncoated sample, for sample freshly coated with FDTS, for sample after 200 injection molding 200 with cold (20°C) mold and after additional 300 cycles with heated mold (100°C), therefore total of 500 cycles. Values marked with star are omitted for further calculation. Values in red oval are not representative, they are measured inside a small surface region affected by so called diesel effect as discussed in chapter text.*

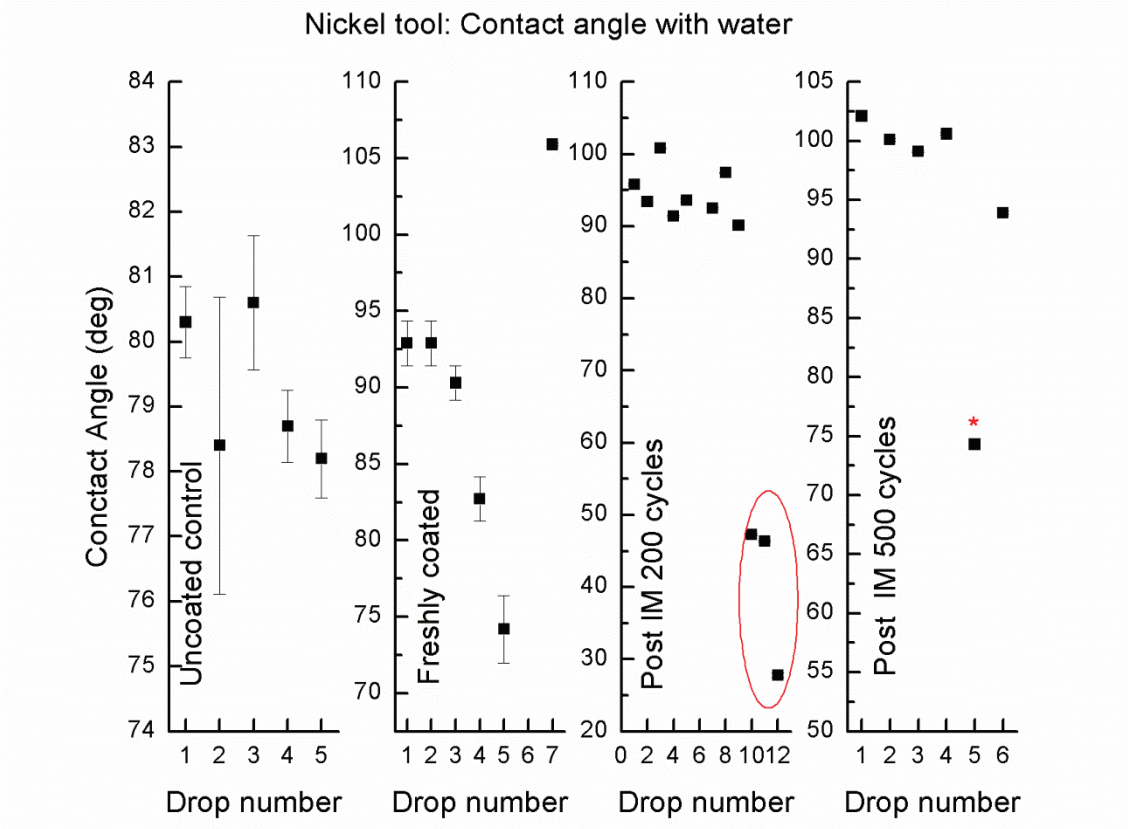

***Figure S6**. Raw contact angle measurement results for a nickel IM surface and water, as a function of a sample treatment, left to right, for an uncoated sample, for sample freshly coated with FDTS, for sample after 200 injection molding 200 with cold (20°C) mold and after additional 300 cycles with heated mold (100°C), therefore total of 500 cycles. Values marked with star are omitted for further calculation. Values in red oval are not representative, they are measured inside a small surface region affected by so called diesel effect as discussed in chapter text.*

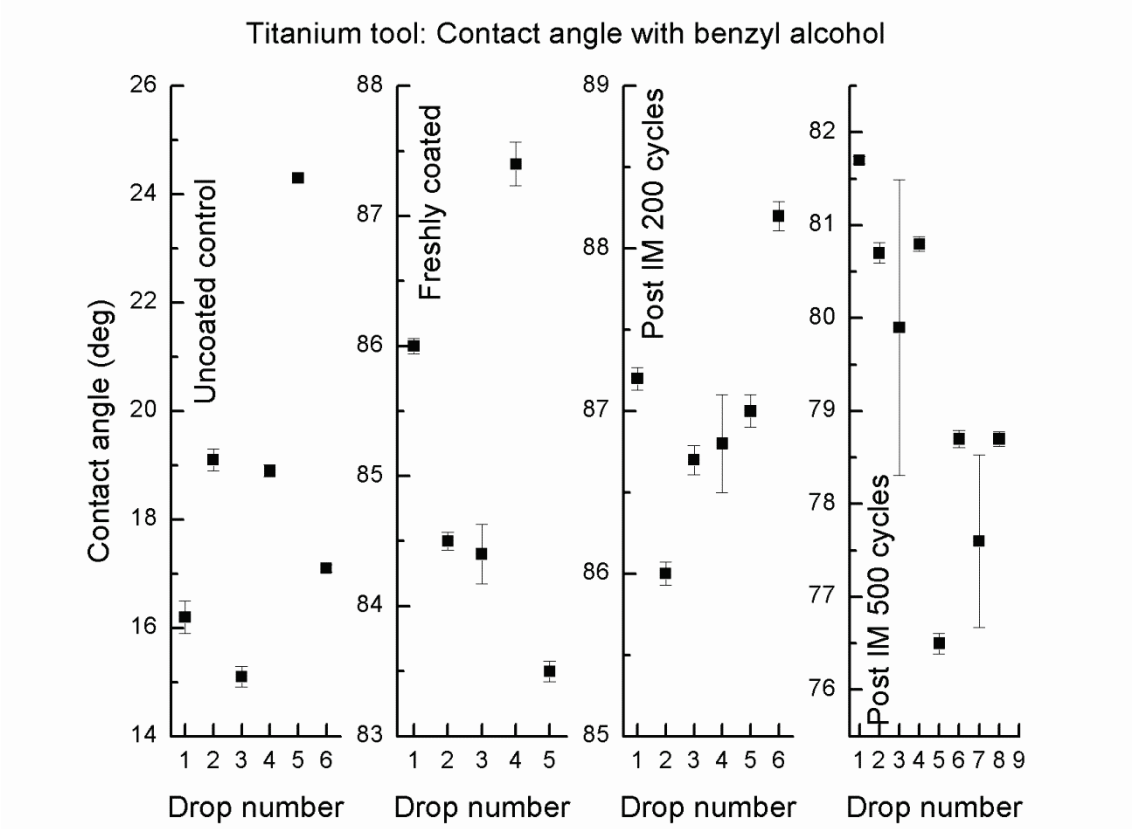

***Figure S7**. Raw contact angle measurement results for a titanium IM tool surface and benzyl alcohol, as a function of a sample treatment, left to right, for an uncoated sample, for sample freshly coated with FDTS, for sample after 200 injection molding 200 with cold (20°C) mold and after additional 300 cycles with heated mold (100°C), therefore total of 500 cycles.*

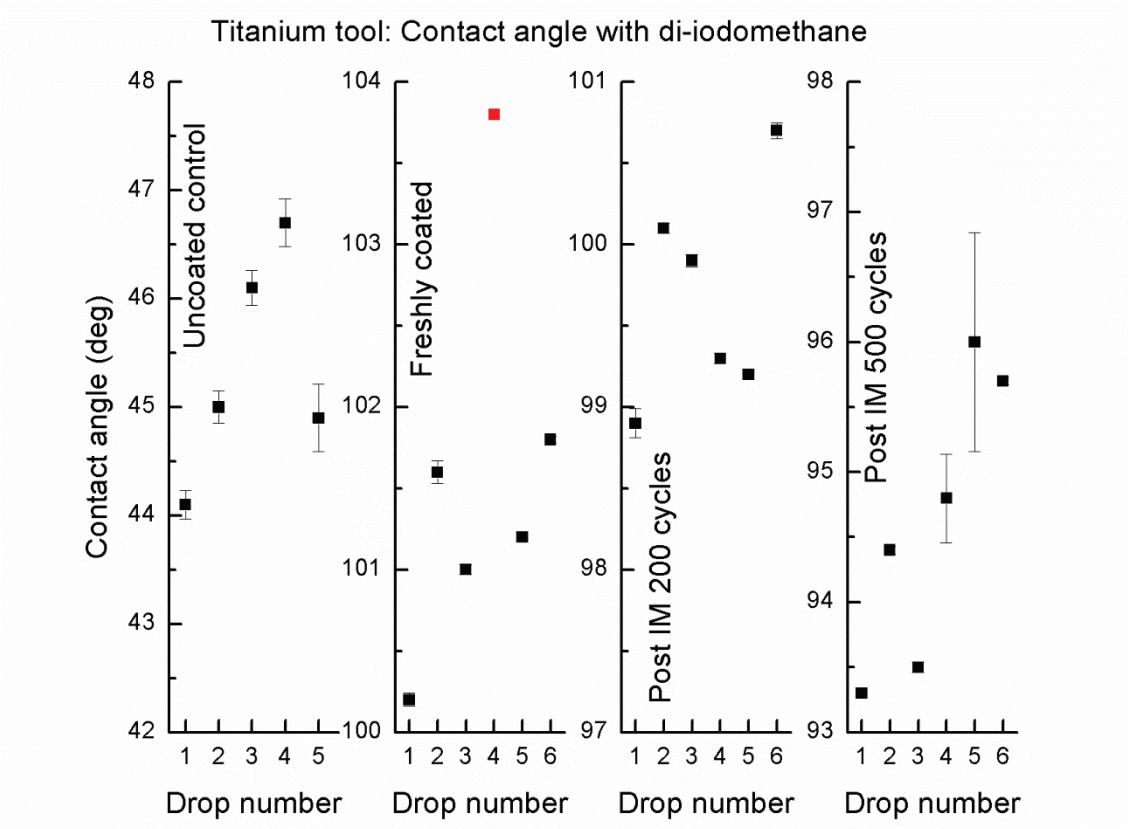

***Figure S8**. Raw contact angle measurement results for a titanium IM tool surface and di-iodomethane, as a function of a sample treatment, left to right, for an uncoated sample, for sample freshly coated with FDTS, for sample after 200 injection molding 200 with cold (20°C) mold and after additional 300 cycles with heated mold (100°C), therefore total of 500 cycles. Value plotted in red is omitted for further calculation.*

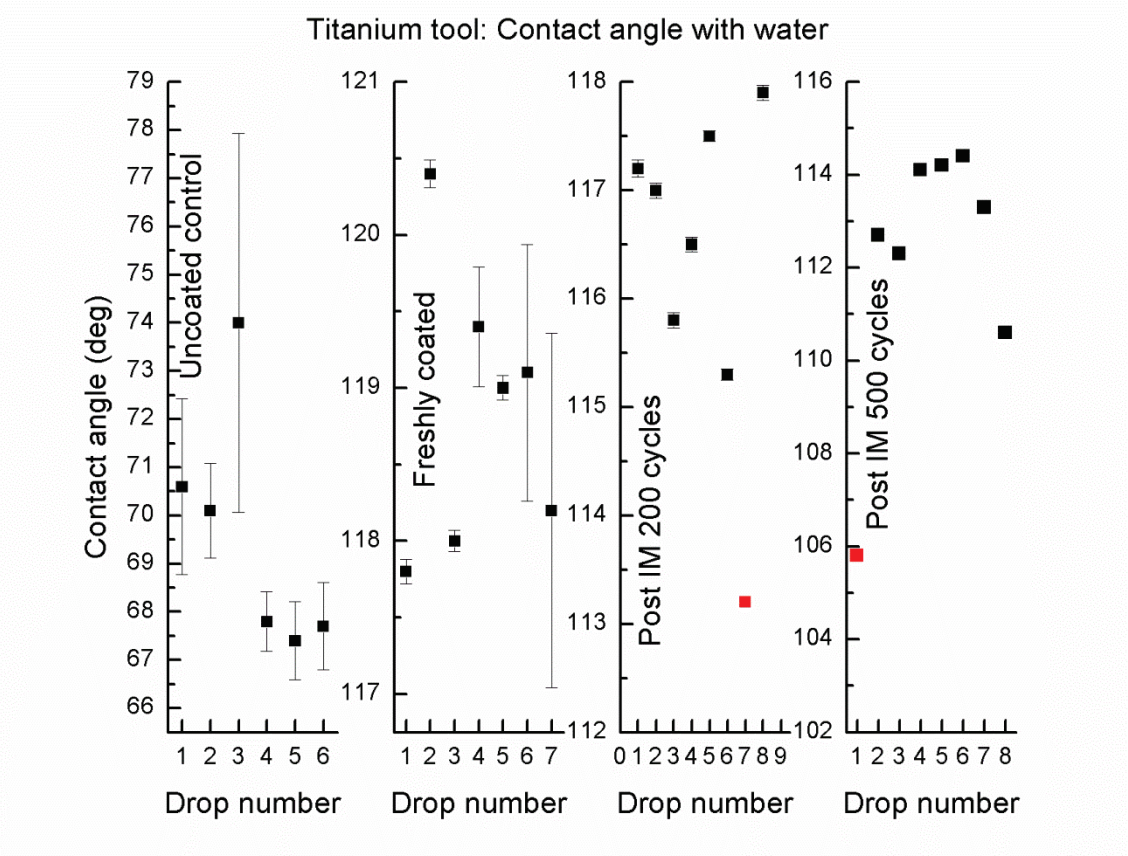

***Figure S9**. Raw contact angle measurement results for a titanium IM tool surface and water, as a function of a sample treatment, left to right, for an uncoated sample, for sample freshly coated with FDTS, for sample after 200 injection molding 200 with cold (20°C) mold and after additional 300 cycles with heated mold (100°C), therefore total of 500 cycles. Values plotted in red are omitted for further calculation.*

Supplementary table S10, with roughness data associated with **Chapter X: Surface roughness reduction using spray-coated hydrogen silsesquioxane reflow**

	clean Si	SD (N=5)	post-sputtering Si	SD (N=4)
S_{RMS} [nm]	2.41	0.29	1.96	0.20
S_a [nm]	1.91	0.26	1.57	0.15
S_{PV} [nm]	16.00	2.30	13.60	1.60

Supplementary table S10. *Roughness parameters and their standard deviations (SD) measured on a silicon wafer before and after sputtering of the reflective Au/Pd film together with actual samples measured using VSI method. Roughness change is very low, as expected for sputtering, which is usually considered a conformal coating process, thus the effect of this coating on roughness can be neglected.*

.

Appendix B: Technical drawings

Technical drawings of the Embossinators 4, 3, and 2.

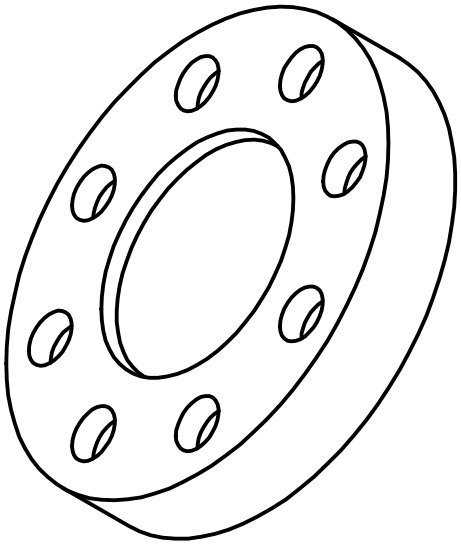

A-A (1 : 2)

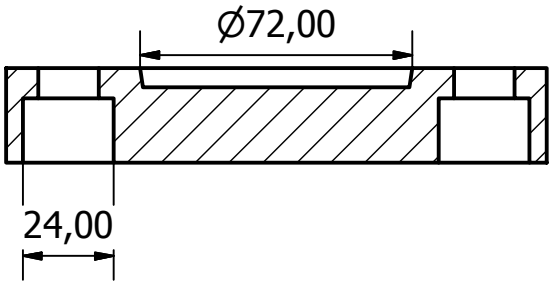

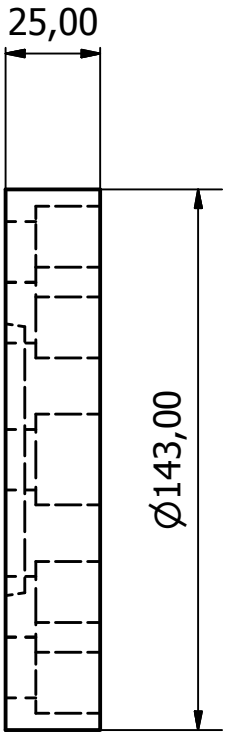

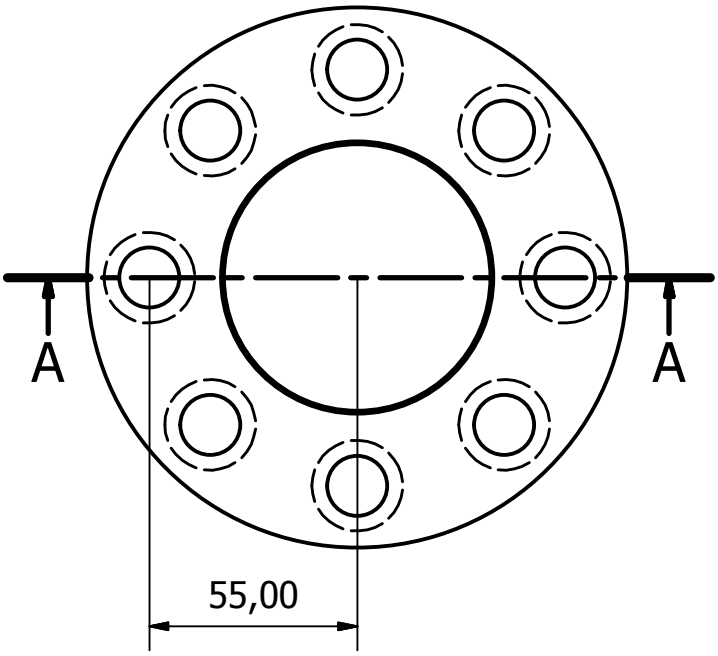

Designed by	Checked by	Approved by	Date		Date	
Jiri Cech					3/8/2013	

DTU Nanotech	Embossinator 4: bottom		
	Steel	Edition	Sheet 1 / 1

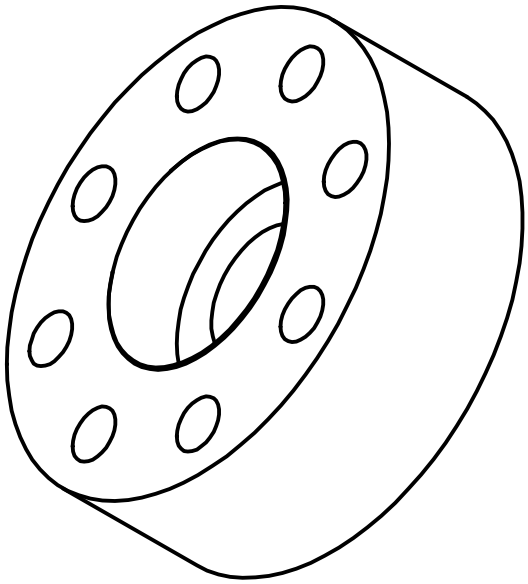

B (5 : 1)

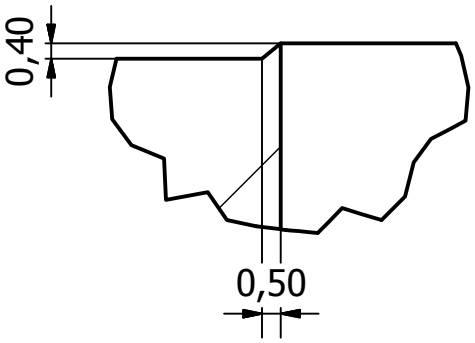

A-A (1 : 2)

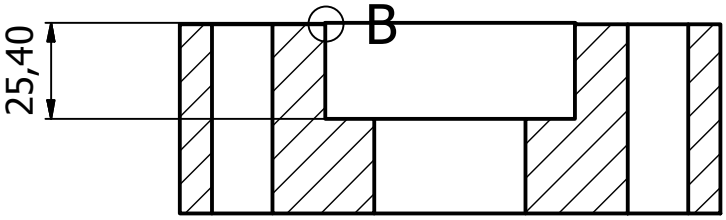

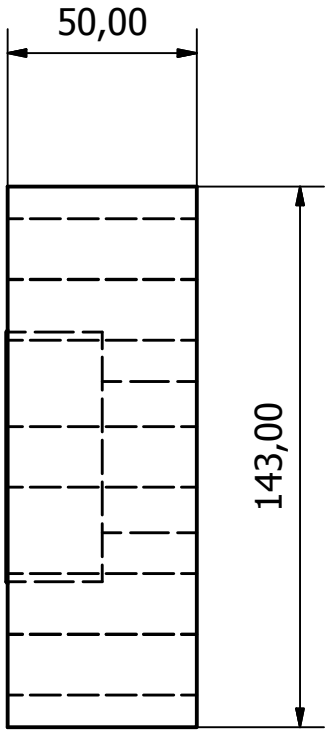

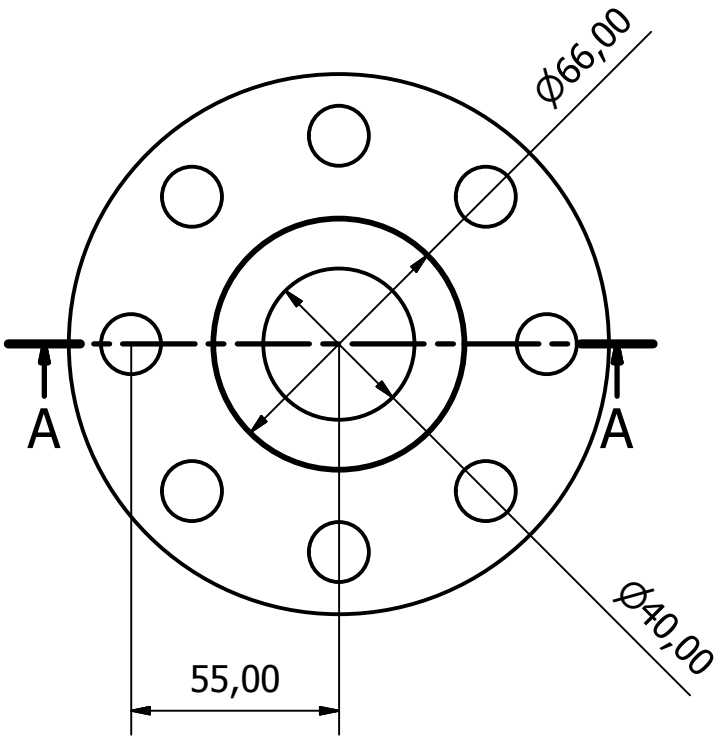

Designed by	Checked by	Approved by	Date		Date	
Jiri Cech					3/8/2013	

DTU Nanotech	Embossinator 4: top		
	steel	Edition	Sheet 1 / 1

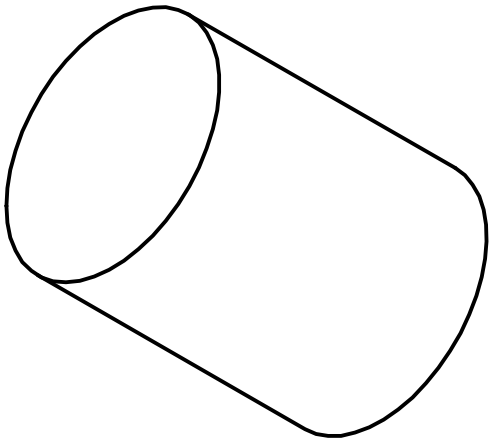

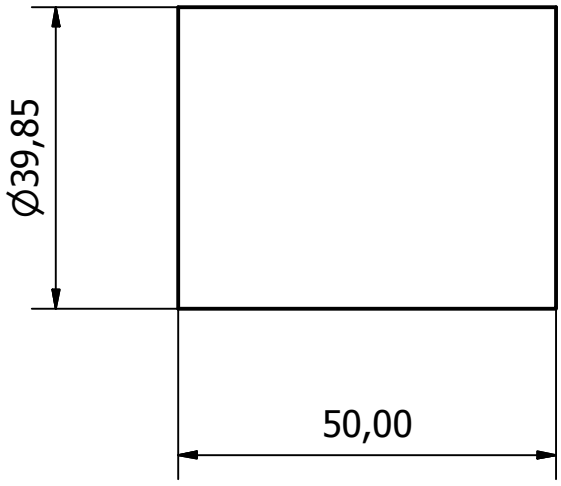

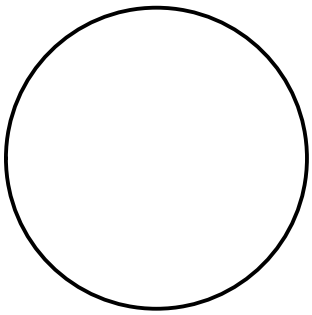

Designed by	Checked by	Approved by	Date		Date	
Jiri Cech					3/8/2013	

DTU Nanotech	Embossinator 4: piston		
	steel	Edition	Sheet 1 / 1

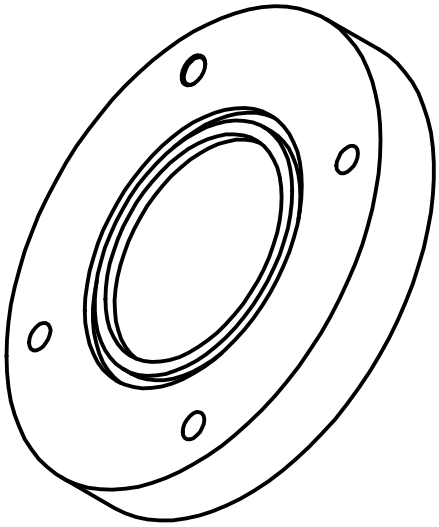

A-A (1 : 2)

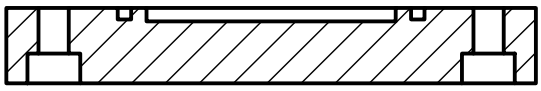

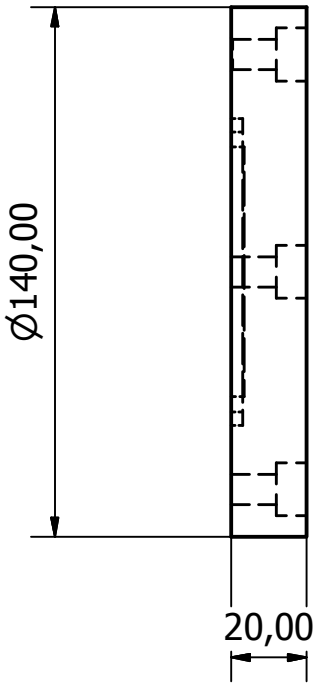

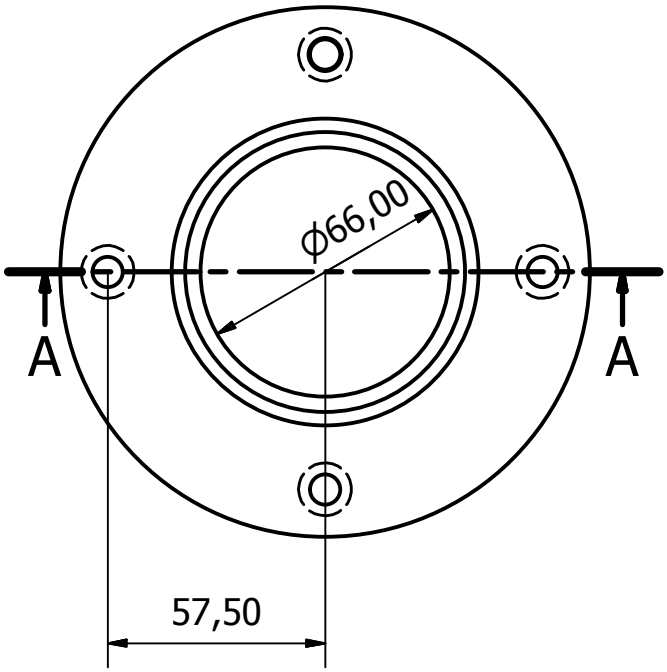

Designed by	Checked by	Approved by	Date		Date	
Jiri Cech					3/8/2013	

DTU Nanotech	Embossinator 3: bottom		
	Aluminum	Edition	Sheet 1 / 1

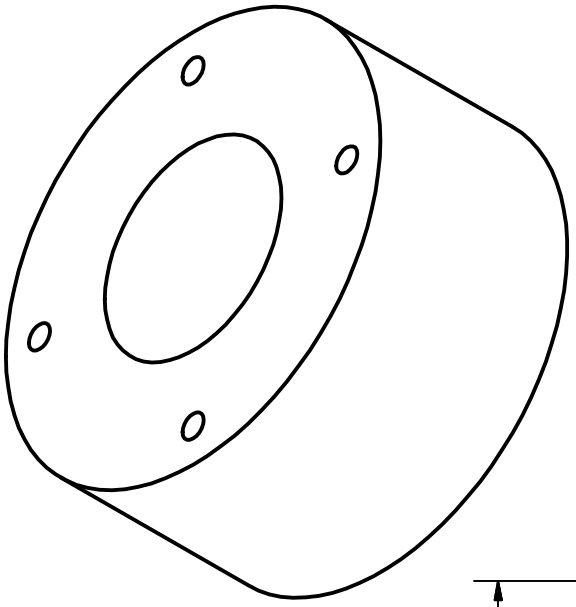

A-A (1 : 2)

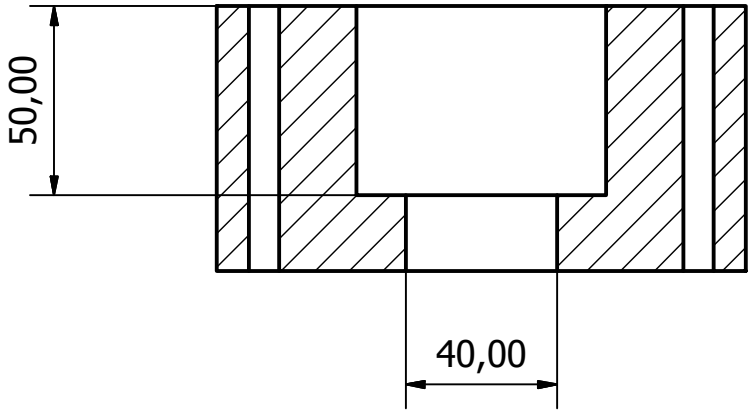

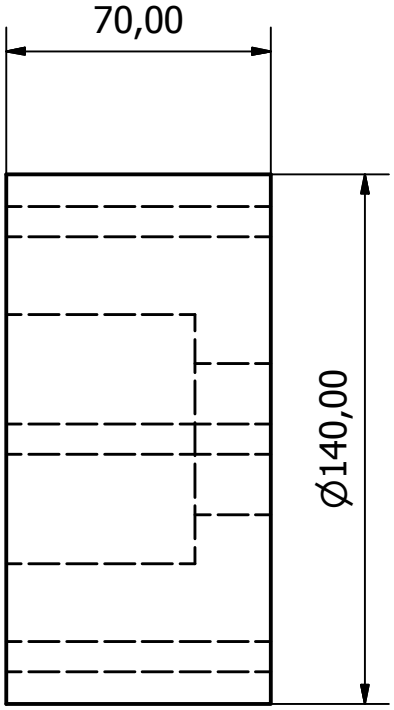

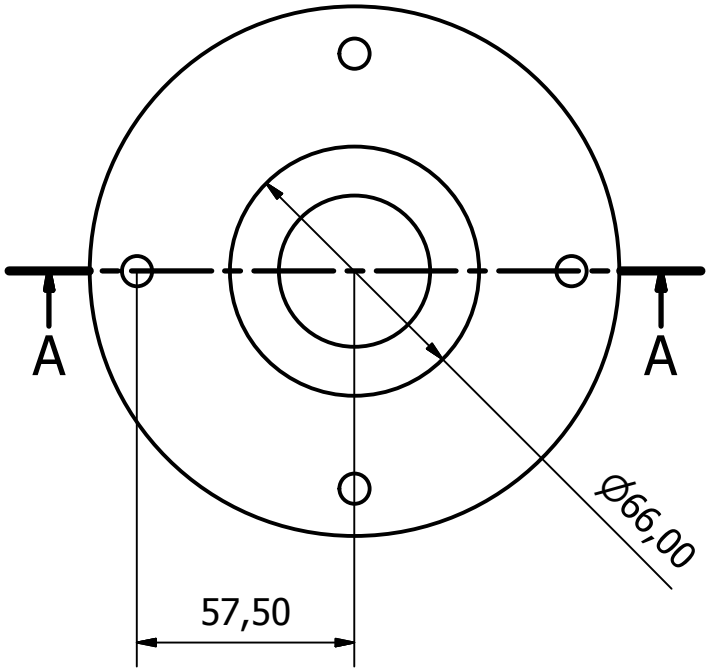

Designed by	Checked by	Approved by	Date		Date	
Jiri Cech					3/8/2013	

DTU Nanotech	Embossinator 3: top		
	Aluminum	Edition	Sheet 1 / 1

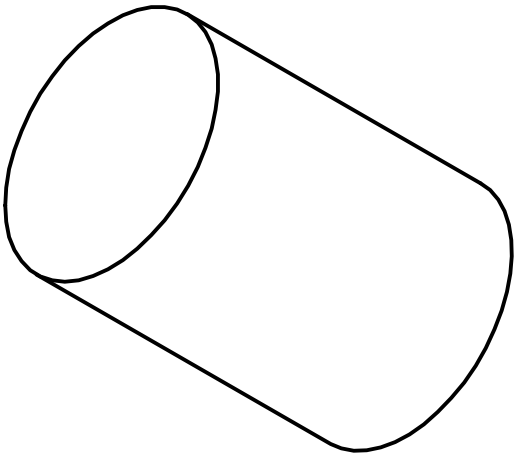

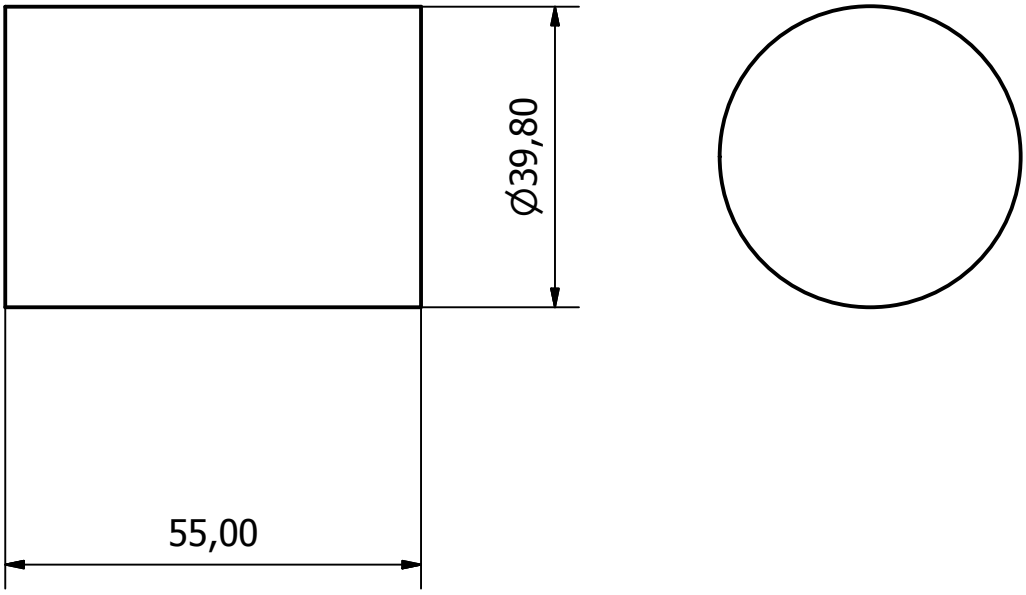

Designed by	Checked by	Approved by	Date		Date	
Jiri Cech					3/8/2013	

DTU Nanotech	Embossinator 3: piston		
	Aluminum	Edition	Sheet 1 / 1

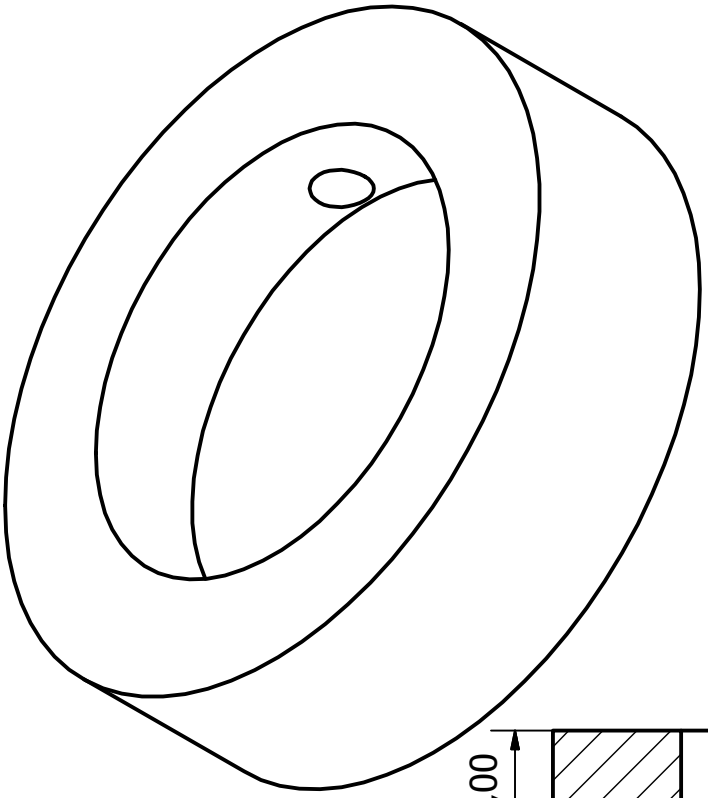

A-A (1 : 1)

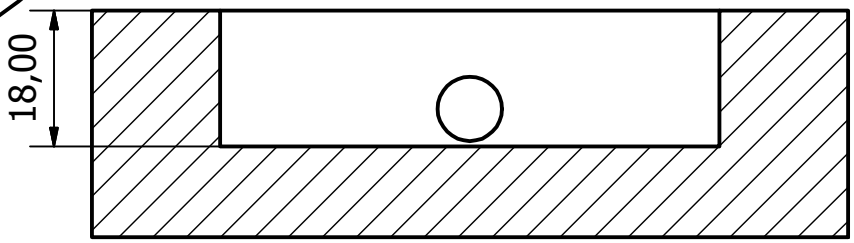

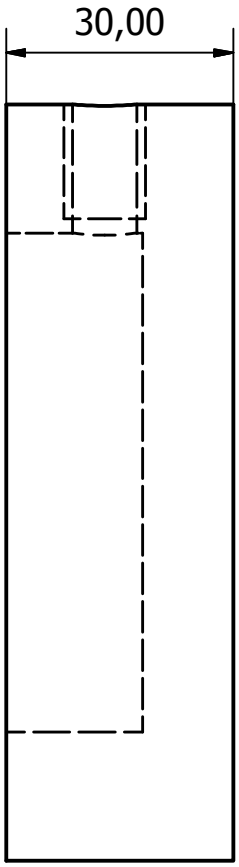

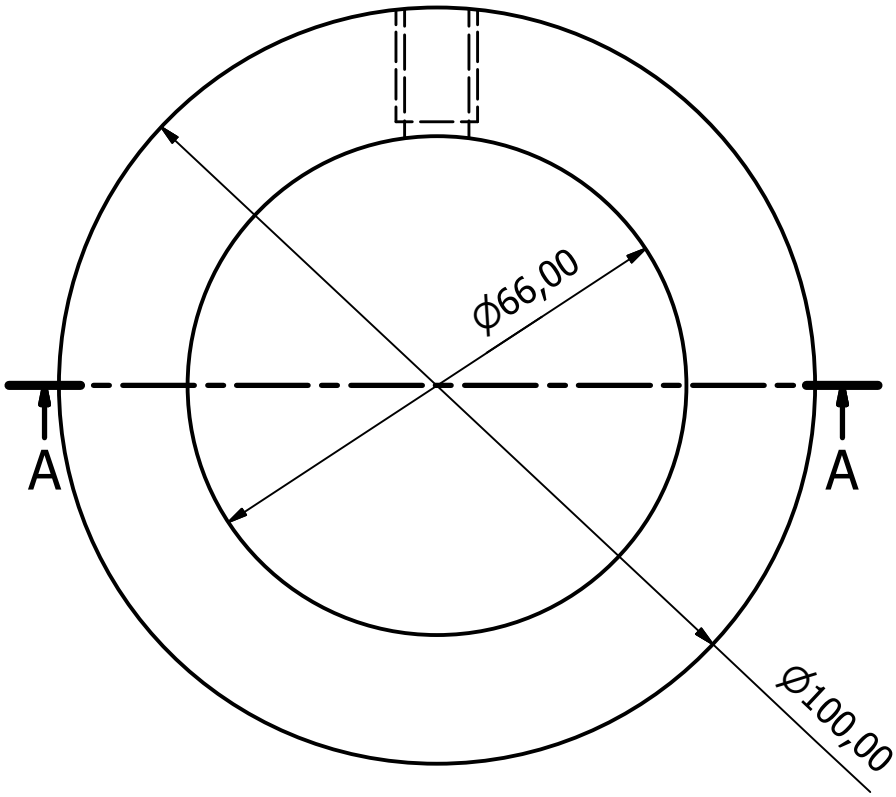

Designed by	Checked by	Approved by	Date		Date	
Jiri Cech					3/8/2013	

DTU Nanotech	Embossinator 2: top		
	Aluminum	Edition	Sheet 1 / 1

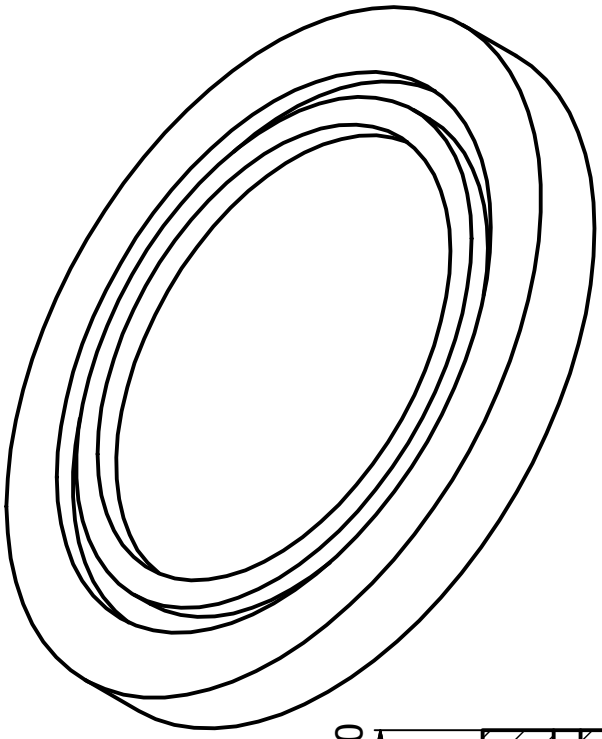

B-B (1 : 1)

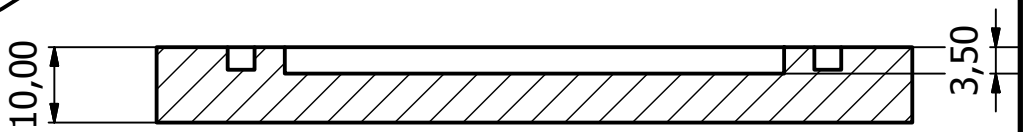

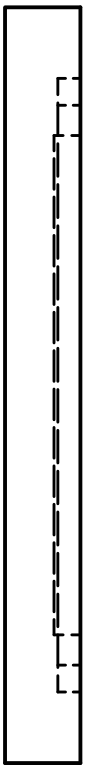

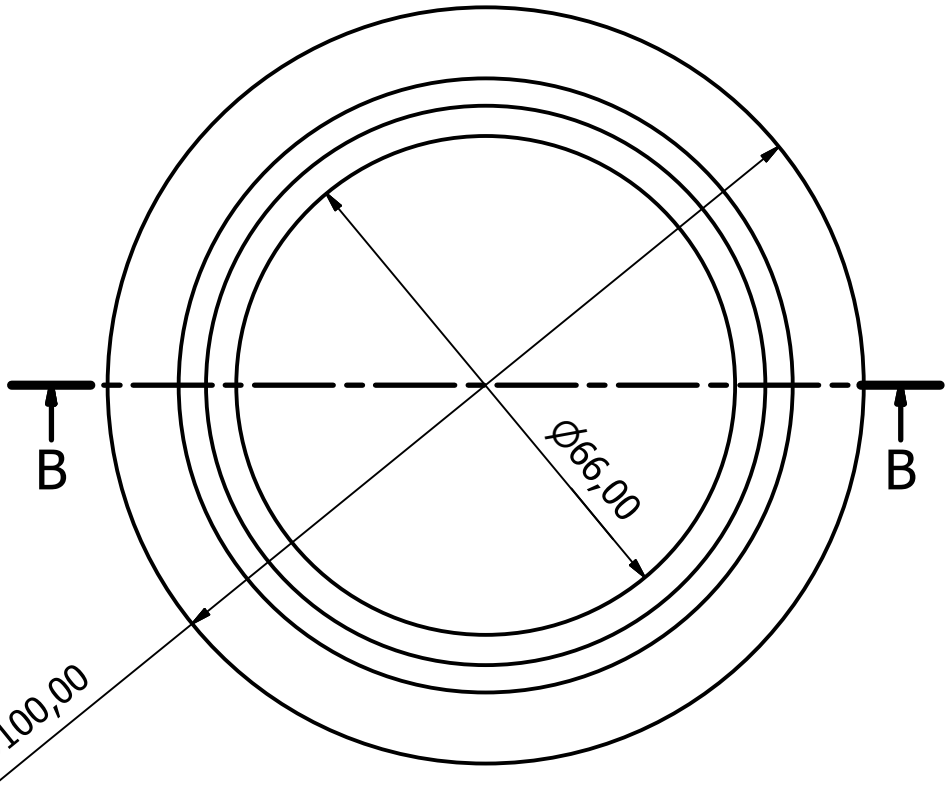

Designed by	Checked by	Approved by	Date		Date	
Jiri Cech					3/8/2013	

DTU Nanotech	Embossinator 2: bottom		
	Aluminum	Edition	Sheet 1 / 1

Appendix C: Publications

In this appendix authors relevant published or submitted publications are reprinted.